

# Exploring Baryon Resonances with Transition Generalized Parton Distributions: Status and Perspectives

S. Diehl<sup>1,2,a,b</sup>, K. Joo<sup>2,a</sup>, K. Semenov-Tian-Shansky<sup>3,a</sup>, C. Weiss<sup>4,a</sup>,  
V. Braun<sup>5</sup>, W.C. Chang<sup>6</sup>, P. Chatagnon<sup>4</sup>, M. Constantinou<sup>7</sup>, Y. Guo<sup>8</sup>,  
P. T. P. Hutaeruk<sup>9</sup>, H.-S. Jo<sup>3</sup>, A. Kim<sup>2</sup>, J.-Y. Kim<sup>4</sup>, P. Kroll<sup>10</sup>,  
S. Kumano<sup>11</sup>, C.-H. Lee<sup>12</sup>, S. Liuti<sup>13</sup>, R. McNulty<sup>14</sup>, H.-D. Son<sup>15</sup>,  
P. Sznajder<sup>16</sup>, A. Usman<sup>17</sup>, C. Van Hulse<sup>18</sup>, M. Vanderhaeghen<sup>19</sup>,  
M. Winn<sup>20</sup>

<sup>1</sup>Justus Liebig Universität Gießen, 35390 Gießen, Germany

<sup>2</sup>University of Connecticut, Storrs, CT 06269, USA

<sup>3</sup>Kyungpook National University, Daegu 41566, Korea

<sup>4</sup>Thomas Jefferson National Accelerator Facility, Newport News, VA 23606, USA

<sup>5</sup>Institut für Theoretische Physik, Universität Regensburg, 93040 Regensburg, Germany

<sup>6</sup>Institute of Physics, Academia Sinica, Taipei 11529, Taiwan

<sup>7</sup>Physics Department, Temple University, Philadelphia, PA 19122-1801, USA

<sup>8</sup>Nuclear Science Division, Lawrence Berkeley National Laboratory, Berkeley, CA 94720, USA

<sup>9</sup>Department of Physics, Pukyong National University (PKNU), Busan 48513, Korea

<sup>10</sup>University of Wuppertal, D-42097 Wuppertal, Germany

<sup>11</sup>Department of Mathematics, Physics, and Computer Science, Faculty of Science, Japan Women's University, Tokyo 112-8681, Japan and Theory Center, Institute of Particle and Nuclear Studies, KEK, Tsukuba, Ibaraki, 305-0801, Japan

<sup>12</sup>Department of Physics, Pusan National University, Busan 46241, Korea and Asia Pacific Center for Theoretical Physics, POSTECH, Pohang 37673, Korea

<sup>13</sup>Physics Department, University of Virginia, Charlottesville, VA 22904-4714, USA

<sup>14</sup>University College Dublin, School of Physics, Science Centre Belfield Dublin 4, Ireland

<sup>15</sup>Department of Physics, Inha University, Incheon 22212, Korea

<sup>16</sup>National Centre for Nuclear Research (NCBJ), 02-093 Warsaw, Poland

<sup>17</sup>University of Regina, Regina SK S4S 0A2 Canada

<sup>18</sup>Universidad de Alcalá, 28801 Alcalá de Henares, Spain

<sup>19</sup>Institut für Kernphysik and PRISMA<sup>+</sup> Cluster of Excellence, Johannes Gutenberg Universität, 55099 Mainz, Germany

<sup>20</sup>DPhN/Irfu, CEA Saclay, 91191 Gif sur Yvette, France

May 27, 2024

**Abstract** QCD gives rise to a rich spectrum of excited baryon states. Understanding their internal structure is important for many areas of nuclear physics, such as nuclear forces, dense matter, and neutrino-nucleus interactions. Generalized parton distributions (GPDs) are an established tool for characterizing the QCD structure of the ground-state nucleon. They are used to create 3D tomographic images of the quark/gluon structure and quantify the mechanical properties such as the distribution of mass, angular momentum and forces in the system. Transition GPDs extend these concepts to  $N \rightarrow N^*$  transitions and can be used to characterize the 3D structure and mechanical properties of baryon resonances. They can be probed in high-momentum-transfer exclusive electroproduction processes with res-

onance transitions  $e+N \rightarrow e'+M+N^*$ , such as deeply-virtual Compton scattering ( $M = \gamma$ ) or meson production ( $M = \pi, K, \text{etc.}$ ), and in related photon/hadron-induced processes.

This White Paper describes a research program aiming to explore baryon resonance structure with transition GPDs. This includes the properties and interpretation of the transition GPDs, theoretical methods for structures and processes, first experimental results from JLab 12 GeV, future measurements with existing and planned facilities (JLab detector and energy upgrades, COMPASS/AMBER, EIC, EicC, J-PARC, LHC ultra-peripheral collisions), and the theoretical and experimental developments needed to realize this program.

<sup>a</sup>Editors

<sup>b</sup>Corresponding author e-mail: stefan.diehl@exp2.physik.uni-giessen.de, sdiehl@jlab.org

## Contents

1	Introduction	2
2	Overview	3
3	Transition GPDs	6
3.1	GPDs of the ground state nucleon	6
3.2	$N \rightarrow \Delta$ transition GPDs	7
3.3	Second resonance region	8
4	Baryon resonance structure	10
4.1	3D tomography of baryon resonances	10
4.2	Spin and angular momentum in baryon resonances	11
4.3	Mechanical properties of baryon resonances	13
4.4	Tensor charge and anomalous magnetic moment	13
5	Theoretical methods for transition GPDs	14
5.1	Chiral dynamics in $N \rightarrow \pi N$ transitions	14
5.2	$1/N_c$ expansion and $N \rightarrow \Delta$ transitions	14
5.3	Light-cone sum rules	15
5.4	Lattice QCD calculations	15
6	Transition processes: electron scattering	15
6.1	$N \rightarrow \Delta$ , $N^*$ DVCS and transition GPDs	16
6.2	$N \rightarrow N^*$ DVMP and transition GPDs	19
6.3	Near-threshold pion production	22
7	First experimental results from JLab 12 GeV	23
7.1	$\pi^- \Delta^{++}$ electroproduction with CLAS12	23
7.2	Further $N \rightarrow N^*$ DVMP channels with CLAS12	24
7.3	$\pi^+ \Delta^0$ electroproduction in JLab Hall C	25
7.4	$N \rightarrow \Delta^+$ DVCS with CLAS12	26
8	Transition processes: hadron scattering	27
8.1	Meson-induced exclusive Drell-Yan process	27
8.2	Proton-induced $2 \rightarrow 3$ processes	30
8.3	Exotic hadron production using GPDs	32
9	Transition processes: diffractive scattering	33
9.1	Inelastic diffraction and quantum fluctuations	33
9.2	GPDs at HERA	33
9.3	Transition GPDs in ultraperipheral collisions	34
10	Future experimental facilities	35
10.1	CLAS12 luminosity upgrade and JLab 22 GeV	35
10.2	Muon and meson beams at COMPASS/AMBER	36
10.3	Electron-Ion Collider EIC	36
10.4	Hadron beams at J-PARC and FAIR	36
10.5	LHC fixed-target and ultraperipheral collisions	37
11	Challenges of GPD analysis	37
12	Future transition GPD program	38
13	Acknowledgements	39

## 1 Introduction

Hadrons are emergent phenomena of Quantum Chromodynamics (QCD), see *e.g.* [1]. The elementary dynamics is expressed in both the spectrum and the structure of the hadronic states. Exploring both expressions together is essential for a complete understanding of strong interactions. There are many examples of connections between the internal motion and the excitation spectrum in nonrelativistic quantum systems (atoms, nuclei). Similar connections are expected in the much more complex relativistic quantum systems presented by the hadrons in QCD.

A rich spectrum of baryon resonances is known to emerge from QCD. They are observed in scattering experiments with electron, photon, and hadron beams at

energies  $\sim$  few GeV. These are excited states of the nucleon (proton or neutron), the basic building block of nuclei and of visible matter in the universe. The spectrum of these excited states was essential for establishing the quark model as a precursor to QCD. The baryon resonances play an important role in the theory of nuclear forces (*e.g.* the  $\Delta$  isobar), in the behavior of matter at high densities and temperatures (early universe, stellar structure), and in the existence of hypothetical strange matter (neutron stars) [2]. They are also needed for describing the interactions of neutrinos with nuclei at energies  $\sim$  few GeV (neutrino detection in oscillation experiments) [3]. Understanding the internal structure of the baryon resonances is thus of fundamental interest and practical importance.

Some information on the structure of baryon resonances is available from the electromagnetic transition form factors measured in electroproduction experiments. They describe the spatial distribution of charge and current in the dynamical system. Further information from other probes is needed to characterize the excited baryon states.

The study of ground-state nucleon structure has made significant advances in the last two decades. The concept of generalized parton distributions (GPDs) [4–6] has provided a rigorous formulation of the spatial distributions of quarks and gluons in the nucleon and offered new opportunities for characterizing nucleon structure, see *e.g.* [7] for an overview. The GPDs unify the concepts of the elastic nucleon form factors and the quark/gluon particle densities. They enable the construction of 3D tomographic images of the distribution of quarks and gluons, which have great potential for the visualization of nucleon structure and the discussion of the internal motion. They also quantify the distribution of energy, momentum, angular momentum, and forces in the nucleon, which allows one to discuss the mechanical properties of the quantum system in analogy with classical systems. The GPDs are extracted using a combination of theoretical methods and experimental data from various scattering processes, particularly exclusive processes at energy and momentum transfers  $\gg 1$  GeV. Programs of GPD measurements are under way at Jefferson Lab (JLab) with 12 GeV electron beam [8, 9], CERN COMPASS [10], Large Hadron Collider (LHC) [11], and Japan Proton Accelerator Research Complex (J-PARC) [12], and planned with the future Electron-Ion Collider (EIC) [13, 14] and Electron-ion collider in China (EicC) [15].

Recent advances have made it possible to extend the framework of GPDs to excited baryon states and use it to characterize baryon resonance structure. Theoretical studies have formulated the concept of  $N \rightarrow$

$\Delta$ ,  $N^*$  transition GPDs and extended the method of quark/gluon tomography to baryon resonances. Experimental efforts have produced the first measurements of exclusive processes with  $N \rightarrow \Delta$  transitions and demonstrated their feasibility. The transition GPDs allow one to ask and answer new questions about baryon resonance structure:

- What is the spatial distribution of quarks in excited baryon states, and how does it differ from the ground state? Can we construct tomographic images of the baryon resonances?
- What are the distributions of energy, momentum, and angular momentum carried by quarks and gluons in baryon resonances? Can we quantify the mechanical properties of the baryon resonances?
- What is the distribution of quark tensor charge in baryon resonances? What is the gluonic structure of resonances? Can we excite baryon resonances using transition operators with quantum numbers other than the vector current operator used in traditional photo/electroexcitation?

These questions greatly expand the scope of baryon resonance structure studies and raise it to the same level as current ground-state nucleon structure studies.

A workshop “Exploring resonance structure with transition GPDs” was held at the European Center for Theoretical Studies in Nuclear Physics and Related Areas (ECT\*) in Trento, Italy, on August 21-25, 2023, supported jointly by ECT\* and the Asia Pacific Center for Theoretical Physics (APCTP) [<https://indico.ectstar.eu/event/176/>]. Twenty-seven presentations were given over five days, followed by extensive discussions. This white-paper summarizes the status of theoretical and experimental studies of transition GPDs and baryon resonance structure, the prospects for future experimental programs using electromagnetic and hadronic probes, and the developments needed for their realization.

The article is organized as follows: Section 2 presents a general introduction to the concepts and an overview of the scientific program. Section 3 provides a theoretical introduction to transition GPDs, while section 4 shows their connection to higher level observables of the baryon resonance structure. In section 5 and overview on the methods for the theoretical treatment of transition GPDs is provided. Section 6 introduces the description of lepto-production processes sensitive to transition GPDs and section 7 presents first experimental results from 12 GeV JLab on deeply virtual  $N \rightarrow N^*$  meson production and  $N \rightarrow N^*$  Compton scattering. Sections 8 and 9 introduce the description and measurement of transition GPDs in hadron scattering and diffractive scattering processes. Section 10 provides an

overview of future perspectives at JLab, but also at hadron facilities like J-PARC and other places. Finally, the strategy for the extraction of transition GPDs from experimental observables is discussed in section 11.

## 2 Overview

Hadron structure in QCD is expressed in the matrix elements of QCD operators between hadronic states. These gauge-invariant operators are composed of the fundamental quark and gluon fields and measure certain features of their distribution in the hadronic state. Two basic types of QCD operators are accessible in scattering experiments. One type are the vector and axial-vector currents of the quark fields, which are probed in elastic lepton-nucleon or neutrino-nucleon scattering mediated by electromagnetic or weak interactions. These operators are local and measure the distribution of electric and axial charge and current in the hadronic state (form factors). Another type are QCD operators arising from the factorization of deep-inelastic scattering processes at energy and momentum transfers much larger than the hadronic scale ( $\gg 1$  GeV). These operators are non-local in space-time (light-like separation of fields) and measure the momentum distributions of quarks and gluons in the hadronic state (parton distributions). Inclusive deep-inelastic lepton-nucleon scattering and related processes have provided extensive information on the quark and gluon parton densities (PDFs).

Exclusive processes in lepton-nucleon scattering at energy and momentum transfers  $W^2, Q^2 \gg 1$  GeV<sup>2</sup> are another class of processes to which the factorization method can be applied. Examples include the electroproduction of real photons (deeply-virtual Compton scattering, or DVCS)  $e + N \rightarrow e' + \gamma + N'$ , electroproduction of light mesons  $e + N \rightarrow e' + M + N'$ , or photo/electroproduction of heavy quarkonia,  $e + N \rightarrow e' + Q + N'$ . In the asymptotic regime, the production process involves individual quarks and gluons, whose coupling to the nucleon is described by QCD operators with light-like separation (see Fig. 1a). The matrix elements of these operators between the nucleon states are parameterized by the GPDs; see Refs. [16–18] for a review. These are non-forward matrix elements, involving a longitudinal and transverse momentum transfer of the order of the hadronic scale between the initial and final nucleon, resulting in a rich structure. GPDs thus unify the concepts of elastic form factors and parton densities, and contain both as limiting cases.

GPDs provide new information on nucleon structure beyond what is available from conventional probes (form factors, PDFs) (see Fig. 2). (i) The transverse

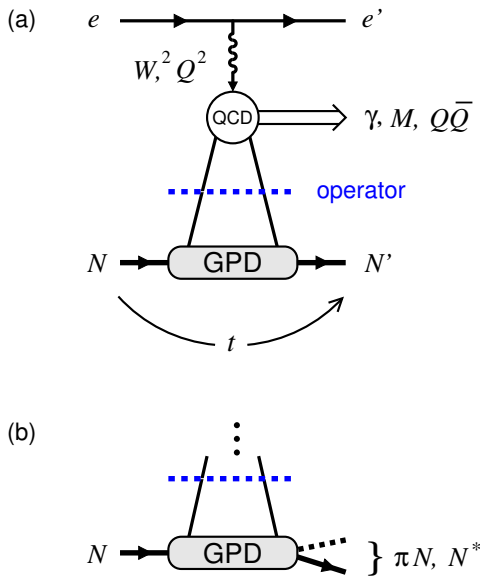


**Fig. 1** (a) QCD factorization of hard exclusive processes  $e + N \rightarrow e' + \{\gamma N, MN, Q + N'\}$ . The production process couples to the nucleon through a QCD operator. The  $N \rightarrow N$  matrix element of the operator is described by the GPD. (b) Processes with transition  $N \rightarrow \pi N, \Delta, N^*$ . The  $N \rightarrow \pi N, \Delta, N^*$  matrix element of the operator is described by the transition GPD.

Fourier transform of the GPDs (transverse momentum transfer  $\Delta_T \rightarrow$  transverse coordinate  $b$ ) describes the transverse spatial distribution of quarks and gluons with given longitudinal momentum fraction  $x$  [19, 20]. It provides a 2 + 1 dimensional “tomographic image” of the nucleon. This spatial representation is appropriate for the nucleon as a relativistic quantum system and allows one to visualize it as an extended object in space-time. The spatial structure can be connected with the internal motion of the quarks and gluons and their polarization and provides a new framework for the discussion of structure and dynamics. “3D imaging” of the nucleon based on GPDs, which requires measurements with high precision, is the object of experimental programs at JLab and EIC. (ii) The moments of the GPDs (weighted integrals over the momentum fraction  $x$ ) represent matrix elements of local QCD operators of spin  $n > 1$  (so-called generalized form factors). This makes it possible to probe nucleon structure with local operators beyond the spin-1 operators accessible with the electroweak currents. The spin-2 operators obtained from GPDs contain the QCD energy-momentum tensor, the matrix elements of which describe the distribution of momentum, angular momentum, forces, and mass and are of fundamental interest for nucleon structure. Characterizing the “mechanical properties” of hadrons based on the QCD energy-momentum tensor has emerged as a field of study in its own right, with many theoretical

and experimental results; see Refs. [21, 22] for a review.

QCD factorization can be applied not only to exclusive processes with  $N \rightarrow N$  transitions on the target side, but also to processes in which the nucleon undergoes a transition to a low-mass hadronic state,  $N \rightarrow \pi N, \pi\pi N, N^*, \dots$  (see Fig. 1b) [16]. Examples are DVCS with  $N \rightarrow \pi N$  transitions,  $e + N \rightarrow e' + \gamma + \pi N(\text{low-mass})$ ; or exclusive pion production with  $N \rightarrow \pi N$  transitions,  $e + N \rightarrow e' + \pi + \pi N(\text{low-mass})$ . The QCD operators representing the high-energy processes are the same as in the case of  $N \rightarrow N$  transitions. The matrix elements are now taken between the initial  $N$  and the final  $\pi N$  state,  $\langle \pi N | \mathcal{O}_{\text{QCD}} | N \rangle$ , and are parameterized by so-called transition GPDs. This extends the concepts of GPDs to transitions between low-mass hadronic states. The final  $\pi N$  state here can be non-resonant or resonant. Matrix elements for transitions to a baryon resonance  $N \rightarrow N^*$  can be defined rigorously through analytic continuation in invariant mass of the  $\pi N$  system (resonance pole). This allows one to establish the concept of GPDs for baryon resonance transitions.

The nucleon is known to possess a rich spectrum of excited states [23]. They are observed in production and decay processes induced by electromagnetic and hadronic probes. The spectrum has been explained using models based on effective degrees of freedom (quark model, chiral soliton) and is increasingly being confirmed by lattice QCD (LQCD) calculations. Exploring the structure of the excited states in terms of QCD degrees of freedom is the next step in their study. In the hadronic picture the excited states are as fundamental as the ground state, and the QCD structure of all the states is needed for a complete understanding of strong interaction dynamics. Some information on  $N^*$  structure is available from the transition form factors of the vector current measured in electroexcitation processes. Much more information on  $N^*$  can be obtained from the transition GPDs measured in  $N \rightarrow N^*$  exclusive processes and the concepts derived from them (see Fig. 2). The transition GPDs allow one to construct tomographic images of the  $N^*$  at the same level as the  $N$  and discuss the QCD structure of resonances in these terms. They provide access to the transition matrix elements of the QCD EMT and allow one to discuss the mechanical properties of the resonances. The factorization of exclusive processes provides QCD operators with quantum numbers that are not easily accessible otherwise, such as chiral-odd quark operators (pion production) and gluonic operators (heavy-quarkonium production), and these operators can be used for resonance excitation and structure studies. While extracting the

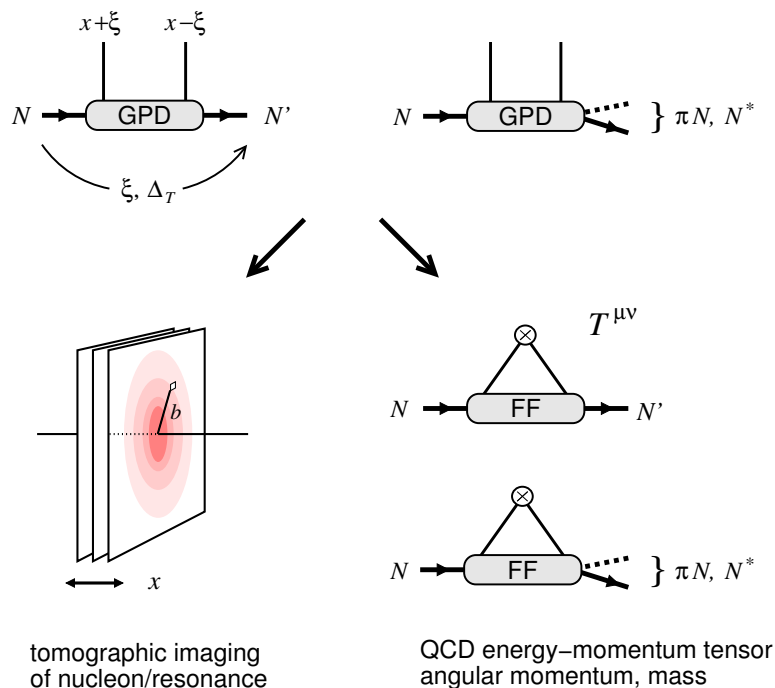


**Fig. 2** Applications of GPDs to nucleon structure: (a) Transverse spatial distributions of partons (tomographic imaging). (b) Form factors of QCD energy-momentum tensor describing distributions of angular momentum, mass, and forces (mechanical properties). The concepts and structures can be extended to  $N \rightarrow \pi N, N^*$  transitions.

structures from experiments poses considerable challenges, the concepts derived from transition GPDs can also be explored using dynamical models and LQCD results and enrich  $N^*$  structure studies in this way. Altogether, transition GPDs have the potential to greatly expand the range of baryon structure studies in QCD.

After first studies of associated electroproduction of real photons,  $e + p \rightarrow e' \gamma \pi N$ , in the  $\Delta(1232)$ -resonance region with HERMES [24], recent experiments at JLab have shown the feasibility of measuring exclusive processes with  $N \rightarrow N^*$  transitions with significantly increased precision and background separation capabilities. Measurements of exclusive electroproduction  $e + p \rightarrow e' + \pi^- + \Delta^{++}$  have been performed at JLab CLAS12 and are being interpreted in terms of transition GPDs [25]. Similar measurements of  $e + p \rightarrow e' + \pi^+ + \Delta^0$  have been performed at JLab Hall C and are being analyzed. Measurements of DVCS with  $N \rightarrow \Delta$  and other  $N \rightarrow N^*$  transitions will be possible with the forthcoming CLAS12 data.

A program for exploring resonance structure using transition GPDs is emerging. To realize it, it is necessary to develop theoretical and experimental methods, define the scientific objectives, simulate the proposed measurements, and optimize the analysis and extraction procedure.

Theoretical methods needed for the transition GPD program include the structural decomposition of the

$N \rightarrow N^*$  matrix elements of the QCD operators and their parametrization in terms of transition GPDs. The structure of the  $N \rightarrow \Delta$  matrix elements of the chiral-even QCD operators was discussed in Refs. [16, 18]. Recent work revisited the definition of the chiral-even  $N \rightarrow \Delta$  transition GPDs and extended the analysis to the chiral-odd sector [26]. The  $N \rightarrow \Delta$  transition matrix elements of the QCD energy-momentum tensor were studied in Ref. [27–29].

Also needed is the physical interpretation of the transition matrix elements, especially the  $N \rightarrow N^*$  transition matrix elements of the QCD energy-momentum tensor and the mechanical properties derived from it. Recent work has extended the concept of QCD angular momentum to  $N \rightarrow \Delta$  transitions, using a formulation in terms of light-front densities appropriate for transitions between baryon states with different masses and quantum numbers [30].

Theoretical efforts also focus on making quantitative predictions of the transition GPDs using methods of nonperturbative QCD. Particularly useful are methods that can connect the  $N \rightarrow N$  and  $N \rightarrow \pi N, \Delta$  etc. matrix elements in a systematic fashion. The  $1/N_c$  expansion of QCD is a general method for analyzing matrix elements of QCD operators in meson and baryon states. It is based on the dynamical spin-flavor symmetry of QCD in the large- $N_c$  limit, where  $N$  and  $\Delta$  states are in the same multiplet, and transitions between them

are connected by symmetry. The method can classify and predict the spin-flavor components of  $N \rightarrow \Delta$  transition GPDs and express them in terms of the  $N \rightarrow N$  GPDs. The  $1/N_c$  expansion was applied to chiral-even transition GPDs [16], and was recently extended to study chiral-odd GPDs [26, 31]. Methods based on chiral dynamics (soft-pion theorems, chiral perturbation theory) can connect  $N \rightarrow N$  and  $N \rightarrow \pi N$  transition matrix elements near threshold and predict transition GPDs in this regime [32–35]. They can also be extended to processes with  $N \rightarrow \Delta$  transitions [36, 37]. Models based on the holographic representation of QCD (gauge-string duality) posit a close connection between hadron structure and the spectrum of excited states and are useful for the study of GPDs and transition GPDs [38].

LQCD methods for computing nucleon matrix elements of local QCD operators are well developed. They have recently been extended to enable the computation of  $x$ -dependent partonic structure, using matrix elements of nonlocal operators with spacelike separation in fast-moving hadronic states (quasi/pseudo distributions). Applications to GPDs are in progress [39–41]. At the same time, LQCD methods have been adapted to extract excited hadronic states, using arrays of Euclidean correlation functions of operators projecting on ground and excited states (generalized eigenvalue problem, distillation) [42, 43]. While the combination of both techniques is challenging and requires major development, there is the long-term prospect of LQCD calculations of transition GPDs.

Theory developments currently focus on reaction theory and observables for DVCS with  $N \rightarrow \Delta$  and  $N \rightarrow N^*$  transitions [44] as well as  $\pi$  electroproduction with  $N \rightarrow \Delta$  transitions [26].

Experimental developments at JLab focus on improving the measurement of pion production with  $N \rightarrow \Delta$  transitions (CLAS12, Hall C), and preparing measurements of DVCS with  $N \rightarrow \Delta$  and other  $N \rightarrow N^*$  transitions (CLAS12). It is planned to extend the studies to the strangeness sector. The luminosity upgrade of CLAS12, which is currently in preparation, will help to increase the statistics for these studies. Further detector modifications to increase the detection efficiency of the processes with CLAS12 will be investigated. A potential energy upgrade of JLab [45] would help to increase the accessible  $Q^2$  range (factorization of the processes) and the phase space of the invariant masses above the background rejection cuts (detection efficiency).

The future EIC will enable an extended program of GPD measurements on the proton at high energies ( $10^{-3} \lesssim x_B \lesssim 0.1$ ). The final-state proton or neutron moves forward in the ion beam direction and will be

detected with the far-forward detection system (magnetic spectrometer with several detector subsystems for proton, zero-degree calorimeter for neutron) [13]. The possibility of  $\pi N$  and other transition GPD measurements with this setup is being explored and presents interesting challenges for the far-forward detection and event reconstruction.

Ultrapерipheral proton-nucleus collisions and central exclusive production in proton-proton collisions at LHC enable measurements of photon-proton scattering at energies  $W \sim 10^3$  GeV, the highest energies available for electromagnetic scattering (an order of magnitude larger than at the electron-proton HERA collider) [46]. The setup is used to measure gluon GPDs in the photoproduction of heavy quarkonia,  $\gamma + p \rightarrow \bar{Q}Q + p$ , reaching momentum fractions  $x \sim 10^{-6}$  [47, 48]. This exclusive scattering process is diffractive (vacuum exchange) and can be discussed using concepts of diffractive scattering. The scattering either leaves the proton intact,  $p \rightarrow p$ , or causes it to dissociate into a low-mass hadronic state,  $p \rightarrow X(\text{low-mass})$ . The latter process measures the gluon GPD for  $p \rightarrow X$  transitions, which can be connected with the quantum fluctuations of the gluon density in the proton [49].

Hadron-induced scattering processes can also be used to access GPDs under certain conditions, providing a complementary method to electromagnetic processes. Exclusive dilepton production (Drell-Yan pair production) [50, 51] as well as  $2 \rightarrow 3$  processes [52], have been proposed as a way of measuring GPDs and transition GPDs. These hadron-induced processes have a natural connection to transition GPDs.

### 3 Transition GPDs

#### 3.1 GPDs of the ground state nucleon

GPDs encode the 3-dimensional partonic structure of the nucleon by correlating the internal transverse position of the partons with their longitudinal momentum fraction [4, 53, 54]. For a nucleon with arbitrary spin, there are in total 8 independent GPDs of which 4 do not flip the parton helicity, while the other 4 flip the parton helicity and are also known as transversity GPDs (indicated by  $T$  in the subscript) [17, 55, 56]. These GPDs can be related to the polarization of the nucleon ( $N$ ) and the parton ( $q$ ), which can both be unpolarized (U), longitudinally polarized (L) or transversely polarized (T) and are summarized in Tab. 1.

GPDs typically depend on the kinematic variables  $x$ ,  $\xi$ , and  $t$ . The introduced variable  $x$  can be physically interpreted in a way, that during the scattering process, a quark is removed from the nucleon with a momentum

$N \setminus q$	<b>U</b>	<b>L</b>	<b>T</b>
<b>U</b>	$H$		$\bar{E}_T$
<b>L</b>		$\tilde{H}$	$\tilde{E}_T$
<b>T</b>	$E$	$\tilde{E}$	$H_T, \tilde{H}_T$

**Table 1** GPDs for the ground state nucleon. With  $\bar{E}_T = 2\tilde{H}_T + E_T$ .

fraction  $x + \xi$  and reinserted with a reduced momentum fraction  $x - \xi$  at a certain transverse distance, parameterized by the conjugate of the Mandelstam variable  $t$  [57].

### 3.2 $N \rightarrow \Delta$ transition GPDs

Transition GPDs describe transitions from a ground-state nucleon to a resonating meson-nucleon system and occur in a description of several classes of hard-exclusive reactions within the collinear factorization framework. First studies are focused on the nucleon transitions to  $\Delta$  and nucleon resonances with the lowest masses. A possible more general description in terms of  $N \rightarrow \pi N$  transition GPDs [58, 59] was sketched in [16]. In the threshold region, the  $N \rightarrow \pi N$  GPDs are related to the nucleon GPDs through the soft-pion theorems, allowing the parameter-free predictions for the  $N \rightarrow \pi N$  DVCS at the pion production threshold [34].

For the special case of the  $N \rightarrow \Delta$  transition, a total of 16 (twist-2) transition GPDs [18, 26] can be defined. Several equivalent definitions are available in the literature. Here, for the cases of vector and axial-vector operators, we present the definitions of the set of GPDs of Ref. [18] for the proton-to- $\Delta^{++}$  transition employed in the recent analysis [26]. There are four even-parity transition GPDs,

$$\begin{aligned}
& \int \frac{d\tau}{2\pi} e^{i\tau(n \cdot P)x} \\
& \langle \Delta^{++}(p_R, \lambda_R) | \bar{u}(-\tau n/2) \gamma^+ d(\tau n/2) | N^p(p, \lambda_N) \rangle \\
& = \frac{1}{(n \cdot P)} \bar{U}_\delta(p_R, \lambda_R) \left\{ \frac{\Delta^\delta n^\mu - \Delta^\mu n^\delta}{M_N} (\gamma_\mu G_1(x, \xi, t)) \right. \\
& + \frac{P_\mu}{M_N} G_2(x, \xi, t) + \frac{\Delta_\mu}{M_N} G_3(x, \xi, t) \\
& \left. + \frac{\Delta^+ \Delta^\delta}{M_N^2} G_4(x, \xi, t) \right\} \gamma_5 u(p, \lambda_N); \quad (1)
\end{aligned}$$

and four odd-parity ones,

$$\begin{aligned}
& \int \frac{d\tau}{2\pi} e^{i\tau(n \cdot P)x} \\
& \langle \Delta^{++}(p_R, \lambda_R) | \bar{u}(-\tau n/2) \gamma^+ \gamma^5 d(\tau n/2) | N^p(p, \lambda_N) \rangle \\
& = \frac{1}{(n \cdot P)} \bar{U}_\delta(p_R, \lambda_R) \left\{ \frac{\Delta^\delta n^\mu - \Delta^\mu n^\delta}{M_N} (\gamma_\mu \tilde{G}_1(x, \xi, t)) \right. \\
& + \frac{P_\mu}{M_N} \tilde{G}_2(x, \xi, t) + n^\delta \tilde{G}_3(x, \xi, t) \\
& \left. + \frac{\Delta^+ \Delta^\delta}{M_N^2} \tilde{G}_4(x, \xi, t) \right\} u(p, \lambda_N). \quad (2)
\end{aligned}$$

Here,  $n^2 = 0$  is the light-cone vector; and for simplicity, the light-cone gauge  $A^+ \equiv A \cdot n = 0$  is adopted;  $P$  is the average hadron momentum  $P \equiv \frac{p^+ + p_R^+}{2}$  and  $\Delta \equiv p_R - p$  is the momentum transfer;  $p(\lambda_N, M_N)$  and  $p_R(\lambda_R, M_\Delta)$  denote the proton and the  $\Delta(1232)$  momenta (helicities and masses), respectively. The quantity  $U_\delta(p_R, \lambda_R)$  stands for the Rarita-Schwinger spinor describing the  $\Delta$  particle, and  $u(p, \lambda_N)$  is the nucleon's Dirac spinor. The skewness parameter  $\xi$  is defined by the ratio of light-cone plus components of  $\Delta$  and  $P$ :

$$\xi = -\frac{\Delta^+}{2P^+}. \quad (3)$$

The Mandelstam variable  $t$  is given by

$$t = \Delta^2 = t_0 - \frac{\Delta_\perp^2}{1 - \xi^2}, \quad (4)$$

where  $t_0$  is the minimal value of  $-t$  implied by the positivity of the transverse squared momentum transfer  $\Delta_\perp^2$

$$t_0 = -\frac{2\xi}{1 - \xi^2} \left[ (1 + \xi)(M_\Delta^2 - M_N^2) + 2\xi M_N^2 \right]. \quad (5)$$

So far the  $\Delta(1232)$  is considered to be a stable particle. Therefore, one can apply the usual time-reversal invariance arguments to show that the  $p - \Delta$  GPDs turn to be real-valued functions of the momentum fraction  $x$ , the skewness and  $t$  [18]. The GPDs also depend on the factorization scale. For convenience, this dependence is suppressed here.

An alternative parametrization [60] relying on a different set of spin-tensor structures involves 4 unpolarized GPDs  $h_{M, E, C, 4}(x, \xi, t)$  and 4 polarized GPDs  $C_{1, 2, 3, 4}(x, \xi, t)$ ; and is employed in the analysis of Ref. [44]. The relation of this transition GPD set to that of the heritage parametrization of Ref. [16] is specified in Ref. [60].

The set of 8 transversity GPDs  $G_{T1, \dots, T8}(x, \xi, t)$  has been defined in [26]:

$$\begin{aligned}
& \int \frac{d\tau}{2\pi} e^{i\tau(n \cdot P)x} \\
& \langle \Delta^{++}(p_R, \lambda_R) | \bar{u}(-\tau n/2) i\sigma^{+j} d(\tau n/2) | N^p(p, \lambda_N) \rangle \\
& = \frac{1}{(n \cdot P)} \bar{U}_\delta(p_R, \lambda_R) \left\{ G_{T1} \frac{p^\delta}{M_N} i\sigma^{+j} \right. \\
& + G_{T2} p^\delta \frac{P^+ \Delta^j - \Delta^+ P^j}{M_N^3} + G_{T3} p^\delta \frac{\gamma^+ \Delta^j - \Delta^+ \gamma^j}{2M_N^2} \\
& + G_{T4} p^\delta \frac{\gamma^+ P^j - P^+ \gamma^j}{M_N^2} + G_{T5} (n^\delta \gamma^j - \gamma^\delta n^j) \\
& + G_{T6} \frac{n^\delta \Delta^j - \Delta^\delta n^j}{M_N} \left. \right\} \gamma_5 u(p, \lambda_N) \\
& + \frac{1}{(n \cdot P)} \left\{ G_{T7} (\bar{U}^+(p_R, \lambda_R) \gamma^j - \bar{U}^j(p_R, \lambda_R) \gamma^+) \right. \\
& + G_{T8} \frac{\bar{U}^+(p_R, \lambda_R) \Delta^j - \bar{U}^j(p_R, \lambda_R) \Delta^+}{M_N} \left. \right\} \gamma_5 u(p, \lambda_N). \quad (6)
\end{aligned}$$

Isospin symmetry relates the  $p \rightarrow \Delta^{++}$  GPDs to those of other  $\Delta(1232)$  states [18]:

$$G_{p\Delta^{++}}^{ud} = -\frac{\sqrt{3}}{2} G_{p\Delta^+}^{uu-dd} = -\sqrt{3} G_{p\Delta^0}^{du}, \quad (7)$$

where the flavor content of the GPDs is indicated.

The definitions (1), (2) and (6) also hold for any other octet-decuplet transition GPDs. Moreover, the flavor symmetry relates the various octet-decuplet GPDs to each other [18].

The 8 GPDs defined in Eqs. (1), (2) are helicity-nonflip transition GPDs. Four of them ( $G_1 - G_4$ ) are unpolarized (parity even) and can be related to the Jones-Scadron electromagnetic form factors for the  $N \rightarrow \Delta$  transition [16, 61]:

$$\begin{aligned}
& \int_{-1}^1 dx G_1(x; \xi; t) \propto G_M^*(t), & \int_{-1}^1 dx G_2(x; \xi; t) \propto G_E^*(t), \\
& \int_{-1}^1 dx G_3(x; \xi; t) \propto G_C^*(t), & \int_{-1}^1 dx G_4(x; \xi; t) = 0,
\end{aligned} \quad (8)$$

with the magnetic dipole, electric quadrupole, and the Coulomb quadrupole form factors  $G_{M,E,C}^*(t)$ . The other four ( $\tilde{G}_1 - \tilde{G}_4$ ) are polarized (parity odd) and can be related to the Adler form factors of the  $N \rightarrow \Delta$  transition ( $C^A(t)$ ) [16, 62, 63]:

$$\begin{aligned}
& \int_{-1}^1 dx \tilde{G}_1(x; \xi; t) \propto C_5^A(t), & \int_{-1}^1 dx \tilde{G}_2(x; \xi; t) \propto C_6^A(t), \\
& \int_{-1}^1 dx \tilde{G}_3(x; \xi; t) \propto C_3^A(t), & \int_{-1}^1 dx \tilde{G}_4(x; \xi; t) \propto C_4^A(t).
\end{aligned} \quad (9)$$

### 3.3 Second resonance region

The extension of the transition GPD formalism to the second  $\pi N$  resonance region requires introducing parametrizations for the twist-2  $N \rightarrow N^*$  transition GPDs for the case of the vector bilinear and axial-vector quark operators on the light cone for the isospin- $\frac{1}{2}$  resonances  $P_{11}(1440)$ ,  $D_{13}(1520)$  and  $S_{11}(1535)$  with and the spin-parity quantum numbers, respectively,  $J^P = \frac{1}{2}^+, \frac{3}{2}^-, \frac{1}{2}^-$ .

The parametrizations of  $N \rightarrow P_{11}(1440)$ ,  $D_{13}(1520)$ ,  $S_{11}(1535)$  transition GPDs introduced in Ref. [44] for the case of the vector bilinear quark operator were designed with the sets of spin-tensor structures consistent with the parametrizations of corresponding transition electromagnetic form factors detailed in Ref. [64]. Similarly, for the axial-vector bilinear quark operator, the parametrization of Ref. [44] tends to ensure the simple connection with the FFs occurring in the parametrizations of the transition matrix elements of the isoscalar  $A_0^\nu(0)$  and isovector  $A_3^\nu(0)$  axial currents:

$$A_{\{0,3\}}^\nu(0) \equiv \frac{1}{2} [\bar{u}(0) \gamma^\nu \gamma_5 u(0) \pm \bar{d}(0) \gamma^\nu \gamma_5 d(0)]. \quad (10)$$

This provides a simple form of the normalization constraint for the first Mellin moments from determining the dominant  $N \rightarrow N^*$  axial FFs with help of the PCAC relation

$$\partial_\nu A_3^\nu = -f_\pi m_\pi^2 \Pi_3, \quad (11)$$

where the pion decay constant  $f_\pi \simeq 92.4$  MeV; and  $\Pi_3$  stands for the  $\pi^0$  field operator.

As an example, we present the case of GPDs for the  $N \rightarrow P_{11}$  transition. Due to the identical spin-parity, the parametrization has a form similar to the nucleon GPD case, with two unpolarized and two polarized twist-2 GPDs. The matrix element of the vector bilinear quark operator along the light-cone can be parameterized as:

$$\begin{aligned}
& \int \frac{d\tau}{2\pi} e^{i\tau(n \cdot P)x} \\
& \sum_q e_q^2 \langle R(p_R, \lambda_R) | \bar{q}(-\tau n/2) \gamma^+ q(\tau n/2) | N(p, \lambda_N) \rangle \\
& = \frac{1}{(n \cdot P)} \bar{R}(p_R, \lambda_R) \left\{ H_1^{pP_{11}}(x, \xi, \Delta^2) \right. \\
& \times \left( n^\nu - \frac{n \cdot \Delta}{\Delta^2} \Delta^\nu \right) \gamma_\nu \\
& \left. + H_2^{pP_{11}}(x, \xi, \Delta^2) \frac{i\sigma_{\nu\kappa} n^\nu \Delta^\kappa}{(M_R + M_N)} \right\} u(p, \lambda_N), \quad (12)
\end{aligned}$$

where the convective DVCS combination is weighted by the quadratic quark charges  $e_q$ ; and  $\bar{R}(p_R, \lambda_R)$  denotes the Dirac spinor of the final state  $P_{11}$ . This definition results in the following normalization of the first



Mellin moment of GPDs to the proton ( $N = p$ ) and neutron ( $N = n$ ) to  $P_{11}$  transition electromagnetic FFs:

$$\int_{-1}^1 dx H_{1,2}^{pP_{11}}(x, \xi, \Delta^2) = F_{1,2}^{pP_{11}}(\Delta^2) + \frac{2}{3} F_{1,2}^{nP_{11}}(\Delta^2). \quad (13)$$

The transition electromagnetic FFs  $F_1^{NP_{11}}$  and  $F_2^{NP_{11}}$  are defined from the matrix element

$$\begin{aligned} & \langle R(p_R, \lambda_R) | J_{\text{em}}^\nu(0) | N(p, \lambda_N) \rangle \\ & = \bar{R}(p_R, \lambda_R) \Gamma_{\gamma NP_{11}}^\nu(p_R, p) u(p, \lambda_N), \end{aligned} \quad (14)$$

where the vertex  $\Gamma_{\gamma NP_{11}}^\nu$  is parameterized as [65]:

$$\begin{aligned} \Gamma_{\gamma NP_{11}}^\nu(p_R, p) & = F_1^{NP_{11}}(\Delta^2) \left[ \gamma^\nu - \frac{(\gamma \cdot \Delta) \Delta^\nu}{\Delta^2} \right] \\ & + F_2^{NP_{11}}(\Delta^2) \frac{i \sigma^{\nu\kappa} \Delta_\kappa}{(M_R + M_N)}. \end{aligned} \quad (15)$$

For the phenomenological applications, we rely on the empirical MAID2008 analysis for the proton and the MAID2007 analysis for the neutron, as detailed in Ref. [64].

Furthermore, in the case of the axial-vector operator, the parametrization for the  $N \rightarrow P_{11}$  transition reads

$$\begin{aligned} & \int \frac{d\tau}{2\pi} e^{i\tau(n \cdot P)x} \\ & \sum_q e_q^2 \langle R(p_R, \lambda_R) | \bar{q}(-\tau n/2) \gamma^+ \gamma_5 q(\tau n/2) | N(p, \lambda_N) \rangle \\ & = \frac{1}{(n \cdot P)} \bar{R}(p_R, \lambda_R) \left\{ \tilde{H}_1^{pP_{11}}(x, \xi, \Delta^2) \gamma \cdot n \gamma_5 \right. \\ & \left. + \tilde{H}_2^{pP_{11}}(x, \xi, \Delta^2) \frac{\Delta \cdot n}{(M_R + M_N)} \gamma_5 \right\} u(p, \lambda_N). \end{aligned} \quad (16)$$

To work out the normalization, we need to consider the transition matrix elements of the isovector and isoscalar axial currents (10). For the isovector axial current  $N \rightarrow P_{11}$  transition it reads

$$\begin{aligned} & \langle R(p_R, \lambda_R) | A_3^\nu(0) | N(p, \lambda_N) \rangle \\ & = \bar{R}(p_R, \lambda_R) \left\{ G_A^{NP_{11}}(\Delta^2) \gamma^\nu \gamma_5 \right. \\ & \left. + G_P^{NP_{11}}(\Delta^2) \frac{\Delta^\nu \gamma_5}{(M_R + M_N)} \right\} \frac{\tau_3}{2} u(p, \lambda_N), \end{aligned} \quad (17)$$

with  $\tau_3$  the third isospin Pauli matrix., Here,  $G_A^{NP_{11}}$  and  $G_P^{NP_{11}}$  are the corresponding isovector axial transition FFs. And, similarly, for the isoscalar axial current  $N \rightarrow P_{11}$  transition:

$$\begin{aligned} & \langle R(p_R, \lambda_R) | A_0^\nu(0) | N(p, \lambda_N) \rangle \\ & = \bar{R}(p_R, \lambda_R) \left\{ G_{A,0}^{NP_{11}}(\Delta^2) \gamma^\nu \gamma_5 \right. \\ & \left. + G_{P,0}^{NP_{11}}(\Delta^2) \frac{\Delta^\nu \gamma_5}{(M_R + M_N)} \right\} \frac{1}{2} u(p, \lambda_N), \end{aligned} \quad (18)$$

with  $G_{A,0}^{NP_{11}}$  and  $G_{P,0}^{NP_{11}}$  the corresponding isoscalar axial transition FFs.

The relations between the first moments of the polarized GPDs (16) for a given quark flavor entering the definition in Eq. (16) and the axial transitions FFs defined in Eqs. (17) and (18) are then obtained as:

$$\begin{aligned} \int_{-1}^1 dx \tilde{H}_1^{u,pP_{11}}(x, \xi, \Delta^2) & = \frac{1}{2} (G_A^{NP_{11}} + G_{A,0}^{NP_{11}})(\Delta^2), \\ \int_{-1}^1 dx \tilde{H}_1^{d,pP_{11}}(x, \xi, \Delta^2) & = \frac{1}{2} (-G_A^{NP_{11}} + G_{A,0}^{NP_{11}})(\Delta^2), \end{aligned} \quad (19)$$

and analogous relations for  $\tilde{H}_2^{u,pP_{11}}$  and  $\tilde{H}_2^{d,pP_{11}}$  in terms of  $G_P^{NP_{11}}$  and  $G_{P,0}^{NP_{11}}$ .

The physical normalization for the  $N \rightarrow P_{11}$  transition isovector axial FF can be obtained by use of the PCAC relation (11) together with an effective  $\pi NP_{11}$  vertex derived from the effective Lagrangian

$$\mathcal{L}_{\pi NP_{11}} = \left( \frac{f_{\pi NP_{11}}}{m_\pi} \right) \bar{R} \gamma^\mu \gamma_5 \tau_i N (\partial_\mu \Pi_i) + \text{h.c.}, \quad (20)$$

with  $\pi NP_{11}$  coupling constant  $f_{\pi NP_{11}}$ . This results in the generalized Goldberger-Treiman relation for the  $N \rightarrow P_{11}$  isovector axial FF:

$$G_A^{NP_{11}}(0) = \left( \frac{f_{\pi NP_{11}}}{m_\pi} \right) 2f_\pi. \quad (21)$$

Furthermore, using the pion-pole dominance for the axial FF  $G_P^{NP_{11}}$  at small values of  $\Delta^2$  yields:

$$G_P^{NP_{11}}(\Delta^2) \approx \frac{(M_R + M_N)^2}{-\Delta^2 + m_\pi^2} G_A^{NP_{11}}(\Delta^2). \quad (22)$$

The isoscalar  $N \rightarrow P_{11}$  axial FFs  $G_{A,0}^{NP_{11}}$  and  $G_{P,0}^{NP_{11}}$  are not known. As a possible best guess one may use for  $G_{A,0}^{NP_{11}}$  the same quark model relation as for the nucleon isoscalar axial FF:

$$G_{A,0}^{NP_{11}}(\Delta^2) \approx \frac{3}{5} G_A^{NP_{11}}(\Delta^2), \quad (23)$$

and parameterize  $G_A^{NP_{11}}$  by a dipole form as in the nucleon case:

$$G_A^{NP_{11}}(\Delta^2) = 1/(1 - \Delta^2/M_A^2)^2, \quad (24)$$

with dipole mass  $M_A \simeq 1.0$  GeV. Furthermore, the isoscalar FF is set to zero

$$G_{P,0}^{NP_{11}} \approx 0, \quad (25)$$

in line with pion-pole dominance. A possible cross check for such estimates can be provided by calculating these FFs within dynamical quark-diquark approaches, which have proven to provide a good understanding of the data for the vector FFs  $F_{1,2}^{NP_{11}}$  for the  $N \rightarrow P_{11}$  transition [66].

The cases of  $N \rightarrow D_{13}(1520)$  and  $N \rightarrow S_{11}(1535)$  in [44] are treated in a similar manner. The parametrization of leading twist vector and axial-vector GPDs for  $N \rightarrow D_{13}(1520)$  involves 4 + 4 invariant GPDs, while  $N \rightarrow S_{11}(1535)$  involves 2 + 2 invariant GPDs. The phenomenological normalization for the first Mellin moment vector transition GPDs is provided by the relation to the transition electromagnetic FFs available *e.g.* from the empirical MAID2008 analysis for the proton and the MAID2007 analysis for the neutron detailed in Ref. [64]. The normalization of the axial vector can be established relying on the PCAC, following a line similar to the case of  $N \rightarrow P_{11}(1440)$  described above.

## 4 Baryon resonance structure

### 4.1 3D tomography of baryon resonances

GPDs provide a new set of tools for characterizing hadron structure in QCD. Extending these concepts and methods from  $N \rightarrow N$  to  $N \rightarrow N^*$  transitions and using them to resonance structure is an objective of the transition GPD program.

One major application of  $N \rightarrow N$  GPDs is the 3D imaging of the quark/gluon structure of the nucleon. In a frame where the momentum transfer between the nucleon states is in the transverse direction,  $\xi = 0$  and  $\Delta_T \neq 0$ , the  $N \rightarrow N$  GPD  $H_q(x, \xi = 0, t = -\Delta_T^2)$  ( $q$  denotes the quark flavor) can be represented as the Fourier transform of a transverse coordinate distributions as (here  $x > 0$ )

$$\begin{aligned} H_q(x, \xi = 0, t = -\Delta_T^2) &= \int d^2b e^{i\Delta_T b} f_q(x, \mathbf{b}). \\ -H_q(-x, \xi = 0, t = -\Delta_T^2) &= \int d^2b e^{i\Delta_T b} f_{\bar{q}}(x, \mathbf{b}). \end{aligned} \quad (26)$$

The functions  $f_q(x, \mathbf{b})$  and  $f_{\bar{q}}(x, \mathbf{b})$  describe the distributions of quarks and antiquarks with momentum fraction  $x$  as a function of transverse position  $\mathbf{b}$ , in a nucleon state localized in transverse space at the origin [19, 20]. The representation provides a “tomographic image” of the nucleon’s quark/antiquark structure and reveals new information about the dynamical system, such as the average transverse radius of quarks/antiquarks and the change of the transverse distribution with  $x$ . Similar distributions describe the transverse distribution gluons [67, 68], of polarized quarks and gluons (helicity, transversity), and the distortions of the spatial distributions induced by transverse nucleon polarization (spin-orbit phenomena) [19, 20, 69].

Extending the transverse coordinate representation to  $N \rightarrow N^*$  transition GPDs is a subject of theoretical

research. The definition of localized transverse coordinate states in light-front quantization does not refer to the particle mass, so localized states can be defined  $N \rightarrow N^*$  transitions in the same way as for  $N \rightarrow N$ . The coordinate space densities associated with  $N \rightarrow \Delta$  GPDs can be studied using methods based on the large- $N_c$  limit of QCD (see Sec. 5.2) [70].

A special case of the transverse coordinate representation are the transverse densities of electric charge and magnetization in the nucleon [19, 20, 71, 72]. The transverse charge density in the nucleon is given by the Fourier transform of the  $N \rightarrow N$  Dirac electromagnetic form factor,

$$F_1(t = -\Delta_T^2) = \int d^2b e^{i\Delta_T b} \rho_1(\mathbf{b}). \quad (27)$$

The Dirac form factor is the integral of the GPD  $H_f$  over  $x$  (first moment), weighted with the quark charges and summed over quark flavors

$$F_1(t) = \sum_{q=u,d} e_q \int_{-1}^1 dx H_q(x, \xi = 0, t), \quad (28)$$

and the transverse charge density is the integral of the difference of quark and antiquark distributions

$$\rho_1(\mathbf{b}) = \sum_{q=u,d} e_q [f_q(x, \mathbf{b}) - f_{\bar{q}}(x, \mathbf{b})]. \quad (29)$$

In this way the transverse charge density provides summary information on the transverse coordinate distributions of quarks and antiquarks in the nucleon. In a similar way, the transverse magnetization density representing the Pauli form factor provides information on the transverse coordinate representation of the nucleon GPD  $E$ . The transverse charge and magnetization densities can be extracted directly from the experimentally measured electromagnetic form factors and provide interesting insight into nucleon structure; see Refs. [73–76] for empirical and theoretical studies. The concepts can be generalized from  $N \rightarrow N$  transitions to  $N \rightarrow N^*$  transitions. The  $N \rightarrow N^*$  transition charge/magnetization densities can be extracted directly from the transition form factors [77] and provide insight into the transverse spatial structure of the  $N \rightarrow N^*$  transition.

$N \rightarrow \Delta$  transition densities have been extracted from the  $N \rightarrow \Delta$  transition form factors [78]. An interesting aspect is the appearance of a quadrupole deformation in the transverse charge density due to the presence of a quadrupole form factor ( $\Delta J = 2$ ) in the  $N \rightarrow \Delta$  transition. The  $N \rightarrow \Delta$  densities have been studied theoretically in holographic and light-front quark models [79]. The transverse densities in hyperon

states have been studied using dispersion theory and EFT methods [80].

The transverse coordinate representation Eq. (26) is defined at  $\xi = 0$ , where the transverse coordinate distributions represent proper particle densities in the context of light-front quantization. The kinematics  $\xi = 0$  is not accessible in experiment, as actual scattering processes involve a longitudinal momentum transfer between the initial and final baryon; this applies to  $N \rightarrow N$  as well as  $N \rightarrow N^*$  transitions. It is generally not possible to extract  $x$ -dependent transverse distributions directly from experiment. Experimental information can be used to probe GPDs in other regions of the partonic variables. The program of nucleon tomography with GPDs therefore relies essentially on theoretical models predicting/constraining the behavior of GPDs. Lattice QCD calculations using the quasi/pseudo-distribution formulation can potentially provide direct information about the  $x$ -dependent GPDs at  $\xi = 0$  for use in hadron tomography (see Sec. 5.4).

#### 4.2 Spin and angular momentum in baryon resonances

Another major application of  $N \rightarrow N$  GPDs is the characterization of the angular momentum carried by the quark and gluon fields in the nucleon, including spin and orbital angular momentum. This is possible because the GPDs contain information on the nucleon matrix elements of the QCD energy momentum tensor (EMT), which enters into the definition of field-theoretical angular momentum in QCD. Expanding the nonlocal QCD operator in powers of the light-like separation of the quark fields, one obtains

$$\begin{aligned} & n_\alpha \bar{\psi}_q(-\tau n/2) \gamma^\alpha [\text{gauge link}] \psi_q(\tau n/2) \\ &= n_\alpha \bar{\psi}_q(0) \gamma^\alpha \psi_q(0) \\ &+ \frac{1}{2} n_\alpha n_\beta \bar{\psi}(0) \gamma^\alpha \overleftrightarrow{\nabla}^\beta \bar{\psi}(0) + \dots \end{aligned} \quad (30)$$

where  $\overleftrightarrow{\nabla}^\beta \equiv \frac{1}{2}(\overrightarrow{\partial}^\beta - \overleftarrow{\partial}^\beta) - igA^\beta$  is the QCD covariant derivative. The local spin-2 operator in the second term is the quark part of the EMT ( $q$  denotes the quark flavor),

$$T_q^{\alpha\beta}(0) \equiv i \bar{\psi}_q(0) \gamma^\alpha \overleftrightarrow{\nabla}^\beta \bar{\psi}_q(0). \quad (31)$$

The matrix elements of this operator between nucleon states can be obtained from the  $x$ -weighted integrals (second moments) of the  $N \rightarrow N$  GPDs. The angular momentum of quarks (and gluons) can be computed from its field-theoretical definition in terms of the EMT. As a result, the angular momentum of quarks

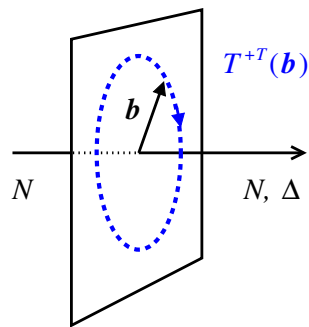


**Fig. 3** Transition angular momentum derived from transition transverse density of energy-momentum tensor, Eq.(36), for  $N \rightarrow \Delta$  transitions [30].

and gluons in the nucleon can be expressed as certain  $x$ -weighted integrals of the  $N \rightarrow N$  GPDs (spin sum rules) [53]. Several versions of these sum rules have been proposed, using different but equivalent definitions versions of the field-theoretical angular momentum; the relation between them is now well understood [81]. A field of study has emerged, exploring the angular momentum content of the nucleon based on GPDs using theoretical methods [16, 82], LQCD simulations [83–87], and experimental data.

The extension of the notion of QCD angular momentum to  $N \rightarrow N^*$  transitions is a subject of ongoing theoretical research. Some principal questions need to be addressed when generalizing the concept of angular momentum to transitions between states with different masses and quantum numbers (spin, isospin). The invariant formulation of the spin sum rule by Ji [53] uses specific properties of  $1/2 \rightarrow 1/2$  transitions, and the Breit frame formulation by Polyakov [88] assumes transitions between baryon states of equal mass.

A framework that is well suited for the generalization to  $N \rightarrow N^*$  transitions is the formulation of QCD angular momentum as a transverse density at fixed light-front time [82, 89, 90]. A definition of  $N \rightarrow N^*$  transition angular momentum based on this formulation has been proposed in Ref. [30]. One considers the transition matrix elements of the EMT between general baryon states with masses  $m$  and  $m'$  and 4-momenta  $p$  and  $p'$ ,

$$\langle B'(p', \lambda') | \hat{T}_q^{\alpha\beta}(0) | B(p, \lambda) \rangle. \quad (32)$$

The baryons can have different spin  $S' \neq S$ . The spin states are described as light-front helicity states; the light-front helicities  $\lambda$  and  $\lambda'$  are directly related to the spin projection along the the 3-axis in the baryon rest frame;  $\lambda \leftrightarrow S_3, \lambda' \leftrightarrow S'_3$ . One analyzes the transition matrix element Eq. (32) in a class of frames where the momentum transfer has  $\Delta^+ = 0$  and the average

momentum has  $\mathbf{P}_T = 0$  (generalized Drell-Yan-West frame). In these frames the light-cone components of the baryon momenta are given by (using the notation  $p = [p^+, p^-, \mathbf{p}_T]$  with  $p^\pm \equiv p^0 \pm p^3$ )

$$\begin{aligned} p &= \left[ p^+, \frac{m^2 + |\Delta_T|^2/4}{p^+}, -\frac{\Delta_T}{2} \right], \\ p' &= \left[ p^+, \frac{m'^2 + |\Delta_T|^2/4}{p^+}, \frac{\Delta_T}{2} \right], \\ \Delta &= \left[ 0, \frac{m'^2 - m^2}{p^+}, \Delta_T \right]. \end{aligned} \quad (33)$$

The matrix element in Eq. (32) thus becomes a function of  $\Delta_T$ , with  $t = -\Delta_T^2 < 0$ . Taking the light-front component  $+i$  of the EMT ( $i = 1, 2$ ) and performing the two-dimensional Fourier transform, one obtains the transverse coordinate density

$$\begin{aligned} T_q^{+i}(\mathbf{b}|S'_3, S_3) &= \int \frac{d^2\Delta_T}{(2\pi)^2} e^{-i\Delta_T \cdot \mathbf{b}} \langle B'(p', \lambda') | \hat{T}_q^{+i}(0) | B(p, \lambda) \rangle. \end{aligned} \quad (34)$$

The transition AM in the  $z$ -direction is then defined as

$$\begin{aligned} 2S^z(S'_3, S_3) J_{B \rightarrow B'}^q &= \frac{1}{2p^+} \int d^2b \left[ \mathbf{b} \times \mathbf{T}_q^{+T}(\mathbf{b}|S'_3, S_3) \right]^z, \end{aligned} \quad (35)$$

where  $S^z(S'_3, S_3)$  accounts for the kinematic spin dependence and  $J_{B \rightarrow B'}^q$  contains the dynamical information (reduced matrix element). This definition of the AM in the transverse coordinate representation has the form of a vector product of position and momentum and permits a simple mechanical interpretation (see Fig. 3); its properties and the equivalence with other definitions were established for  $N \rightarrow N$  transitions in Refs. [82, 89, 90]. In the momentum representation of the matrix element the transition AM is expressed as

$$\begin{aligned} 2S^z(S'_3, S_3) J_{B \rightarrow B'}^q &= \frac{1}{2p^+} \left[ -i \frac{\partial}{\partial \Delta_T} \times \langle B'(p', \lambda') | \hat{\mathbf{T}}_q^{+T}(0) | B(p, \lambda) \rangle \right]_{\Delta_T=0}^z. \end{aligned} \quad (36)$$

The kinematic spin vector is defined as (for transitions between baryon states with  $|S' - S| = 0, 1$ )

$$S^z(S'_3, S_3) = \sqrt{S(S+1)} \sqrt{\frac{2S'+1}{2S'+1}} \langle SS_3, 10 | S'_3 S'_3 \rangle, \quad (37)$$

where  $\langle SS_3, 10 | S'_3 S'_3 \rangle$  are the SU(2) Clebsch-Gordan coefficients. Equations (35) and (36) provide a general definition of the QCD AM associated with baryon transitions. Its implications should be explored in further research.

Lattice QCD	$J_{p \rightarrow p}^{u+d}$	$J_{\Delta^+ \rightarrow \Delta^+}^{u+d}$	$J_{p \rightarrow p}^{u-d}$	$J_{p \rightarrow \Delta^+}^{u-d}$	$J_{\Delta^+ \rightarrow \Delta^+}^{u-d}$
[83] $\mu^2 = 4 \text{ GeV}^2$	0.33*	0.33	0.41*	0.58	0.08
[84] $\mu^2 = 4 \text{ GeV}^2$	0.21*	0.21	0.22*	0.30	0.04
[85] $\mu^2 = 4 \text{ GeV}^2$	0.24*	0.24	0.23*	0.33	0.05
[86] $\mu^2 = 1 \text{ GeV}^2$	–	–	0.23*	0.33	0.05
[87] $\mu^2 = 4 \text{ GeV}^2$	–	–	0.17*	0.24	0.03

**Table 2** Estimates of the isoscalar and the isovector AM for  $p \rightarrow p$ ,  $p \rightarrow \Delta^+$  and  $\Delta^+ \rightarrow \Delta^+$  obtained from lattice QCD data on  $J_{p \rightarrow p}^{u+d}$  and  $J_{p \rightarrow p}^{u-d}$  and the relations provided by the leading-order  $1/N_c$  expansion. Input values are marked by an asterisk \*.

The transition AM definition Eq. (35) has been used to study the AM in  $N \rightarrow \Delta$  transitions [30]. Because of the isospin difference between the states, these transition probe the isovector component of the quark AM ( $u - d$ ). The  $N \rightarrow \Delta$  transition matrix elements of the EMT can be analyzed using the  $1/N_c$  of QCD, where  $N$  and  $\Delta$  states appear in the same representation of the emergent SU( $2N_f$ ) spin-flavor symmetry and transitions between them are connected by the symmetry (see Sec. 5.2). The main results of this analysis are:

(i) The isovector AM in the nucleon is leading in  $1/N_c$ ; the isoscalar is subleading:

$$J_{N \rightarrow N}^{u+d} = \mathcal{O}(N_c^0), \quad J_{p \rightarrow p}^{u-d} = \mathcal{O}(N_c). \quad (38)$$

This explains the observed large flavor asymmetry of the quark AM in the nucleon. Note that this scaling is consistent with that of the quark spin contribution to the nucleon spin as given by the axial coupling,  $g_A^{u+d} = \mathcal{O}(N_c^0)$  and  $g_A^{u-d} = \mathcal{O}(N_c^1)$ .

(ii) The isoscalar component of the AM in the nucleon and  $\Delta$  are related by

$$J_{N \rightarrow N}^{u+d} = J_{\Delta \rightarrow \Delta}^{u+d}. \quad (39)$$

This provides insight into the spin structure of  $\Delta$  resonance. Note that this relation is consistent with the spin sum rule for the  $\Delta$  state.

(iii) The isovector AM in the nucleon, the AM in the  $N \rightarrow \Delta$  transitions, and the isovector AM in the  $\Delta$  are related by

$$J_{p \rightarrow p}^{u-d} = \frac{1}{\sqrt{2}} J_{p \rightarrow \Delta^+}^{u-d} = 5 J_{\Delta^+ \rightarrow \Delta^+}^{u-d}. \quad (40)$$

This suggests that the  $N \rightarrow \Delta$  transition AM is large and provides a way to probe the isovector nucleon AM with  $N \rightarrow \Delta$  transition measurements.

Furthermore, within the  $1/N_c$  expansion one can obtain numerical estimates of the  $N \rightarrow \Delta$  transition AM, using Eq. (40) and lattice QCD results for the isovector EMT  $N \rightarrow N$  matrix elements [30]. Results are summarized in Table 2. The dominance of the isovector component of the quark angular momentum in  $N \rightarrow N$

transitions was also confirmed by a calculation using the light-cone wave function of the chiral soliton in the large- $N_c$  limit [70].

The  $N \rightarrow \Delta$  transition matrix element of the EMT can be connected with the  $N \rightarrow \Delta$  transition GPDs of the parity-even quark operator, Eq. (1) [16, 30]. In the context of the  $1/N_c$  expansion, the dominant  $N \rightarrow \Delta$  transition GPD is the GPD  $G_1^1$ , which scales as

$$G_1(x, \xi, t) \sim N_c^3 \times \text{function}(N_c x, N_c \xi, t). \quad (41)$$

In leading order of  $1/N_c$ , one obtains

$$\int_{-1}^1 dx x G_1(x, \xi, 0) = \frac{8}{3} J_{p \rightarrow \Delta^+}^{u-d}. \quad (42)$$

The  $N_c$  scaling of the second moment implied by Eq. (41) agrees with Eq. (38).

#### 4.3 Mechanical properties of baryon resonances

A further major application of  $N \rightarrow$  GPDs is the study of the so-called ‘‘mechanical properties’’ of the nucleon. The components of the EMT with 3-dimensional tensor and scalar character describe the distributions of mass/energy and forces/pressure in a mechanical system [21, 22, 88, 91]. The nucleon matrix elements of these EMT components can again be connected with the  $x$ -weighted integrals of the GPDs (second moments). The second moment of the  $N \rightarrow N$  GPD  $H$  contains two EMT form factors<sup>2</sup>

$$\int dx x H(x, \xi, t) = M_2(t) + \frac{4}{5} \xi^2 d_1(t). \quad (43)$$

$M_2(t)$  describes the distribution of mass/energy in the nucleon;  $d_1(t)$  describes the distribution of shear forces and pressure. An interpretation of these structures has been developed in terms of 3-dimensional spatial densities in the Breit frame ( $\Delta^0 = 0$ ). Determining these form factors and spatial distributions using theoretical and experimental methods data has become a major goal of nucleon structure physics.

The extension of these concepts to  $N \rightarrow N^*$  transitions would provide new tools for resonance structure physics. The distributions of mass/energy and pressure/forces would allow for new assessments of the size and spatial structure of resonances, correlated with their mass and spin. One present limitation is that the

<sup>1</sup>In the  $h_{M,E,C,A}$  convention employed in Ref. [44] the dominant in  $1/N_c$  unpolarized  $N \rightarrow \Delta$  GPD is  $h_M$ , which in leading order in  $1/N_c$  corresponds to  $\frac{4}{3}G_1$ .

<sup>2</sup>Because the EMT describes the coupling of matter to gravity, these form factors are also known as the ‘‘gravitational form factors’’ of the nucleon.

interpretation of the EMT form factors in terms of spatial densities uses 3D densities in the Breit frame and cannot readily be generalized to transitions between states with different masses. This could be overcome by using the framework of transverse densities at fixed light-front time, as in the definition of the transition AM, Eq. (35) [30].

In the large- $N_c$  limit the baryon masses are  $\mathcal{O}(N_c)$  and the baryon motion becomes effectively non-relativistic, so that the baryon mass does not play a role in transition matrix elements. In this situation the  $N \rightarrow N^*$  transition EMT form factors (and even the  $N^* \rightarrow N^*$  ones) permit an interpretation in terms of Breit frame densities in the same way as the  $N^* \rightarrow N$  form factors.

The  $d_1(t)$  form factor (the first coefficient of the Gegenbauer expansion of the so-called D-term [92]) is of special interest because it makes a determining contribution into the subtraction constant of the fixed- $t$  dispersion relation for the DVCS amplitude within the leading-twist approximation [16]. As such it can be extracted from the experimental data on the beam spin asymmetry (imaginary part of DVCS amplitude) and cross section (real part) without need for a GPD parametrization. Several extractions have been performed using existing experimental data, in particular from JLab CLAS 6 GeV [93–95]. It would be interesting to explore whether the DVCS dispersion relations could be generalized to  $N \rightarrow \Delta$  transitions, and whether there would be a connection with an  $N \rightarrow \Delta$  D-term. It should be noted that the amplitude of  $N \rightarrow \Delta$  DVCS is suppressed in the high-energy limit (non-diffractive process, quantum number exchange), so that the need for subtraction in a dispersion relation is not apparent. It is also known that the isovector D-term is suppressed in the  $1/N_c$  expansion [16]. In  $N \rightarrow N^*$  transitions to states with the same quantum numbers as the nucleon, the high-energy behavior of DVCS is the same as in  $N \rightarrow N$ , and a transition D-term might appear in the dispersion relation.

#### 4.4 Tensor charge and anomalous magnetic moment

For the GPDs of the ground state nucleon, the first moments of the transversity GPDs  $\bar{E}_T$  and  $H_T$  can be related [69, 96, 97] to the anomalous tensor magnetic moment  $k_T$  of the nucleon for the single quark flavors ( $u, d$ ):

$$k_T^{u,d} = \int dx \bar{E}_T^{u,d}(x, \xi = 0, t = 0) \quad (44)$$

and to the tensor charge  $\delta_T$ :

$$\delta_T^{u,d} = \int dx H_T^{u,d}(x, \xi = 0, t = 0). \quad (45)$$

Since relations between the transversity transition GPDs and the ground state transition GPDs can be found in the large  $N_c$  limit [26], it is assumed that similar relations exist for the transversity transition GPDs and allow an extraction of the equivalent properties for baryon resonances.

## 5 Theoretical methods for transition GPDs

### 5.1 Chiral dynamics in $N \rightarrow \pi N$ transitions

The simplest case of transition GPDs are transitions between  $N$  and  $\pi N$  states in the near-threshold region. If the center-of-mass momentum of the  $\pi N$  system in the final state is “small” of the order  $k \sim m_\pi$ , the emission of the pion is governed by chiral dynamics and can be computed from first principles (so-called soft-pion theorems) (see Fig. 4). Chiral dynamics is the effective long-range dynamics emerging from the spontaneous breaking of chiral symmetry in QCD, where the pion appears as a Goldstone boson, the form of its interaction with other hadrons is dictated by the chiral symmetry. In particular, chiral symmetry implies that the QCD isovector axial current  $J_{5V}^\mu$  produces low-momentum pions out of the vacuum and can be used as an interpolating QCD operator for pion states. In nucleon transition matrix elements, this allows one to derive relations between the  $N \rightarrow \pi N$  transition matrix elements of a QCD operator  $\mathcal{O}$  and the  $N \rightarrow N$  matrix elements of the commutator  $\mathcal{O}' = [\mathcal{O}, J_{5V}^\mu]$ ; schematically

$$\langle \pi N | \mathcal{O} | N \rangle \leftrightarrow \langle N | \mathcal{O}' | N \rangle, \quad \mathcal{O}' = [\mathcal{O}, J_{5V}^\mu] \quad (46)$$

These relations become predictive if the commutator can be reduced to an operator whose matrix elements are known using the field equations. Application of this method to near-threshold  $N \rightarrow \pi N$  transitions is demonstrated in Ref. [32]. The  $N \rightarrow \pi N$  transition GPDs measured in DVCS and meson production are considered in Refs. [33–35]. Higher-order corrections in the pion momentum can be computed using chiral EFT [98]. Applications to hard exclusive pion production with  $N \rightarrow \pi N$  transitions are discussed in Ref. [59]. The soft-pion theorems are practically applicable in S-wave of the  $\pi N$  system. In the P-wave, the strong  $\Delta$  resonance limits the useful range of the chiral expansion. In this channel other methods can be applied, such as extensions of chiral EFT including  $\Delta$  degrees of freedom [36, 37] or the  $1/N_c$  expansion (see Sec. 5.2).

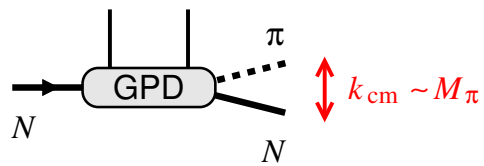


Fig. 4  $N \rightarrow \pi N$  transition GPD in the chiral regime

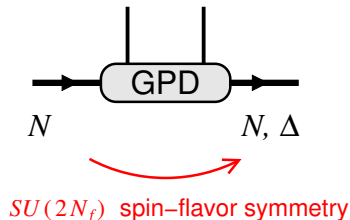


Fig. 5  $N \rightarrow N$  and  $N \rightarrow \Delta$  transition GPDs in the large- $N_c$  limit

### 5.2 $1/N_c$ expansion and $N \rightarrow \Delta$ transitions

The  $1/N_c$  expansion is a general method for analyzing QCD in the nonperturbative domain and connecting it with meson and baryon properties. The large- $N_c$  limit corresponds to a semi-classical limit of the quantum field theory, in which dynamics simplifies in characteristic ways (“string-like”) yet remains strongly coupled and generates meson/baryon spectra close to those observed in experiment [99, 100]. In the baryon sector, a dynamical spin-flavor symmetry emerges, whose ground-state representation consists of states with equal spin and isospin,  $S = I$  [101–103]. The  $N$  and  $\Delta$  appear as the states with  $S = I = 1/2$  and  $3/2$  in this representation. Matrix elements of QCD operators between  $N$  and  $\Delta$  states are therefore constrained by the spin-flavor symmetry (see Fig. 5). The transformation properties of QCD operators under the emergent spin-flavor symmetry can be inferred from model-independent considerations and are determined by their spin-flavor quantum numbers. The transition matrix between ground-state baryons are then connected by group-theoretical coefficients, similar to the matrix elements of spherical tensor operators between angular momentum states. Schematically,

$$\langle N(S'_3, I'_3) | \mathcal{O} | N(S_3, I_3) \rangle = C(\frac{1}{2} \frac{1}{2} | S'_3 I'_3, S_3 I_3 \rangle \langle \mathcal{O} \rangle, \quad (47)$$

$$\langle \Delta(S'_3, I'_3) | \mathcal{O} | N(S_3, I_3) \rangle = C(\frac{3}{2} \frac{1}{2} | S'_3 I'_3, S_3 I_3 \rangle \langle \mathcal{O} \rangle, \quad (48)$$

$$\langle \Delta(S'_3, I'_3) | \mathcal{O} | \Delta(S_3, I_3) \rangle = C(\frac{3}{2} \frac{3}{2} | S'_3 I'_3, S_3 I_3 \rangle \langle \mathcal{O} \rangle, \quad (49)$$

where  $S_3/I_3$  denote the spin/isospin projections,  $C$  are group-theoretical coefficients given by products of  $SU(2)$  vector coupling coefficients, and  $\langle \mathcal{O} \rangle$  is the reduced matrix element containing the dynamical information.

The relations Eqs. (47)–(49) can be used to derive the  $N \rightarrow \Delta$  and  $\Delta \rightarrow \Delta$  transition matrix elements of QCD operators from the  $N \rightarrow N$  matrix elements if the latter are known (measured, calculated in Lattice QCD). The method has extensively been applied to matrix elements of local QCD operators such as vector and axial vector currents, with very successful results [104–106]. It can also be applied to matrix elements of nonlocal light-ray operators, to predict the  $N \rightarrow \Delta$  transition GPDs in terms of the  $N \rightarrow N$  GPDs. Large- $N_c$  relations for the chiral-even transition GPDs are discussed in Ref. [16, 107] and applied to  $N \rightarrow \Delta$  DVCS processes. The extension to chiral-odd GPDs is discussed in Refs. [26, 31] and applied to hard exclusive pion production with  $N \rightarrow \Delta$  transitions.

The  $1/N_c$  expansion has other interesting applications to GPDs besides connecting  $N$  and  $\Delta$  transition matrix elements. It predicts the  $N_c$ -scaling of the reduced matrix element  $\langle \mathcal{O} \rangle$  in dependence on the spin-flavor quantum numbers of the operator and allows one to classify the matrix elements in leading and subleading ones. It also permits the calculation of  $1/N_c$  corrections to the leading-order relations of Eqs. (47)–(49). The  $1/N_c$  expansion can also be combined with chiral dynamics to enable quantitative predictions. One formulation is given by effective field theories (EFTs) based on a combined chiral and  $1/N_c$  expansion [108, 109]. Another formulation is the chiral quark-soliton model of baryons based on the dynamics of chiral constituent quarks [110]; this framework has been applied extensively to study GPDs and transition GPDs [16, 111].

### 5.3 Light-cone sum rules

Helicity-conserving elastic and transition form factors at very large momentum transfers can be calculated in QCD in terms of the light-cone distribution amplitudes (LCDAs) that describe momentum fraction distributions of valence quarks at small transverse distances. The problem is that the onset of the pQCD regime is postponed to very large  $Q^2$  because the factorizable contribution involves a small factor  $\sim (\alpha_s/(2\pi))^2$  and has to win over nonperturbative “soft” or “end-point” contributions that are suppressed by an extra power of  $Q^2$  but do not involve small coefficients. The light-cone sum rule (LCSR) technique [112] makes use of quark-hadron duality and dispersion relations to calculate such non-factorizable “soft” contributions in terms of the same LCDAs that enter the pQCD calculation and avoid double counting. Thus, the LCSRs provide one with the most direct relation between the hadron form factors and LCDAs that is available at present,

with no other nonperturbative parameters. This approach was initially developed to describe the weak decay  $\Sigma \rightarrow p\gamma$  [112]. It is very flexible, and has been applied to light- and heavy-meson decays (see, *e.g.*, [113] for a recent review), to elastic and transition baryon form factors [114–118] and pion electroproduction near threshold [119]. The current state-of-the art LCSRs have NLO accuracy. The LCSR technique proves to be very powerful, especially if used in combination with lattice QCD inputs on the LCDAs, which are gradually becoming more and more accurate, see *e.g.* [120].

### 5.4 Lattice QCD calculations

Aspects of GPDs have been investigated in lattice QCD for decades. Most of these calculations are based on the Mellin moments of GPDs, such as the electromagnetic and axial form factors of the proton, mainly because these are the most reliably extracted. Lattice calculations of these quantities have advanced significantly and now take into account sources of systematic uncertainties, such as physical pion mass calculations, excited states, infinite volume, and extrapolation to the continuum limit. Another crucial improvement is the inclusion of disconnected-diagram contributions that enable the extraction of the individual flavor quantities. Despite notable advancements, theoretical and computational constraints hinder the calculation of higher Mellin moments of GPDs, making the reconstruction of GPDs inherently challenging. Rather than relying solely on Mellin moments, alternative methods for determining the  $x$ -dependence of various distribution functions have emerged over time [121–129]. In the past decade, significant progress has been made in extending these methods to calculate  $x$ -dependent GPDs [39–41, 130–135]. Comprehensive reviews of recent progress in the field can be found in Refs [136–139]. This progress can also be extended to the calculation of transition GPDs, which offer another avenue for probing hadronic structure. There are only a few lattice QCD calculations limited to the transition form factors (see, *e.g.*, Refs. [140–143]).

## 6 Transition processes: electron scattering

Similar to the GPDs of the ground-state nucleon, transition GPDs are accessible in different lepton scattering reactions as well as hadronic reactions. In lepton production experiments, transition GPDs can be accessed by the  $N \rightarrow N^*$  deeply virtual Compton scattering (DVCS) and the  $N \rightarrow N^*$  deeply virtual meson production (DVMP) processes.

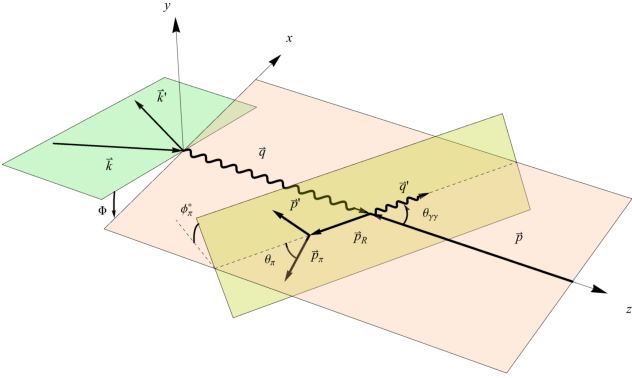


**Fig. 6** Planes defining the scattering angles that characterize the  $e^- N \rightarrow e^- \gamma \pi N$  process. The angles  $\Phi$  and  $\phi_\pi^*$  are defined with respect to the  $xz$ -plane, which is the scattering plane of the virtual photons with four-momenta  $q$  and  $q'$ . This figure is taken from Ref. [44].

### 6.1 $N \rightarrow \Delta$ , $N^*$ DVCS and transition GPDs

The non-diagonal DVCS reaction with a nucleon-to-resonance-transition can be accessed through the study of the hard exclusive process

$$\begin{aligned} e^-(k) + N(p) &\rightarrow e^-(k') + \gamma(q') + R(p_R) \\ &\rightarrow e^-(k') + \gamma(q') + \pi(p_\pi) + N(p'), \end{aligned} \quad (50)$$

in which the produced nucleon resonance  $R$  further decays into a  $\pi N$  system. The first studies of  $N \rightarrow \Delta(1232)$  non-diagonal DVCS were reported in Refs. [34, 144] and a generalization for the second nucleon resonance region was recently considered in Ref. [44].

The process (50), see Fig. 6 for the specification of kinematic quantities, is described in terms of 8 kinematical invariants, which can be chosen as

$$\begin{aligned} s &= (k + p)^2, \quad Q^2 = -q^2 \equiv (k' - k)^2, \quad x_B = \frac{Q^2}{2p \cdot q}, \\ t &= \Delta^2 \equiv (p_R - p)^2, \quad M_{\pi N}^2 = p_R^2 \equiv (p' + p_\pi)^2, \\ \Phi, \quad \theta_\pi^*, \quad \phi_\pi^*. \end{aligned} \quad (51)$$

Here  $\Phi$  is the angle between the leptonic plane and the production plane spanned by the vectors  $\vec{q}$  and  $\vec{q}'$  defined in the  $\gamma^*(q)N(p)$  Center-of-Mass System; and the angles  $\theta_\pi^*$ ,  $\phi_\pi^*$  denote, respectively, the polar and azimuthal angles of the rest frame of the  $\pi(p_\pi)N(p')$  system.

Instead of the pion polar angle  $\theta_\pi^*$ , it is sometimes instructive to consider the invariant mass of the  $\pi\gamma$  system  $M_{\pi\gamma}^2 = (p_\pi + q')^2$  as independent kinematical variable.

The sevenfold differential unpolarized cross section for the  $e^- N \rightarrow e^- \gamma \pi N$  reaction is expressed as

$$\begin{aligned} \frac{d\sigma}{dQ^2 dx_B dt d\Phi dM_{\pi N}^2 d\Omega_\pi^*} &= \frac{1}{(2\pi)^7} \frac{x_B y^2}{32Q^4 \sqrt{1 + \frac{4M_N^2 x_B^2}{Q^2}}} \\ &\times \frac{|\vec{p}_\pi^*|}{4M_{\pi N}} \sum_i \sum_f |\mathcal{M}(e^- N \rightarrow e^- \gamma \pi N)|^2, \end{aligned} \quad (52)$$

where  $y \equiv p \cdot q / p \cdot k$ ;  $d\Omega_\pi^* \equiv d\cos\theta_\pi^* d\phi_\pi^*$  is the solid angle of the produced pion; and  $|\vec{p}_\pi^*|$  is the value of the pion 3-momentum in the  $\pi N$  rest frame. The squared invariant amplitude  $|\mathcal{M}(e^- N \rightarrow e^- \gamma \pi N)|^2$  is averaged (summed) over the initial (final) particle helicities.

Another characteristic observable of the reaction (50) is the beam-spin asymmetry (BSA) defined as

$$BSA = \frac{d\sigma^+ - d\sigma^-}{d\sigma^+ + d\sigma^-}, \quad (53)$$

where  $d\sigma^\pm$  refer to the polarized cross sections with electron beam helicity  $\pm 1/2$ .

Analogously to the usual hard exclusive electro-production of photons off a nucleon, the amplitude of the process (50) obtains contributions from the Bethe-Heitler (BH) process, with the final-state real photon emitted off the lepton lines; and the DVCS process, in which the photon is produced from the hadron side. The BH contribution is a pure QED process, and the corresponding amplitude can be calculated exactly provided an input on the nucleon-to-resonance transition electromagnetic form factors.

Similarly to the diagonal DVCS case, for which factorization is proven [145, 146], we assume the validity of the QCD collinear factorization theorem for the non-diagonal DVCS in the generalized Bjorken kinematics (large  $Q^2$  and  $W^2 = (p + q)^2$ ; fixed  $x_B$ ;  $-t$  and  $W_{\pi N}^2$  of hadronic mass scale:  $-t, W_{\pi N}^2 \ll Q^2$ ). Therefore, to the leading twist-2 accuracy, the reaction proceeds through the reaction mechanism of Fig. 7; and the corresponding amplitude is parameterized in terms of  $N \rightarrow R$  transition GPDs.

The interference between the BH and the non-diagonal DVCS leads to the interference term in the cross section. The BH process is usually expected to dominate the measured cross section for the kinematics accessible with current lepton scattering experiments and has to be subtracted in order to extract the non-diagonal DVCS signal.

As a first example we briefly review the description of the  $e^- N \rightarrow e^- \gamma \Delta(1232) \rightarrow e^- \gamma \pi N$  process. The corresponding invariant amplitude entering the cross section



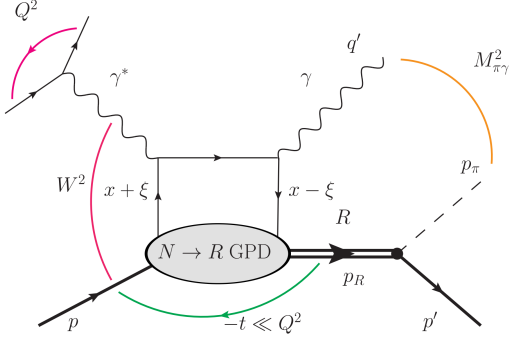


**Fig. 7** Handbag mechanism for the  $N \rightarrow \Delta$ ,  $N^*$  DVCS process. The diagram with the crossed real and virtual photon lines is not shown.

tion of Eq. (52) is given by:

$$\begin{aligned} \mathcal{M}(e^- N \rightarrow e^- \gamma \Delta \rightarrow e^- \gamma \pi N) &= \bar{C}_{iso} \frac{f_{\pi N \Delta}}{m_\pi} (-p_\pi)^\alpha \\ &\times \bar{N}(p', s'_N) \frac{i P_{\alpha\beta}^{(3/2)}(p_R)}{M_{\pi N}^2 - M_R^2 + i M_R \Gamma_\Delta(M_{\pi N})} \\ &\times \mathcal{M}_R^\beta(e^- N \rightarrow e^- \gamma \Delta), \end{aligned} \quad (54)$$

where  $\mathcal{M}_R^\beta(e^- N \rightarrow e^- \gamma \Delta)$  is defined as the sum of the BH and DVCS amplitudes;  $f_{\pi N \Delta} \simeq 2.08$  is the  $\pi N \Delta$  coupling constant of the effective  $\pi N \Delta$  Lagrangian (see Eq. (45) of Ref. [44]) determined from the  $\Delta \rightarrow \pi N$  decay width. The isospin factor  $\bar{C}_{iso}$  takes on the values  $\bar{C}_{iso} = \sqrt{\frac{2}{3}}$  for  $\Delta^+ \rightarrow \pi^0 p$ ; and  $\bar{C}_{iso} = -\sqrt{\frac{1}{3}}$  for  $\Delta^+ \rightarrow \pi^+ n$ . Furthermore, in Eq. (54),  $P_{\alpha\beta}^{(3/2)}(p_R)$  denotes the spin- $\frac{3}{2}$  projector, cf. Ref. [60].

The amplitude (54) results in the specific angular distribution for the decay pion in the resonance rest frame:

$$\begin{aligned} \mathcal{M}(e^- N \rightarrow e^- \gamma \Delta \rightarrow e^- \gamma \pi N) &= \bar{C}_{iso} \frac{f_{\pi N \Delta}}{m_\pi} \sqrt{\frac{4\pi}{3}} \frac{i |\vec{p}_\pi^*| [(M_{\pi N} + M_N)^2 - m_\pi^2]^{1/2}}{M_{\pi N}^2 - M_R^2 + i M_R \Gamma_\Delta(M_{\pi N})} \\ &\times \sum_{\lambda_R} \mathcal{M}(e^- N \rightarrow e^- \gamma \Delta(M_{\pi N}, \lambda_R)) \\ &\times \sum_{\lambda'} \langle 1\lambda', \frac{1}{2}s'_N | \frac{3}{2}s_R \rangle Y_{1\lambda'}(\Omega_\pi^*), \end{aligned} \quad (55)$$

where  $Y_{lm_i}(\Omega_\pi^*)$  denote the spherical harmonic functions and  $\langle ss_z, lm_l | JM \rangle$  are the Clebsch-Gordan coefficients for the  $\Delta \rightarrow \pi N$  decay.

Eq. (55) is instrumental in computing the resonance angular distributions of the cross-section. It is particularly instructive to present the cross section (52) integrated over the complete pion solid angle or integrated over the invariant mass of the  $\pi N$  system  $M_{\pi N}^2$ . It is worth mentioning that, assuming the Breit-Wigner form of the spectral function  $\Gamma_\Delta(M_{\pi N})$  together with

the narrow resonance limit  $\Gamma_R \ll M_R$ , the unpolarized cross section (52) integrated both in  $\Omega_\pi^*$  and  $M_{\pi N}^2$

$$\begin{aligned} &\int dM_{\pi N}^2 \int d\Omega_\pi^* \frac{d\sigma}{dQ^2 dx_B dt d\Phi dM_{\pi N}^2 d\Omega_\pi^*} \\ &\approx \frac{1}{(2\pi)^4} \frac{x_B y^2}{32 Q^4 \sqrt{1 + \frac{4M_N^2 x_B^2}{Q^2}}} \\ &\times \overline{\sum_i \sum_f} |\mathcal{M}(e^- N \rightarrow e^- \gamma \Delta(M_R, \lambda_R))|^2, \end{aligned} \quad (56)$$

where the sum runs over the final helicities of  $e^-$ ,  $\gamma$ , and  $\Delta$ , turns out to be fully consistent with the result for a stable particle [16].

A very instructive piece of information can be revealed through working out the pion polar angular distribution integrated over the azimuthal angle  $\phi_\pi^*$  within the narrow resonance approximation:

$$\begin{aligned} &\int dM_{\pi N}^2 \frac{d\sigma}{dQ^2 dx_B dt d\Phi dM_{\pi N}^2 d\cos\theta_\pi^*} \\ &\approx \frac{1}{(2\pi)^4} \frac{x_B y^2}{32 Q^4 \sqrt{1 + \frac{4M_N^2 x_B^2}{Q^2}}} \overline{\sum_{e,N} \sum_{e,\gamma}} (\bar{C}_{iso})^2 \\ &\times \left\{ \frac{1}{4} (1 + 3 \cos^2 \theta_\pi^*) \sum_{\lambda_R = \pm 1/2} |\mathcal{M}(e^- N \rightarrow e^- \gamma \Delta)|^2 \right. \\ &\quad \left. + \frac{3}{4} \sin^2 \theta_\pi^* \sum_{\lambda_R = \pm 3/2} |\mathcal{M}(e^- N \rightarrow e^- \gamma \Delta)|^2 \right\}, \end{aligned} \quad (57)$$

resulting in specific polar angular distributions for the  $\Delta$  helicity states  $\lambda_R = \pm 1/2$  and  $\lambda_R = \pm 3/2$ . This gives rise to a peculiar ‘‘autopolarization’’ effect providing access to information on different polarization states of the produced  $\Delta$ -resonance. For a sufficiently detailed experimental angular resolution, this can open interesting options for a precise partial wave analysis of  $\Delta$ -resonance production.

The cross-section estimates of  $N \rightarrow \Delta(1232)$  in Refs. [34, 144] were based on a model for the  $N \rightarrow \Delta$  transition GPDs dominant in the large- $N_c$  limit within the framework developed in Ref. [107]. The three dominant  $N^p \rightarrow \Delta^+$  transition GPDs  $h_M$ ,  $C_1$  and  $C_2$  are related to the following combinations of nucleon isovector GPDs [16, 107]:

$$\begin{aligned} h_M(x, \xi, \Delta^2) &= \sqrt{2} [E^u(x, \xi, \Delta^2) - E^d(x, \xi, \Delta^2)]; \\ C_1(x, \xi, \Delta^2) &= \sqrt{3} [\tilde{H}^u(x, \xi, \Delta^2) - \tilde{H}^d(x, \xi, \Delta^2)]; \\ C_2(x, \xi, \Delta^2) &= \frac{\sqrt{3}}{4} [\tilde{E}^u(x, \xi, \Delta^2) - \tilde{E}^d(x, \xi, \Delta^2)]. \end{aligned} \quad (58)$$

The control of the accuracy of this approximation is performed through a comparison of the first moments

of (58) to values of the corresponding form factors, see discussion in Ref. [60].

In Ref. [44] this model was employed to provide estimates of the cross section for the kinematical setup accessible with CLAS12@JLab. The phenomenological input included the nucleon GPD model of Sec. 2.7.2 of Ref. [60]. The GPD  $\tilde{E}$  is determined by the pion pole contribution, see Sec. 2.4.2 of Ref. [16]. For the relevant transition electromagnetic form factors, the results of the MAID2007 analysis reported in [64, 147] were employed.

In the upper panels of Fig. 8 we present the dependence of the cross-section (52)  $e^-p \rightarrow e^- \gamma \Delta(1232) \rightarrow e^- \gamma \pi^+ n$  integrated over the pion solid angle  $d\Omega_\pi^*$  on the invariant mass of the  $\pi^+ n$  system ( $M_{\pi N}$ ). The kinematic cut  $M_{\pi\gamma} > 1$  GeV is imposed to reduce the resonating background from the  $\gamma\pi$  subsystem arising from the  $e^-p \rightarrow e^- \rho^+ n \rightarrow e^- \gamma \pi^+ n$  process. The angle between the leptonic and production planes  $\Phi$  is set to  $90^\circ$  to maximize the BSA. We note that the non-diagonal  $N \rightarrow \pi N$  DVCS process in the  $\Delta(1232)$  region is dominated by the  $\pi^0$ -pole contribution into the  $N \rightarrow \Delta$  polarized transition GPD  $C_2$ . It is interesting that in the  $\Delta(1232)$  resonance region, for  $Q^2 = 2.3$  GeV<sup>2</sup>, the model estimates show the change from being dominated by the BH contribution for  $-t = 0.5$  GeV<sup>2</sup> to being DVCS-dominated for  $-t = 1.0$  GeV<sup>2</sup>. Such behavior is unlike the DVCS process on a nucleon in similar valence region kinematics, for which the BH dominates in both cases. This can, probably, be attributed to an effect of kinematic power correction proportional to  $t/Q^2$  and  $M_N^2/Q^2$  [148] that stays large for  $Q^2 = 2.3$  GeV<sup>2</sup>. For larger  $Q^2 = 5$  GeV<sup>2</sup> the dominance of BH over the DVCS seems to be restored. The lower panels of Fig. 8 present the corresponding BSA (53), as a function of  $M_{\pi N}$ . It originates from the BH and DVCS interference, and in the lower range of  $-t$  is estimated to be in the range of 10% with a tendency to slightly decrease with growth of  $-t$ .

Ref. [44] also presented a generalization of the formalism for the second resonance region, including the contribution of  $P_{11}(1440)$ ,  $D_{13}(1520)$  and  $S_{11}(1535)$  resonances with isospin- $\frac{1}{2}$ . This required the construction of phenomenological models for the corresponding twist-2 unpolarized and polarized transition GPDs, see Sec. 3.2: (2 of each for the spin- $\frac{1}{2}$  resonances and 4 of each for the spin- $\frac{3}{2}$  resonance). Let us briefly summarize the key ingredients and the phenomenological input.

- The unpolarized transition GPDs were constructed relying on the constraints for the corresponding first Mellin moments in terms of the transition electromagnetic form factors  $F_{1,2}^{NP_{11}}$ ,  $F_{1,2,3}^{ND_{13}}$ , and  $F_{1,2}^{NS_{11}}$  available from the MAID2007 and MAID2008 anal-

yses detailed in Ref. [64]. The  $x$  and  $\xi$  dependence of GPDs was provided by two types of models:

- I:  $\xi$ -independent valence PDF type parametrization;
- II: the Radyushkin double distribution Ansatz with a usual  $b$ -dependent profile with  $b = 1$  and the same valence PDF used as input.

In fact, model I turns out to be the  $b = \infty$  limit of model II. The comparison of the results of the two models allows us to roughly quantify the sensitivity of the non-diagonal DVCS observables to the quark momentum fraction and skewness dependence of GPDs.

- The polarized transition GPDs  $\tilde{H}_1^{pP_{11}}$ ,  $\tilde{H}_1^{pD_{13}}$ ,  $\tilde{H}_1^{pS_{11}}$  were modeled relying on the normalization provided by the PCAC through the generalized Goldberger-Treiman relations for the dominant axial transition FFs and adopting the dipole form for the  $t$ -dependence with the  $x$  and  $\xi$  dependence from the two types of models (I and II) described above.
- Finally, the GPDs  $\tilde{H}_2^{pP_{11}}$ ,  $\tilde{H}_2^{pD_{13}}$ ,  $\tilde{H}_2^{pS_{11}}$  were modeled assuming the pion pole dominance with the asymptotic form of the pion distribution amplitude.
- GPDs  $H_4^{pD_{13}}$ ,  $\tilde{H}_3^{pD_{13}}$ ,  $\tilde{H}_4^{pD_{13}}$ , for which no phenomenological constraints are available, were neglected.

Fig. 9 presents the  $M_{\pi N}$  invariant mass dependence in the first and second nucleon resonance regions of the  $e^-p \rightarrow e^- \gamma \pi^+ n$  cross section and corresponding BSA with the cut  $M_{\pi\gamma} > 1$  GeV to minimize the possible contamination from the  $\rho^+$  production channel.

We first notice from the cross section behavior that, with increasing values of  $-t$ , the second nucleon resonance region becomes more important relative to the  $\Delta(1232)$  resonance region. This can be explained due to the  $\gamma^* N \Delta$  transition form factors dropping faster with increasing  $-t$  value in comparison with the corresponding ones for the  $D_{13}(1520)$  and  $S_{11}(1535)$  resonances. Moreover, in the second nucleon resonance region, the  $D_{13}(1520)$  excitation provides the largest contribution, followed by the  $S_{11}(1535)$  resonance. On the other hand, the contribution of the  $P_{11}(1440)$  excitation to the unpolarized cross section is only very small. For the BSA, one notices that at  $-t = 0.5$  GeV<sup>2</sup> it reaches a value of around 10% in the  $\Delta$ -resonance region and shows a sharp drop in the second resonance region. Fig. 9 also shows that, with an increasing value of  $-t$ , the BSA for the  $D_{13}(1520)$  displays a sign change, resulting in a positive BSA in the second nucleon resonance region at  $-t = 1$  GeV<sup>2</sup>.

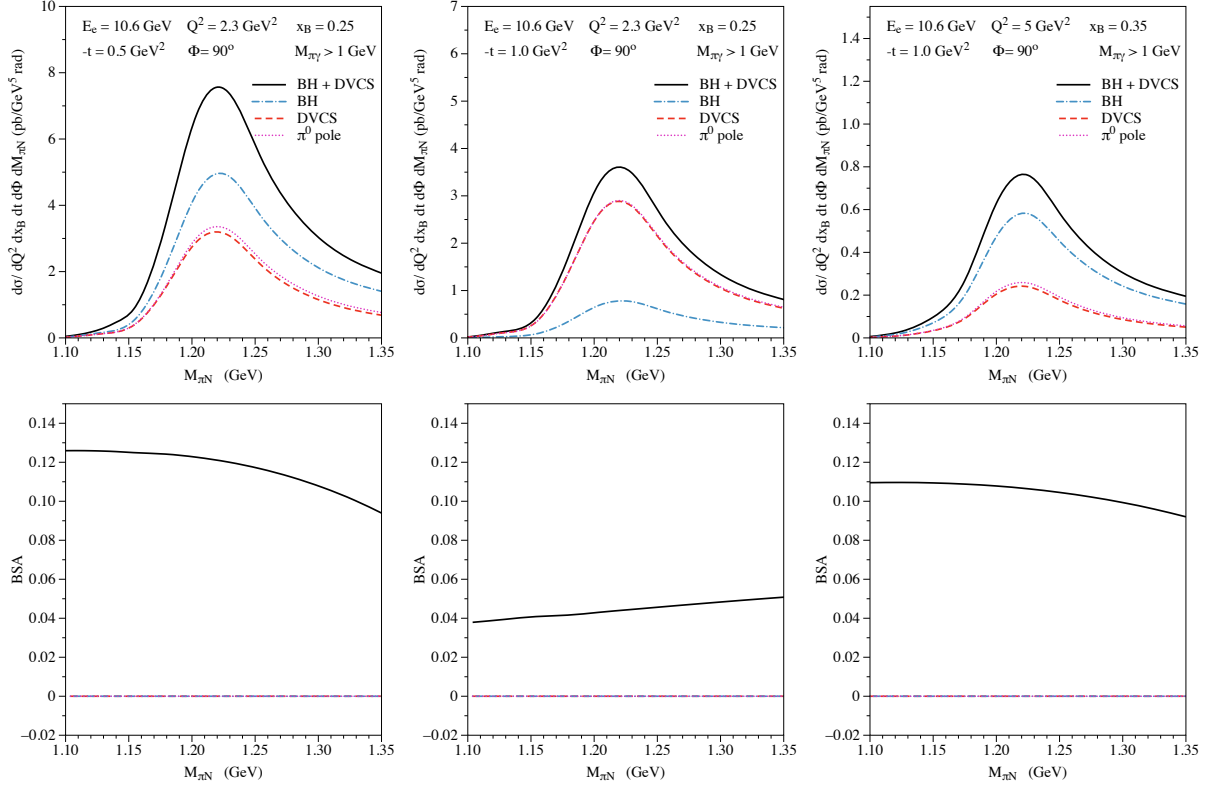


**Fig. 8** Dependence on the invariant mass of the  $\pi^+n$  system ( $M_{\pi N}$ ) of the  $e^-p \rightarrow e^-\gamma\Delta(1232) \rightarrow e^-\gamma\pi^+n$  cross section (upper panels) integrated over the pion solid angle, with the cut  $M_{\pi\gamma} > 1$  GeV, and corresponding beam-spin asymmetry (lower panels), for three kinematical setups accessible with CLAS12@JLab. Blue dashed-dotted curves:  $p \rightarrow \Delta(1232)$  BH process; red dashed curves:  $p \rightarrow \Delta(1232)$  DVCS process; black solid curves: BH + DVCS processes. The magenta dotted curves show the  $\pi^0$ -pole contribution to the  $p \rightarrow \Delta(1232)$  DVCS process separately. This figure is taken from Ref. [44].

## 6.2 $N \rightarrow N^*$ DVMP and transition GPDs

While the  $N \rightarrow N^*$  DVCS process is only sensitive to the twist-2 transition GPDs, the  $N \rightarrow N^*$  DVMP process

$$\gamma^* N \rightarrow \text{meson } N^* \rightarrow \text{meson } [N \text{ meson}], \quad (59)$$

which is shown schematically in Fig. 10, can be used to access all 16 transition GPDs, including the transversity transition GPDs.

Due to the possible different mesons that can be produced and due to the different decay channels of the resonance, a whole series of  $N \rightarrow N^*$  DVMP processes can be studied, for example:

1.  $\gamma^* p \rightarrow \pi^- N^{*++}$
2.  $\gamma^* p \rightarrow \pi^0 N^{*+}$
3.  $\gamma^* p \rightarrow \rho^0 N^{*+}$
4.  $\gamma^* p \rightarrow \pi^+ N^{*0}$
5.  $\gamma^* n \rightarrow \pi^+ N^{*-}$

with a nucleon or a delta resonance  $N^*$ . Furthermore, deeply virtual Kaon production in relation to hyperons like the  $\Lambda$  is possible and enables the study of transitions related to the strangeness sector. Flavor symmetry

relates the proton-hyperon GPDs to the proton-proton ones [149], *e.g.*

$$K_i(p - \Lambda) = -\frac{1}{\sqrt{6}} \left( 2K_i^u - K_i^d - K_i^s \right) \quad (60)$$

where  $K_i$  is a GPD. Predictions for the kaon-hyperon channels can be made analogously to those for pion production [150].

For DVMP reactions, the cross-section is given by [151]:

$$\frac{d^4\sigma}{dsdQ^2d\phi dt} \propto \left[ \frac{d\sigma_T}{dt} + \varepsilon \frac{d\sigma_L}{dt} + \varepsilon \cos 2\phi \frac{d\sigma_{TT}}{dt} + \sqrt{2\varepsilon(1+\varepsilon)} \cos \phi \frac{d\sigma_{LT}}{dt} + h\sqrt{2\varepsilon(1-\varepsilon)} \frac{d\sigma_{LT'}}{dt} \sin \phi \right]. \quad (61)$$

Here the terms  $\sigma_L, \sigma_T, \sigma_{LT}, \sigma_{LT'}, \sigma_{TT}$  correspond to the interaction of longitudinally ( $L$ ) and transversely ( $T$ ) polarized virtual photons,  $\phi$  is the angle between the leptonic and hadronic planes, and  $\varepsilon$  is the polarization of the virtual photon, representing the ratio of longitudinal to transverse photon flux.

As a first reaction, hard exclusive  $\pi^- \Delta^{++}$  electroproduction:

$$\gamma^* p \rightarrow \pi^- \Delta^{++} \rightarrow \pi^- [p \pi^+], \quad (62)$$

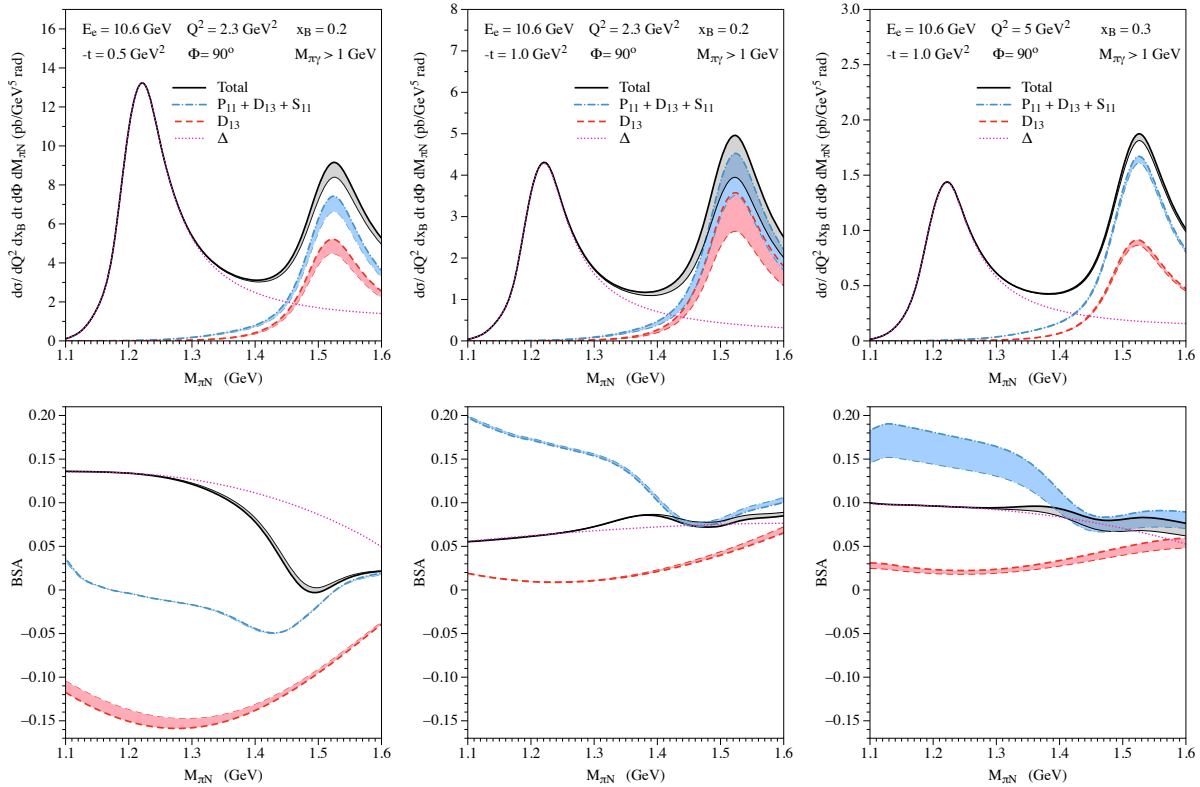


**Fig. 9** Dependence on the invariant mass of the  $\pi^+n$  system ( $M_{\pi N}$ ) of the  $e^-p \rightarrow e^-\gamma R \rightarrow e^-\gamma\pi^+n$  cross section (upper panels) and corresponding beam-spin asymmetry (lower panels), integrated over the decay pion solid angle, with the cut  $M_{\pi\gamma} > 1$  GeV, for three kinematics accessible at CLAS12@JLab. Magenta dotted curves: BH + DVCS process for  $R = \Delta(1232)$ ; red dashed curves and red bands: BH + DVCS process for  $R = D_{13}(1520)$ ; blue dashed-dotted curves and blue bands: BH + DVCS process for  $R = P_{11}(1440) + D_{13}(1520) + S_{11}(1535)$ ; black solid curves and grey bands: BH + DVCS process for  $R = \Delta(1232) + P_{11}(1440) + D_{13}(1520) + S_{11}(1535)$ . The thin (thick) curves represent the result of model I (model II) for  $x$  and  $\xi$  dependence of  $N \rightarrow R$  GPDs, see a description in the text. The bands indicate the corresponding variation due to the modeling. This figure is taken from Ref. [44].

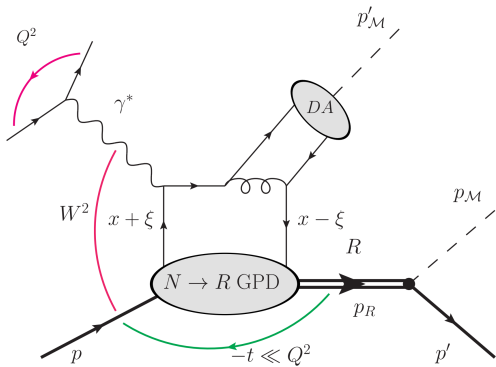


**Fig. 10** Schematic drawing of the  $N \rightarrow N^*$  DVMP process.

has been theoretically described based on transition GPDs in Ref. [26]. The process is expected, but not proven yet, to factorize under the same conditions as the  $N \rightarrow N^*$  DVCS process. At present, nothing is known about the  $p - \Delta$  GPDs neither from experiment nor from theory leaving aside a few relations between the  $p - p$  and the  $p - \Delta$  GPDs obtained in the large- $N_c$

limit [18, 26, 107]. One may expect, however, that the process  $\gamma^*p \rightarrow \pi^- \Delta^{++}$  is under control of similar dynamics as  $\gamma^*N \rightarrow \pi N'$ . From HERMES and the JLab experiments, we learned that the transverse cross section is much larger than the longitudinal one for the  $\pi^0 p$  channel. For charged pions, there is a strong contribution from the pion pole to the longitudinal amplitudes. The pole is to be treated as a one-boson-exchange contribution in the experimentally accessible range of kinematics since its contribution evaluated from the GPD  $\tilde{E}$  is too small [152]. Based on this expectation and with the help of large- $N_c$  results first, admittedly rough, estimates of the  $\pi^- \Delta^{++}$  cross sections have been given in [26].

The helicity amplitudes for longitudinally polarized photons, which are fed by twist-2 contributions, reads ( $e_0$  is the positron charge)

$$\mathcal{M}_{0\lambda_R, 0\lambda_N}^{tw2} = e_0 \int_{-1}^1 dx \mathcal{H}_{0+0+}^{\pi} \left[ A_{\lambda_R+, \lambda_N+}^{\Delta} - A_{\lambda_R-, \lambda_N-}^{\Delta} \right], \quad (63)$$

where  $\mathcal{H}_{0\lambda,0\lambda}^\pi$  is the leading-twist amplitude for the hard partonic subprocess  $\gamma^*q(\lambda) \rightarrow \pi q(\lambda)$  ( $\lambda = \pm\frac{1}{2}$ ) and

$$A_{\lambda_R\lambda,\lambda_N\lambda}^\Delta = \int \frac{dz^-}{2\pi} e^{ixP^+z^-} \langle \Delta^{++}(p_R, \lambda_R) | \times \bar{u}(-z/2) \frac{1}{4} \gamma^+ (1 + 2\lambda) \gamma_5 d(z/2) | p(p, \lambda_N) \rangle_{z^+=0, z_\perp=0}. \quad (64)$$

To the difference of the  $A^\Delta$ s in Eq. (63) only the odd-parity GPDs  $\tilde{G}_i$  (2) contribute.

The amplitudes for transversally polarized photons ( $\mu = \pm 1$ ) read

$$\begin{aligned} & \mathcal{M}_{0\lambda_R, \mu\lambda_N}^{tw3} \\ &= e_0 \int_{-1}^1 dx \left[ \mathcal{H}_{0-, \mu+}^\pi A_{\lambda_R-, \lambda_N+}^\Delta + \mathcal{H}_{0+, \mu-}^\pi A_{\lambda_R+, \lambda_N-}^\Delta \right], \end{aligned} \quad (65)$$

where

$$\begin{aligned} & A_{\lambda_R-\lambda, \lambda_N\lambda}^\Delta = \int \frac{dz^-}{2\pi} e^{ixP^+z^-} \langle \Delta^{++}(p_R, \lambda_R) | \\ & \times -\lambda \frac{i}{2} \bar{u}(-z/2) (\sigma^{+1} - 2\lambda\sigma^{+2}) d(z/2) | p(p, \lambda_N) \rangle_{z^+=0, z_\perp=0} \end{aligned} \quad (66)$$

to which the transversity GPDs (6) contribute. The pion wave function appearing in  $\mathcal{H}_{0-\lambda, \mu\lambda}^\pi$ , is of twist-3 nature. The matrix elements  $A^\Delta$  as well as the helicity amplitudes are explicitly given in terms of the transition GPDs in [26]. The subprocess amplitudes,  $\mathcal{H}^\pi$ , can be found in [152]. They have been calculated within the so-called modified perturbative approach in which the quark transverse momenta and the Sudakov suppressions are taken into account.

In the large- $N_c$  limit, the following relations between the  $p - \Delta^{++}$  transition GPDs and the proton-proton ones are found [18, 107]

$$\tilde{G}_3 = \frac{3}{2} (\tilde{H}^u - \tilde{H}^d) \quad \tilde{G}_4 = \frac{3}{8} (\tilde{E}^u - \tilde{E}^d) \quad (67)$$

and [26]

$$G_{T5} + \frac{1}{2} G_{T7} = -\frac{3}{2} (H_T^u - H_T^d). \quad (68)$$

Neglecting either  $G_{T5}$  (scenario I) or  $G_{T7}$  (scenario II) as well as all other transversity and odd-parity GPDs except of  $\tilde{G}_3$  and  $\tilde{G}_4$  and making use of the parametrization of the proton-proton GPDs advocated for in [153, 154], one is in the position to evaluate the helicity amplitudes (63) and (65). In addition to the GPD contributions one has to take into account also the pion-pole contribution which reads [26]

$$\begin{aligned} & \mathcal{M}_{0\lambda_R, \mu\lambda_N}^{pole} \\ &= e_0 \frac{Q\pi\Delta}{t - m_\pi^2} \bar{u}_\delta(p_R, \lambda_R) \frac{\Delta^\delta}{M_N} u(p, \lambda_N) (q - 2q')_\rho \epsilon^\rho(q, \mu), \end{aligned} \quad (69)$$

where

$$\varrho_{\pi\Delta} = \sqrt{2} g_{\pi\Delta^{++}p} F_{\pi\Delta p}(t) F_\pi(Q^2). \quad (70)$$

The coupling of the pion to the proton and the  $\Delta^{++}$  is described by a coupling constant,  $g_{\pi\Delta^{++}p}$ , and a  $t$ -dependent form factor  $F_{\pi\Delta p}$ . The last item in Eq. (70),  $F_\pi(Q^2)$ , is the electromagnetic form factor of the pion. The photon polarization vector is denoted by  $\epsilon$ . The photon and meson momenta are denoted by  $q$  and  $q'$ , respectively. The longitudinal pole contribution dominates over the transversal ones. The transversal/longitudinal ratio of the pole contributions is proportional to  $1/Q$  as is the case for the corresponding ratio of the amplitudes (65) and (63).

With the above described model for the  $p - \Delta$  GPDs and the pion-pole contribution, the partial cross sections

$$\begin{aligned} \frac{d\sigma_L}{dt} &= \frac{\sum_{\lambda_R} |\mathcal{M}_{0\lambda_R, 0+}|^2}{16\pi(W^2 - M_N^2) \sqrt{\Lambda(W^2, -Q^2, M_N^2)}}, \\ \frac{d\sigma_T}{dt} &= \frac{\sum_{\lambda_R} [|\mathcal{M}_{0\lambda_R, ++}|^2 + |\mathcal{M}_{0\lambda_R, -+}|^2]}{32\pi(W^2 - M_N^2) \sqrt{\Lambda(W^2, -Q^2, M_N^2)}}, \\ \frac{d\sigma_{TT}}{dt} &= -\frac{\sum_{\lambda_R} \text{Re}[\mathcal{M}_{0\lambda_R, ++}^* \mathcal{M}_{0\lambda_R, -+}]}{16\pi(W^2 - M_N^2) \sqrt{\Lambda(W^2, -Q^2, M_N^2)}}, \\ \frac{d\sigma_{LT}}{dt} &= -\sqrt{2} \frac{\sum_{\lambda_R} \text{Re}[\mathcal{M}_{0\lambda_R, 0+}^* (\mathcal{M}_{0\lambda_R, ++} - \mathcal{M}_{0\lambda_R, -+})]}{32\pi(W^2 - M_N^2) \sqrt{\Lambda(W^2, -Q^2, M_N^2)}}. \end{aligned} \quad (71)$$

for the  $\pi^- \Delta^{++}$  channel are evaluated. The results at  $Q^2 = 2.48 \text{ GeV}^2$  and a Bjorken- $x$  of  $x_B = 0.27$  are shown in Figs. 11, 12 as a function of  $t' = t - t_0$  (see Eq. (5)) and compared to the cross sections for the  $\pi^+ n$  channel. Note that the  $t_0$ -values are quite different in both processes ( $t_0 = -0.323 (-0.088) \text{ GeV}^2$  for the  $\pi^- \Delta^{++}$  ( $\pi^+ n$ ) channel at the quoted kinematics). The amplitudes in (71) are the sum of the GPD and the pole contributions. The Mandelstam function is

$$\begin{aligned} \Lambda(W^2, Q^2, M_N^2) &= W^4 + Q^4 + M_N^4 + 2W^2Q^2 \\ & \quad - 2W^2M_N^2 + 2Q^2M_N^2. \end{aligned} \quad (72)$$

As is to be seen from Fig. 11 the longitudinal cross section is large. The reason for this feature is a strong contribution from the pion pole. For the other partial cross sections there are substantial differences between the two scenarios. Particularly interesting is the opposite sign of  $d\sigma_{TT}$  for the  $\pi^- \Delta^{++}$  and the  $\pi^+ n$  channels. The dominant contribution to  $d\sigma_{TT}$  comes from an interference of a twist-3 helicity non-flip amplitude being proportional to the convolution  $\langle H_T \rangle$  (in the large- $N_c$  limit for the  $\pi^- \Delta^{++}$  channel), and a pion-pole contribution. The  $Q^2$  and  $x_B$  dependencies of the  $\pi^- \Delta^{++}$  partial cross sections are similar to those of the  $\pi^+ n$

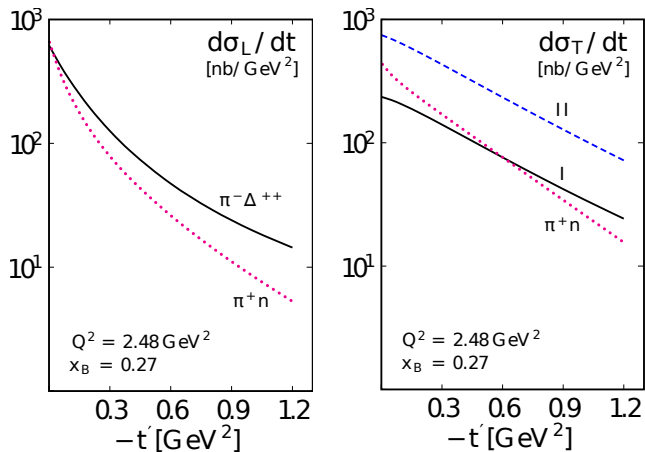


**Fig. 11** The longitudinal (left) and the transverse (right) cross sections of  $\gamma^*p \rightarrow \pi^- \Delta^{++}$  versus  $-t' = -t + t_0$ . The solid (dashed) lines represent the predictions obtained for scenario I (II). For comparison, the dotted lines are the results for  $\gamma^*p \rightarrow \pi^+ n$  obtained with the same GPDs. The figure is taken from Ref. [26].

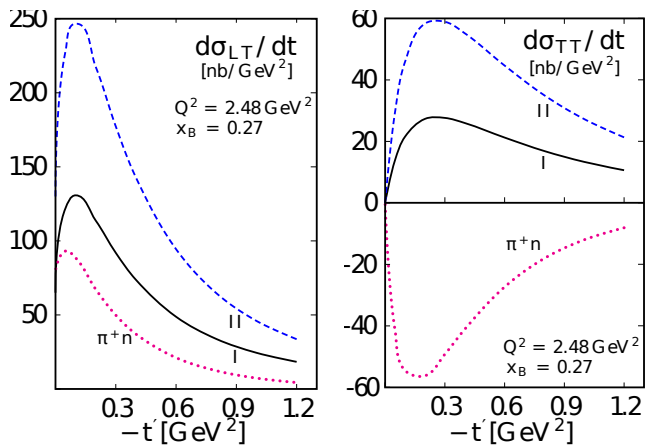


**Fig. 12** The longitudinal-transverse (left) and the transverse-transverse (right) interference cross sections of  $\gamma^*p \rightarrow \pi^- \Delta^{++}$ . For other notations see Fig. 11. The figure is taken from Ref. [26].

ones. It is to be stressed that the predictions are to be understood as rough estimates, their uncertainties are very large.

In [26] also the asymmetry  $A_{LL}$  has been calculated, which can be measured with longitudinally polarized beam and target and is to be integrated upon the electroproduction cross section

$$A_{LL} = \sqrt{1 - \varepsilon^2} \frac{1}{2\sigma_0} \sum_{\lambda_R} \left[ |\mathcal{M}_{0\lambda_R,++}|^2 - |\mathcal{M}_{0\lambda_R,-+}|^2 \right] \quad (73)$$

where

$$\sigma_0 = \sum_{\lambda_R} \left[ |\mathcal{M}_{0\lambda_R,++}|^2 + |\mathcal{M}_{0\lambda_R,-+}|^2 + \varepsilon |\mathcal{M}_{0\lambda_R,0+}|^2 \right].$$

(74)

The magnitude of the predictions are close to that one for the  $\pi^+ n$  channel but the two scenarios lead to opposite signs of  $A_{LL}$ . This result is understandable: for scenario I the amplitudes  $\mathcal{M}_{0\lambda_R,++}$  are large, whereas for scenario II the amplitudes  $\mathcal{M}_{0\lambda_R,-+}$  dominate. This feature provides an opportunity to discriminate between dominant  $G_{T5}$  and  $G_{T7}$ .

There are many other asymmetries, like the beam-spin one

$$A_{LU}^{\sin(\phi)} \sim \frac{1}{\sigma_0} \sum_{\lambda_R} \text{Im} \left[ (\mathcal{M}_{0\lambda_R,++} - \mathcal{M}_{0\lambda_R,-+})^* \mathcal{M}_{0\lambda_R,0+} \right]. \quad (75)$$

Most of these asymmetries depend on relative phases between different helicity amplitudes. At present, it is not possible to estimate these asymmetries reliably.

For vector-meson channels, as for instance  $\rho^0 \Delta^+$ , the same  $A^A$ s hold. Only a plus sign appears between the  $A^A$ s in Eq. (63) instead of the minus sign. This projects out the parity-even GPDs  $G_i$  (1).

### 6.3 Near-threshold pion production

Pion photo- and electroproduction on the nucleon  $\gamma N \rightarrow \pi N$ ,  $\gamma^* N \rightarrow \pi N$  close to threshold has been studied extensively since the 1950s both experimentally and theoretically. The celebrated low-energy theorems (LET) [155–157] relate the S-wave transverse  $E_{0+}$  and longitudinal  $L_{0+}$  multipoles at threshold to the nucleon electromagnetic and axial form factors in the chiral limit  $m_\pi = 0$ . The new insight gained from CHPT calculations [158, 159] is that the expansion at small  $Q^2$  has to be done with care as the limits  $m_\pi \rightarrow 0$  and  $Q^2 \rightarrow 0$  do not commute, in general. For large momentum transfers, the power counting of CHPT cannot be applied. However, the traditional derivation of LET using PCAC and current algebra is not affected as long as the emitted pion is “soft” with respect to the initial and final state nucleons simultaneously. The corresponding condition is, parametrically,  $Q^2 \ll \Lambda^3/m_\pi$  [32, 160] where  $\Lambda$  is some hadronic scale, and might be violated at the highest  $Q^2$  available in future experiments at JLab and EIC.

Such an interplay of chiral dynamics with “hard” QCD factorization picture of large- $Q^2$  reactions is potentially very interesting since the generalized pion-nucleon LCDAs in the chiral limit can be expressed in terms of the “chirally-rotated” nucleon LCDAs [32, 161],

thus providing one with an additional handle to separate the different components in the nucleon wave function. In addition, if the structure of the corrections beyond LET can be quantified, pion electroproduction would allow one to determine the nucleon axial form factor at large momentum transfers, which is difficult to access by direct measurements.

The difficulty is that the onset of the pQCD regime in the form factors is generally believed to be postponed to very large momentum transfers, and at intermediate  $Q^2 \sim 1 - 10 \text{ GeV}^2$  one has to take into account non-factorizable “soft” or “end-point” contributions. The light-cone sum rule (LCSR) technique [112] allows one to estimate such contributions in terms of the same nucleon LCDAs that enter pQCD calculation using dispersion relations and duality. It can be generalized and was applied to the pion electroproduction at threshold in Ref. [119]. The LCSR calculation (so far available in leading order only) suggests that the leading transverse  $E_{0+}$  multipole receives moderate corrections w.r.t. the LET predictions in the whole studied  $Q^2$  range, whereas the longitudinal  $L_{0+}$  multipole receives large corrections and tends to change sign at large  $Q^2$ . These conclusions are, qualitatively, in agreement with the existing CLAS measurements for charged [162] and neutral [163] pion production. More studies, both theoretical and experimental, are needed to make this comparison fully quantitative.

## 7 First experimental results from JLab 12 GeV

Except for the information obtained from the relation to the transition form factors and the relation to the ordinary GPDs in the large  $N_c$  limit, little is known about the transition GPDs so far. On the experimental side, recently, the first beam spin asymmetries for hard exclusive  $\pi^- \Delta^{++}$  electro-production were published by the CLAS collaboration at JLab and further measurements on  $N \rightarrow \Delta^+$  DVCS with CLAS and  $\pi^+ \Delta^0$  DVMP based on data from hall C at JLab are ongoing. This section will summarize the published and ongoing studies and their impact on constraining transition GPDs.

### 7.1 $\pi^- \Delta^{++}$ electroproduction with CLAS12

The first observable sensitive to  $N \rightarrow \Delta$  transversity transition GPDs and  $N \rightarrow \Delta$  transition GPDs in general was provided by the CLAS collaboration with hard exclusive ( $\gamma^* N \rightarrow \pi^- \Delta^{++} \rightarrow \pi^- [p\pi^+]$ ) electro-production beam-spin asymmetries, based on the scattering of longitudinally polarized 10.6 GeV electrons on

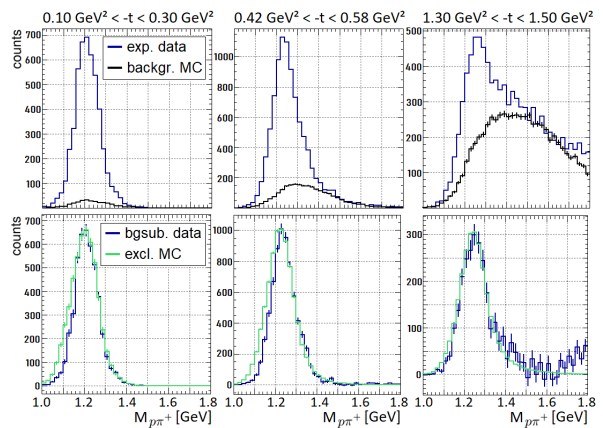


**Fig. 13** Upper row:  $\Delta^{++}$  peak in the  $p\pi^+$  invariant mass of the experimental data (blue, solid) in comparison to the non-resonant background obtained with the semi-inclusive deep inelastic scattering MC (black) for selected bins of  $-t$  in the forward region ( $Q^2 = 2.48 \text{ GeV}^2$ ,  $x_B = 0.27$ ) after a cut on  $M_{\pi^+\pi^-} > 1.1 \text{ GeV}$ . Lower row:  $\Delta^{++}$  peak in the same bins after the subtraction of the background (blue, solid) in comparison to the result from the exclusive MC (green). Figure in modified form taken from Ref. [25].

an unpolarized hydrogen target in the CLAS12 detector [8], published in 2023 [25].

For the study, the  $ep\pi^- X$  final state was detected, and the  $\pi^+$  was reconstructed via a cut on the missing mass. Kinematic cuts on  $W > 2 \text{ GeV}$ ,  $Q^2 > 1.5 \text{ GeV}^2$ ,  $y < 0.75$ , and  $-t < 1.5 \text{ GeV}^2$  have been applied. Furthermore, a cut on  $M(\pi^+\pi^-) > 1.1 \text{ GeV}$  is applied to reject the dominant background from  $\gamma^* p \rightarrow p \rho^0 \rightarrow p \pi^+ \pi^-$ . Fig. 13 shows the  $\Delta^{++}$  peak in the resonance spectrum of the  $p\pi^+$  invariant mass and compares it to the background distribution from a full semi-inclusive deep inelastic scattering Monte Carlo simulation. In addition, the background-subtracted data is compared to a Monte Carlo simulation of the exclusive process. It can be observed that the background contribution increases with increasing values of  $-t$ . However, the good agreement of the falling tail of the  $\Delta^{++}$  peak after the background subtraction with the exclusive Monte Carlo shows that the background is well understood and under control. To select the  $\pi^- \Delta^{++}$  signal region, a cut on  $M(p\pi^+) < 1.3 \text{ GeV}$  is applied. For these events, the beam spin asymmetries are determined for 3  $Q^2 - x_B$  bins and several  $-t$  and  $\phi$  bins. For each  $-t$  bin, the structure function ratio  $\sigma_{LT'}/\sigma_0$  is extracted based on a fit of the  $\phi$  dependence of the beam spin asymmetry, and a background subtraction is performed for each kinematic bin. More details on the analysis can be found in Ref. [25].

Fig. 14, shows a comparison of the obtained structure function ratio  $\sigma_{LT'}/\sigma_0$  for  $\pi^- \Delta^{++}$  with results from  $\pi^+ n$  [164] and  $\pi^0 p$  [165]. The figure shows that

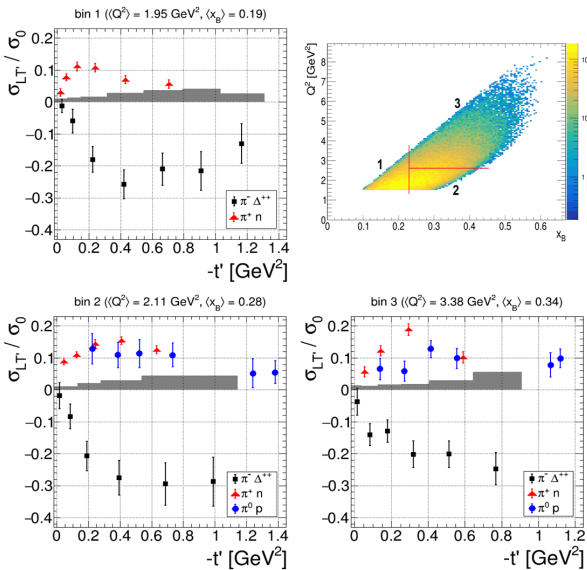


**Fig. 14**  $\sigma_{LT'}/\sigma_0$  and its statistical uncertainty for  $\pi^- \Delta^{++}$  (black squares, Ref. [25]) as a function of  $-t' = (|t| - |t_{min}|)$  and its systematic uncertainty (gray band), measured with CLAS12. For comparison, the CLAS12 results from the hard exclusive  $\pi^+ n$  (red triangles, Ref. [164]) and  $\pi^0 p$  (blue circles, Ref. [165]) electroproduction with similar kinematics are shown. The sub-figures correspond to the results for the different  $Q^2$  and  $x_B$  bins defined in the upper right insert. The mean kinematics are shown on top of each sub-figure. Figures in modified form taken from Ref. [25].

the structure function ratio of  $\pi^- \Delta^{++}$  shows an opposite sign than for  $\pi^+ n$  and an approximately doubled magnitude compared to  $\pi^+ n$ . The different sign of the asymmetry can be related to an interaction of the virtual photon with different quarks ( $u$ ,  $d$ ) for the two reactions and the opposite sign of the quark polarization. However, the large absolute magnitude of  $\sigma_{LT'}/\sigma_0$  for  $\pi^- \Delta^{++}$ , compared to  $\pi^+ n$  can be seen as a clear effect of the excitation process, which is encoded in the transition GPDs [25].

The studied polarized structure function  $\sigma_{LT'}$  is given by products of convolutions of transversity and helicity non-flip transition GPDs with sub-process amplitudes and shows the following relation to the two dominant transversity transition GPDs [25]:

$$\sigma_{LT'} \sim \sqrt{-t'} \operatorname{Im} [G_{T_5}^3 \cdot A + c G_{T_7}^3 \cdot A'], \quad (76)$$

with an unknown kinematic factor  $c$  and helicity amplitudes for longitudinally polarized virtual photons  $A$  and  $A'$ , which are determined by the helicity non-flip transition GPDs  $\tilde{G}_3$  and  $\tilde{G}_4$  within the large  $N_c$  limit. The transversity transition GPDs  $G_{T_5}^3$  and  $G_{T_7}^3$  can be related to the ground state transversity GPD  $H_T$  in the large  $N_c$  limit, as shown in Eq. 68. Therefore, they are expected to be sensitive to the tensor charge of the resonance following Eq. 45.

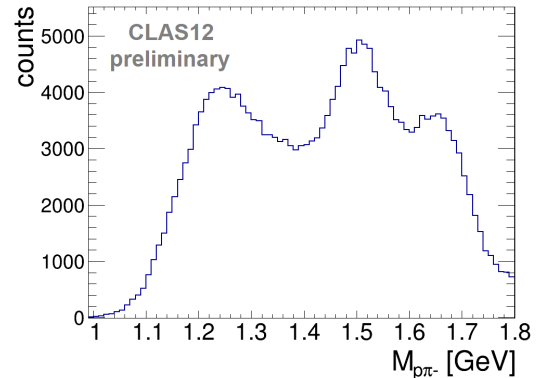


**Fig. 15**  $p\pi^-$  invariant mass for the  $e'\pi^+\Delta^0 \rightarrow e'\pi^+p\pi^-$  DVMP process for  $-t < 1 \text{ GeV}^2$ , after a cut on  $M(\pi^+\pi^-) > 1.1 \text{ GeV}$  to reject the exclusive  $\rho$  events, measured with CLAS12.

Based on CLAS12 data with a longitudinally polarized  $NH_3$  target, it is planned to extend the study to target polarization observables like  $A_{UL}$  and  $A_{LL}$ . Furthermore, the extraction of absolute cross sections ( $\sigma_0 = \sigma_L + \sigma_T$ ) and the  $\cos(\phi)$  ( $\sigma_{LT}$ ) and  $\cos(2\phi)$  ( $\sigma_{TT}$ ) modulations of the cross section is planned based on data from an unpolarized proton target.

## 7.2 Further $N \rightarrow N^*$ DVMP channels with CLAS12

As shown in section 6.2, different  $N \rightarrow N^*$  DVMP channels can be used to study transition GPDs, and a combination of data from different mesons in the final state will allow a flavor decomposition of the transition GPDs.

Currently, the feasibility of the study of different channels, like

- $ep \rightarrow e'\pi^+\Delta^0 \rightarrow e'\pi^+p\pi^-$ ,
- $ep \rightarrow e'\pi^+\Delta^0 \rightarrow e'\pi^+n\pi^0$ ,
- $ep \rightarrow e'\pi^0\Delta^+ \rightarrow e'\pi^0n\pi^+$ ,

is under investigation. Since the electromagnetic calorimeter of CLAS12 is limited to a polar angle below  $35^\circ$ , only resonance decays with a charged pion can be efficiently detected. However, if the DVMP meson is a charged pion, the resolution of CLAS12 is sufficient to consider the application of the missing mass technique to reconstruct the pion from the resonance decay.

As an example, Fig. 15 shows the  $p\pi^-$  invariant mass for the  $e'\pi^+\Delta^0 \rightarrow e'\pi^+p\pi^-$  DVMP process. It can be clearly seen that, in contrast to the  $\pi^- [p\pi^+]$  final state, which was discussed in the last section and which can only be populated by  $\Delta$  resonances, the  $\pi^+ [p\pi^-]$  final state shows the complete resonance spectrum with nucleon and  $\Delta$  resonances. Besides the  $\Delta(1232)$  peak, the second and third resonance regions are clearly visible in Fig. 15. All other  $N \rightarrow N^*$  DVMP channels show



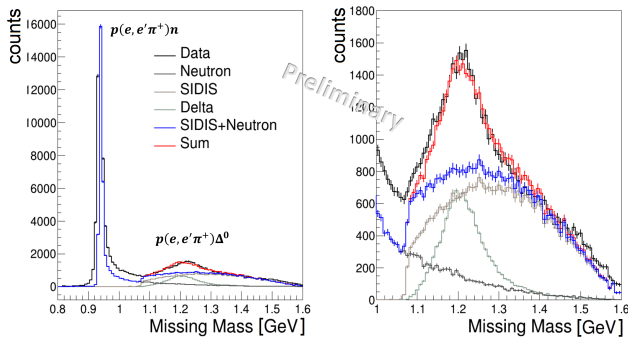


**Fig. 16** Missing mass distribution for exclusive pion electroproduction reaction from Kaon-LT data ( $Q^2 = 2.1 \text{ GeV}^2$ ,  $W = 2.95 \text{ GeV}$ ) from JLab hall C. All the curves except the data are from Monte Carlo simulations. The fits of the simulations to the data are preliminary.

a similar picture. Therefore, a clean separation of the  $\Delta(1232)$  events is more difficult for these channels, and either a full fit of the spectrum, including non-resonant background, or a partial wave decomposition have to be performed to access the  $\Delta(1232)$  events, and especially the higher resonances with a higher mass.

### 7.3 $\pi^+ \Delta^0$ electroproduction in JLab Hall C

Hall C at JLab [166] is a unique facility that gives access to high precision DVMP reaction measurements over a wide range of kinematics. The hall has a fixed target geometry with two focusing magnetic spectrometers, which detect the scattered electron and final state meson in coincidence. The final state hadron is reconstructed to high resolution through missing mass. Hall C is also the only facility worldwide with the capability to perform high  $Q^2$  Longitudinal/Transverse (L/T) separations of the reaction cross section via the Rosenbluth separation process. This is done by taking data at two values of  $\epsilon$  (virtual photon polarization factor) for each kinematic point, where

$$\epsilon = 1 + 2 \frac{(E_e - E_{e'})^2 + Q^2}{Q^2} \tan^2 \frac{\theta_{e'}}{2} \quad (77)$$

The Kaon-LT experiment (E12-09-011) [167] is the first L/T separation experiment after the 12 GeV upgrade to study exclusive  $K^+$  electroproduction reaction  $p(e, e' K^+) \Lambda$ . The experiment also gathered high-statistics exclusive  $\pi^+$  electroproduction data, as it is one of the background processes for the exclusive  $K^+$  channel. The exclusive  $\pi^+$  data include both the  $p(e, e' \pi^+) n$  and  $p(e, e' \pi^+) \Delta^0$  reactions. Table 3 lists all settings collected to date during the Kaon-LT experiment. The BSA analysis is ongoing for the 10.6 GeV

$E_b$ (GeV)	$Q^2$ ( $\text{GeV}^2/c^2$ )	$W$ (GeV)	$\epsilon_{high}/\epsilon_{low}$
10.591/8.213	5.5	3.02	0.53/0.18
10.591/8.213	4.4	2.74	0.72/0.48
10.591/8.213	3.0	3.14	0.67/0.39
10.591/6.187	3.0	2.32	0.88/0.57
10.590/6.187	2.115	2.95	0.79/0.25
4.930/3.834	0.5	2.40	0.70/0.45

**Table 3** The kinematics settings acquired to date in the KaonLT experiment [167].

kinematic settings listed. In this experiment, the meson spectrometer is rotated 3 degrees on either side of the  $\vec{q}$ -vector to get full  $\phi$  coverage at fixed  $t$ , needed for the BSA measurement.

The Hall C spectrometers give access to very good missing mass resolution. Figure 16 shows the missing mass distribution for  $p(e, e' \pi^+) X$  including experimental data and different simulated processes. The plot on the left gives the full range of missing mass, which clearly shows a clean  $p(e, e' \pi^+) n$  peak. The figure on the right is a zoomed-in version to focus on the  $\Delta^0$  region. The  $p(e, e' \pi^+) n$  sample has very little background underneath; therefore, it can be selected by using a missing mass cut around the peak. On the other hand, the  $p(e, e' \pi^+) \Delta^0$  reaction has a Breit-Wigner distribution that sits atop other multi-pion processes. This requires a background shape study to cleanly isolate the  $p(e, e' \pi^+) \Delta^0$  reaction. A shape study was performed for each  $\phi$  bin for each beam helicity state by fitting the  $\Delta^0$  Monte Carlo to the background-subtracted experimental data, and the BSA was calculated. Figure 17 shows preliminary  $p(e, e' \pi^+) \Delta^0$  BSA results for one kinematic setting. A parallel analysis of  $p(e, e' \pi^+) n$  BSA is also in progress for the same kinematics. The  $\Delta^0$  BSA paper will include the  $\sigma_{LT'}$  ratio for both  $n$  and  $\Delta^0$  final states.

The future plan is to perform an L/T separation for all kinematics listed in Table 3 for both  $p(e, e' \pi^+) \Delta^0$ ,  $p(e, e' \pi^+) n$  reactions. This involves a more detailed understanding of all the experimental systematics, as well as fine-tuning the simulation models. The L/T separated cross-section ratio for  $p(e, e' \pi^+) \Delta^0$  and  $p(e, e' \pi^+) n$  can give access to  $N \rightarrow \Delta^0$  transition GPDs. The KaonLT experiment is anticipated to collect more data to complete the proposed kinematics. There is also the possibility of increasing the kinematic coverage with a future experiment using the Hall C experimental setup. An energy upgrade at Jefferson Lab will allow a further increase in kinematic coverage for the  $p(e, e' \pi^+) \Delta^0$  L/T separation experiment.

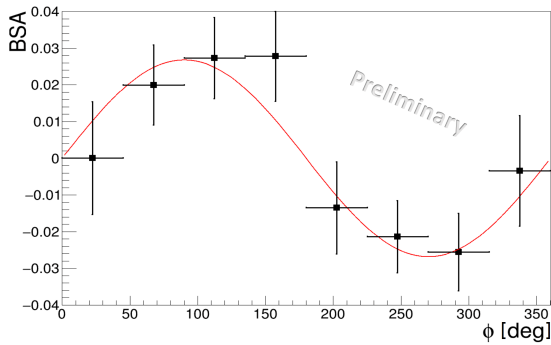


**Fig. 17** Preliminary Beam Spin Asymmetry results for the  $p(e, e' \pi^+) \Delta^0$  reaction from the KaonLT experiment ( $Q^2 = 2.1$  GeV<sup>2</sup>,  $W = 2.95$  GeV) in JLab hall C. Only statistical errors are shown. The final results will include three  $\times$  more data after including all three meson spectrometer settings.

#### 7.4 $N \rightarrow \Delta^+$ DVCS with CLAS12

First feasibility studies for the non-diagonal DVCS process with limited statistics and kinematic coverage, not allowing a real background separation, have been performed based on CLAS data from the 6 GeV era in 2009 [168]. Studies of associated electroproduction of real photons,  $e + p \rightarrow e' \gamma \pi N$ , in the  $\Delta(1232)$ -resonance region were also performed with HERMES [24], but similarly to the first CLAS studies, they also suffered from limited statistics and a missing background separation. The 12 GeV upgrade of JLab finally allowed initial measurements of the  $N \rightarrow N^*$  DVCS and DVMP processes at reasonably high  $Q^2$  values and with sufficient statistics for the first time. For this process, the detection of all final state particles is important for a proper rejection of potential backgrounds. For  $\gamma^* p \rightarrow \gamma \pi^+ n$   $N \rightarrow N^*$  DVCS, two final states are possible based on the  $N^{*+}$  decay:

1.  $\gamma^* p \rightarrow \gamma N^{*+} \rightarrow \gamma n \pi^+$
2.  $\gamma^* p \rightarrow \gamma N^{*+} \rightarrow \gamma p \pi^0$

With a deuterium (neutron) target, also the following reactions can be studied:

1.  $\gamma^* n \rightarrow \gamma N^{*0} \rightarrow \gamma p \pi^-$
2.  $\gamma^* n \rightarrow \gamma N^{*0} \rightarrow \gamma n \pi^0$

In all cases, the  $N^*$  can be a nucleon or a  $\Delta$  resonance. For the very forward regime of the DVCS photon (low  $-t$ ), the  $N^*$  and its decay products are expected to be detected under central to backward lab angles. Therefore, the detection capabilities of neutral pions, originating from a resonance decay, are very limited with CLAS12 due to the missing electromagnetic calorimeter in the region of  $\theta > 35^\circ$ , leading to a limitation of the studies to the  $\gamma n \pi^+$  final state for a proton target and to the  $\gamma p \pi^-$  final state for a neutron target.

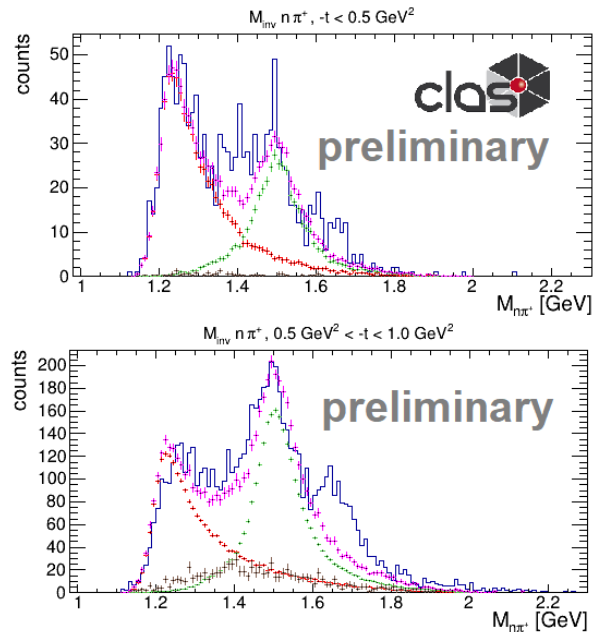


**Fig. 18** Preliminary measured resonance spectrum in the  $n\pi^+$  invariant mass of the  $e p \rightarrow e' \gamma n \pi^+$  process from CLAS12 (blue). The kinematic and selection cuts described in the text are applied, and the  $-t$  range is stated on top of the sub-figures. For comparison, MC simulations for the  $N \rightarrow N^*$  DVCS process with the production of a  $\Delta(1232)$  resonance (red) and for the production of the resonances in the second resonance region (green), following the model prediction in Fig. 9, as well as MC simulations for the non-resonant contributions (brown), are shown. The magenta histogram provides the sum of all MC contributions.

Based on data taken with a 10.2 GeV and a 10.6 GeV longitudinally polarized electron beam and a hydrogen target, a first study has been performed with CLAS12. A series of exclusivity cuts on the missing mass, missing energy, missing transverse momentum, and missing cone angle are applied to select exclusive events. In addition, kinematic cuts on  $W > 2$  GeV,  $Q^2 > 1.5$  GeV<sup>2</sup>,  $y < 0.8$  and  $E_{\gamma-DVCS} > 2$  GeV have been applied for the preliminary study. Furthermore, a cut on  $M(\pi^+ \gamma) > 1$  GeV is applied to reduce the dominant background from exclusive  $\rho^+$  production ( $\gamma^* p \rightarrow \rho^+ n$ ), with the  $\rho^+$  decaying into  $\pi^0 \pi^+$ , with one undetected photon, and the much less frequent decay into  $\gamma \pi^+$ .

Figure 18 shows the resonance spectrum of the  $n\pi^+$  invariant mass after the listed kinematic cuts for two bins of  $-t$ , measured with CLAS12. A clear peak from the delta resonance as well as from the second resonance region can be observed in both ranges of  $-t$ , while for the higher  $-t$  bins, also the third resonance region exceeds the production threshold and becomes visible.

Figure 19 shows a preliminary extraction of the  $A_{LU}^{\sin \phi}$  moment of the BSA as a function of the resonance mass in different bins of  $-t$  and as a function

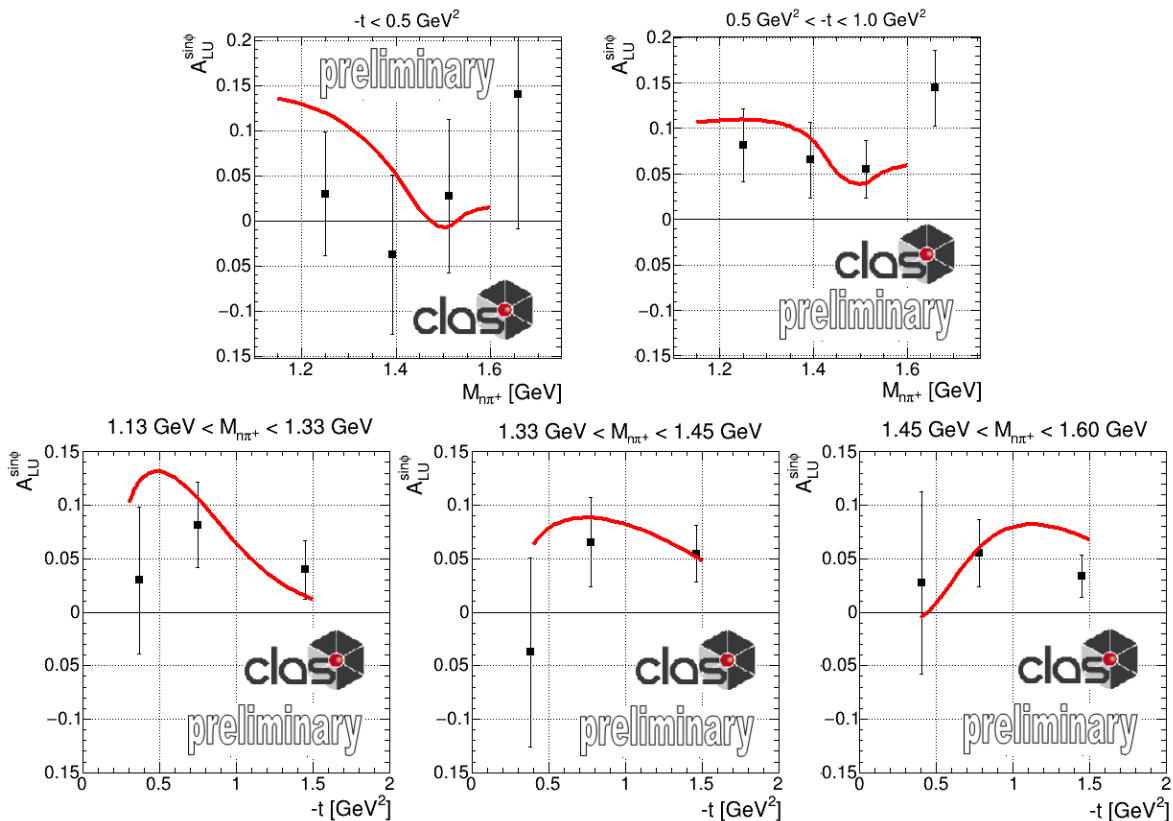


**Fig. 19** Preliminary results of the  $A_{LU}^{\sin\phi}$  moment of the beam-spin asymmetry from the  $e p \rightarrow e' \gamma n \pi^+$  process, with the cuts described in the text, as a function of the resonance mass  $M_{n\pi^+}$  in two bins of  $-t$ , as stated above the figures (upper row), and as a function of  $-t$  in the region around the  $\Delta(1232)$  resonance ( $1.13 \text{ GeV} < M_{n\pi^+} < 1.33 \text{ GeV}$ , lower row left), the Roper resonance ( $1.33 \text{ GeV} < M_{n\pi^+} < 1.45 \text{ GeV}$ , lower row center) and the second resonance region ( $1.45 \text{ GeV} < M_{n\pi^+} < 1.60 \text{ GeV}$ , lower row right). Backgrounds from the  $e p \rightarrow e' \pi^0 N^* \rightarrow e' \pi^0 n \pi^+$  process, with one photon from the  $\pi^0$  decay misidentified as the DVCS photon are not subtracted yet. The red line shows the prediction for the  $N \rightarrow N^*$  DVCS process from the transition GPD based model described in section 6.1, integrated over the CLAS12 kinematic distributions.

of  $-t$  in different regions of the resonance mass  $M_{n\pi^+}$ , in comparison to the transition GPD-based theoretical predictions described in section 6.1.

The study is currently ongoing, and further backgrounds like the  $N \rightarrow N^* \pi^0$  DVMP process, with one photon from the  $\pi^0$  decay misidentified as the DVCS photon, need to be considered and subtracted. The contamination from  $N \rightarrow N^* \pi^0$  DVMP was found to be in the overall order of  $\approx 30\%$  for the shown data sample and shows an asymmetry with the same sign but a smaller magnitude than the  $N \rightarrow N^*$  DVCS process. A subtraction is therefore expected to lead to a slight increase of the measured  $A_{LU}^{\sin\phi}$  moments. Considering these uncertainties, the preliminary results for distributions and beam spin asymmetries show a promising agreement with the transition GPD based theory predictions described in section 6.1 and shown in Fig. 19.

Similar to the  $N \rightarrow N^*$  DVMP processes described in sections 7.1 and 7.2, also for the  $N \rightarrow N^*$  DVCS processes, studies with a deuterium target, with fur-

ther target polarizations as well as the extraction of the unpolarized cross-section terms are possible based on CLAS12 data.

## 8 Transition processes: hadron scattering

### 8.1 Meson-induced exclusive Drell-Yan process

Besides the discussed exclusive lepton scattering reactions, the exclusive hard reactions with the hadron beam are expected to be sensitive to the GPDs. The most promising reaction is the meson-induced exclusive Drell-Yan process [50, 51], which can be studied at J-PARC or CERN COMPASS/AMBER with the pion and kaon beams. In addition, the primary proton beam at J-PARC could be used for the GPDs [52]. These processes are described in detail below.

Recently, JLab CLAS reported the first measurement of timelike Compton Scattering (TCS) process [169]. The comparison of the measured polarization

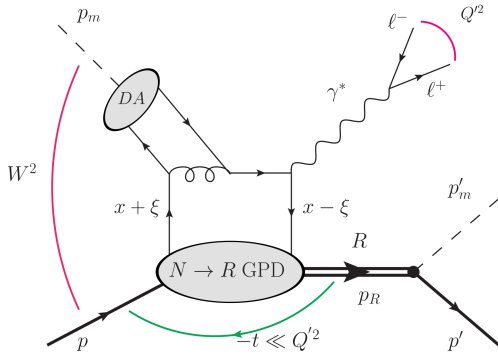


**Fig. 20** Schematic drawing of the exclusive Drell-Yan process. For a ground-state nucleon in the final state, the process is sensitive to the ordinary GPDs, while a baryon resonance in the final state provides sensitivity to the transition GPDs.

asymmetry of TCS with model predictions suggests the universality of GPDs in both spacelike and timelike processes. In the same analogy between TCS and DVCS processes, the meson-induced exclusive process is the complementary timelike process to access the nucleon GPDs, with respect to the DVMP process.

The exclusive meson-induced Drell-Yan process  $mN \rightarrow \ell^+ \ell^- B$ , as shown in Fig. 20, describes the interaction of a meson beam ( $m$ ) with a nucleon target ( $N$ ) during which a lepton pair ( $\ell^\pm$ ) and a ground state nucleon or a baryon resonance ( $B$ ) are produced. The process is expected to factorize if the momentum transfer squared  $t$  between the initial and final state baryon is small and the four momentum squared  $Q^2$  of the final state virtual photon is large. However, potential large contributions of non-factorized processes still need to be evaluated in more detail and considered for the analysis and interpretation of the measurements, as shown in Refs. [170].

The exclusive Drell-Yan process  $\pi(p_m)N(p) \rightarrow \gamma^*(q')N(p') (\rightarrow \ell^+ \ell^- N)$  is described by the following variables: the virtual-photon momentum squared  $Q^2 = q'^2$ , the invariant momentum transfer  $t = (p' - p)^2$ , the scaling variable  $\tau$  given by

$$\tau = \frac{Q^2}{2p \cdot p_m} \simeq \frac{Q^2}{s - M_N^2} \simeq \frac{Q^2}{s}, \quad (78)$$

where  $s = (p + p_m)^2$  and  $M_N$  is the nucleon mass. The variable  $\tau$  is similar to the Bjorken variable in the DVCS and DVMP, and it is related to the pion momentum as  $q \simeq s/(2M_N) \simeq Q^2/(2M_N\tau)$ . The skewness variable  $\xi$  is approximately given by  $\tau$  as

$$\xi \simeq \frac{Q^2}{2s - Q^2} = \frac{\tau}{2 - \tau}. \quad (79)$$

Using these kinematical variables, we write the  $\pi^- N \rightarrow \ell^+ \ell^- N$  cross section up to twist-4 terms as

[152, 171]

$$\begin{aligned} \frac{d\sigma}{dt dQ^2 d\cos\theta d\phi} = & \frac{3}{8\pi} \left( \sin^2\theta \frac{d\sigma_L}{dt dQ^2} + \frac{1 + \cos^2\theta}{2} \frac{d\sigma_T}{dt dQ^2} \right. \\ & \left. + \frac{\sin 2\theta \cos\phi}{\sqrt{2}} \frac{d\sigma_{LT}}{dt dQ^2} + \sin^2\theta \cos 2\phi \frac{d\sigma_{TT}}{dt dQ^2} \right), \end{aligned} \quad (80)$$

where the  $\theta$  and  $\phi$  are polar and azimuthal angles of a lepton direction in the final state. The cross section  $d\sigma_L$  ( $d\sigma_T$ ) is for the longitudinally (transversely)-polarized virtual photon. The  $d\sigma_{LT}$  and  $d\sigma_{TT}$  are the longitudinal-transverse interference and transverse (helicity  $h = 1$ )-transverse ( $h = -1$ ) interference terms. The cross section  $d\sigma_L$  is leading twist,  $d\sigma_{LT}$  is twist three, and  $d\sigma_T$  and  $d\sigma_{TT}$  are twist-four terms.

For the reaction  $\pi^- N \rightarrow \ell^+ \ell^- N$ , Refs. [50, 51] show that the longitudinal part of the cross section  $\sigma_L$  can be related to the GPDs  $\tilde{H}$  and  $\tilde{E}$ . The transverse part of the cross sections  $\sigma_T$  and the  $LT$  and  $TT$  interference terms  $\sigma_{LT}$  and  $\sigma_{TT}$  are also sensitive to transversity GPDs as shown in Ref. [171]. For reactions with a baryon resonance in the final state, this can be related to the corresponding transition GPDs. However, a formalism is not available at the present stage.

In this process, the relevant amplitude is expressed as the convolution of the short-distance partonic annihilation processes with the two parts of long-distance nature, associated with the nucleon GPD and the pion DA. Here, the GPDs for the nucleon are the functions of the light-cone momentum fractions  $x$  of the average momentum, the skewness  $\xi \equiv (p - p')^+ / (p + p')^+$ , and the momentum transfer squared  $t = \Delta^2$  with  $\Delta \equiv p' - p$  where the  $p$  and  $p'$  are initial and final nucleon momenta, respectively.

The quark GPDs relevant to the processes without the quark-helicity flip are given by (see, *e.g.*, [17, 18])

$$\begin{aligned} & \int \frac{dz^-}{4\pi} e^{ixP^+ z^-} \langle p' | \bar{q}(-z/2) \gamma^+ q(z/2) | p \rangle \Big|_{z^+ = \bar{z}_1 = 0} \\ & = \frac{1}{2P^+} \bar{u}(p') \left[ H^q(x, \xi, t) \gamma^+ + E^q(x, \xi, t) \frac{i\sigma^{+\alpha} \Delta_\alpha}{2M_N} \right] u(p), \end{aligned} \quad (81)$$

and

$$\begin{aligned} & \int \frac{dz^-}{4\pi} e^{ixP^+ z^-} \langle p' | \bar{q}(-z/2) \gamma^+ \gamma_5 q(z/2) | p \rangle \Big|_{z^+ = \bar{z}_1 = 0} \\ & = \frac{1}{2P^+} \bar{u}(p') \left[ \tilde{H}^q(x, \xi, t) \gamma^+ \gamma_5 + \tilde{E}^q(x, \xi, t) \frac{\gamma_5 \Delta^+}{2M_N} \right] u(p), \end{aligned} \quad (82)$$

for each quark flavor  $q$ , where  $|p\rangle$  denotes the proton state with momentum  $p$  and mass  $M_N$ ,  $u(p)$  denotes the Dirac spinor for the proton,  $\sigma^{\alpha\beta}$  is given by  $\sigma^{\alpha\beta} =$

$(i/2)[\gamma^\alpha, \gamma^\beta]$ , and the average momentum is denoted as  $P (\equiv (p+p')/2)$ . The  $H^q(x, \xi, t)$  and  $E^q(x, \xi, t)$  are the unpolarized quark GPDs, and  $\tilde{H}^q(x, \xi, t)$  and  $\tilde{E}^q(x, \xi, t)$  are the polarized ones.

The factorization has been proven for the DVMP processes at the leading twist, including the exclusive electroproduction of pion,  $\gamma^* N \rightarrow \pi N$  [55]. The amplitude can be written in terms of the hard-scattering processes at the parton level, combined with the pion distribution amplitude (DA),  $\phi_\pi$ , and also the nucleon GPDs,  $\tilde{H}$  and  $\tilde{E}$ . By interchanging the initial  $\gamma^*$  and final  $\pi$  in the exclusive electroproduction of pion, and replacing the spacelike momentum of  $\gamma^*$  by the time-like momentum, the factorization at twist-two is argued to be applicable to the exclusive Drell-Yan process,  $\pi(q)N(p) \rightarrow \gamma^*(q')N(p')$ , with the same universal non-perturbative input [50].

The appropriate kinematical region is of large time-like virtuality  $Q'^2 = q'^2$  at fixed  $t = (p' - p)^2$  and fixed scaling variable  $\tau \equiv Q'^2/(2p \cdot q)$  where the  $q$ ,  $p$  and  $p'$  are the momenta of the pion, initial, and final nucleons, respectively. At the large  $Q'$  scaling limit, the corresponding leading-twist cross section of  $\pi^- p \rightarrow \gamma^* n$  as a function of  $t$  and  $Q'^2$  is expressed in terms of convolution integrals  $\tilde{\mathcal{H}}^{du}$  and  $\tilde{\mathcal{E}}^{du}$ , as follows [50]

$$\begin{aligned} \left. \frac{d\sigma_L}{dt dQ'^2} \right|_\tau &= \frac{4\pi\alpha_{\text{em}}^2}{27} \frac{\tau^2}{Q'^8} f_\pi^2 \left[ (1 - \xi^2) |\tilde{\mathcal{H}}^{du}(\tilde{x}, \xi, t)|^2 \right. \\ &\quad - 2\xi^2 \text{Re} (\tilde{\mathcal{H}}^{du}(\tilde{x}, \xi, t)^* \tilde{\mathcal{E}}^{du}(\tilde{x}, \xi, t)) \\ &\quad \left. - \xi^2 \frac{t}{4M_N^2} |\tilde{\mathcal{E}}^{du}(\tilde{x}, \xi, t)|^2 \right], \end{aligned} \quad (83)$$

where  $\alpha_{\text{em}}$  is the fine structure constant,  $f_\pi$  is the pion decay constant, and the variable  $\tilde{x}$  is

$$\tilde{x} = -\frac{(p_m + q')^2}{2(p + p') \cdot (p_m + q')} \simeq -\frac{Q'^2}{2s - Q'^2} = -\xi. \quad (84)$$

The convolution integral  $\tilde{\mathcal{H}}^{du}$  involves two soft objects: the nucleon GPD  $\tilde{H}^{du}$  for the  $p \rightarrow n$  transition and the twist-two pion DAs  $\phi_\pi$ . Using  $\tilde{H}^{du}(x, \xi, t) = \tilde{H}^u(x, \xi, t) - \tilde{H}^d(x, \xi, t)$  to relate the transition GPD with the usual proton GPDs  $\tilde{H}^q$  for quark flavor  $q = u, d$ , the expression of  $\tilde{\mathcal{H}}^{du}$  is given, at the leading order in  $\alpha_s$ , by [50]

$$\begin{aligned} \tilde{\mathcal{H}}^{du}(\tilde{x}, \xi, t) &= \frac{8}{3} \alpha_s \int_{-1}^1 dz \frac{\phi_\pi(z)}{1 - z^2} \\ &\quad \times \int_{-1}^1 dx \left( \frac{e_d}{\tilde{x} - x - i\epsilon} - \frac{e_u}{\tilde{x} + x - i\epsilon} \right) \\ &\quad (\tilde{H}^d(x, \xi, t) - \tilde{H}^u(x, \xi, t)), \end{aligned} \quad (85)$$

where  $e_{u,d}$  are the electric charges of  $u, d$  quarks in units of the elementary charge, and  $\alpha_s$  is the running coupling constant of QCD. The corresponding expression

of  $\tilde{\mathcal{E}}^{du}$  is given by (85) with  $\tilde{H}^q$  replaced by the proton GPDs  $\tilde{E}^q$ . Because of the pseudo-scalar nature of the pion, the cross sections (83) receive the contributions of  $\tilde{H}$  and  $\tilde{E}$  only, among the GPDs in Eqs. (81) and (82). The pion distribution function  $\phi_\pi(z)$  is defined in the region  $-1 < z < 1$  as  $\int_{-1}^1 dz \phi_\pi(z) = 1$ . Use of the same pion beam also provides an opportunity to access pion-to-nucleon transition distribution amplitudes [172] through investigation of backward charmonium production in pion-nucleon collisions  $\pi^- p \rightarrow J/\psi n$  [173].

To ensure proper factorization and sensitivity to the partonic structure,  $Q'$  has to be larger than 1 GeV and  $|t|$  is large enough. Both of these require a large center-of-mass energy ( $\sqrt{s}$ ) for the reactions. Nevertheless, the estimated hard exclusive Drell-Yan cross sections drop dramatically with an increase of  $\sqrt{s}$ . Furthermore, the experimental determination of exclusiveness for the measured reactions through a missing-mass technique favors the measurement of lepton tracks from the Drell-Yan process in an open apparatus, and thus the charged multiplicity has to be low enough for good tracking. Considering various experimental factors and constraints, it is found that carrying out the measurement of the exclusive Drell-Yan process in the coming high-momentum beamline at J-PARC with a 10-20 GeV  $\pi^-$  beam ( $\sqrt{s} = 4\text{-}6$  GeV) is unique and optimized.

The E50 experiment at J-PARC plans to investigate the charmed-baryon spectroscopy via the measurement of  $\pi^- + p \rightarrow Y_c^* + D^{*-}$  reaction in the high-momentum beam line [174, 175] with a spectrometer system of a large acceptance and good momentum resolutions. Thanks to the relatively low track density in the energy regime of J-PARC and the high-granularity tracking chambers of the E50 experiment, the measurement of the Drell-Yan process could be operated without the installation of a hadron absorber in front of the spectrometer. Without the multiple-scattering effect in the hadron absorber, a good momentum determination of muon tracks can be achieved so that the exclusive Drell-Yan process can be characterized via the missing-mass technique.

To identify the muon track, a muon identification ( $\mu$ ID) system after the spectrometer is necessary. The current design of the  $\mu$ ID system consists of hadron absorber layers made of 20-cm concrete and 230-cm iron to absorb incoming hadrons, a large-size tracker resistive plate chambers (RPC) upstream of the absorber (2.4x1.8 m<sup>2</sup> active area with a few mm spatial resolutions), and another RPC downstream of the absorber (3.5x2.5 m<sup>2</sup> active area with 5cm spatial resolution). The thickness of concrete and iron shall be optimized considering the stopping power for low-

momentum tracks and penetrating efficiency for high-momentum ones.

Using GK2013 GPDs [176] for the exclusive Drell-Yan process, a feasibility study for 50-day beam time was done in Ref. [51]. The simulated invariant mass  $M_{\mu^+\mu^-}$  and missing-mass  $M_X$  spectra of the  $\mu^+\mu^-$  events with  $M_{\mu^+\mu^-} > 1.5$  GeV and  $|t - t_0| < 0.5$  GeV<sup>2</sup> for  $P_\pi=10, 15,$  and  $20$  GeV are shown in Fig. 21, where  $t_0$  ( $= -4M_N^2\xi^2/(1-\xi^2)$ ) is the limiting value of  $t$  corresponding to the scattering angle in the center-of-mass system  $\theta^{CM} = 0$ . Lines with different colors denote the contributions from various sources: exclusive Drell-Yan (red, dashed), inclusive Drell-Yan (blue, dotted),  $J/\psi$  (cyan, dash-dotted), and random background (purple, solid), respectively. Signals of  $J/\psi$  are only visible in the invariant mass distributions for  $P_\pi=15$  and  $20$  GeV.

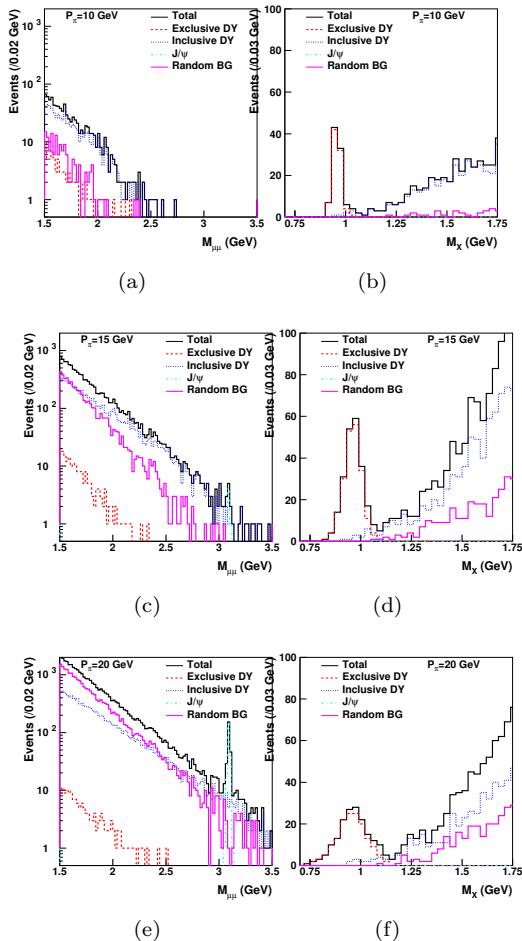


**Fig. 21** The Monte-Carlo simulated invariant mass  $M_{\mu^+\mu^-}$  and missing-mass  $M_X$  spectra of the  $\mu^+\mu^-$  events with  $M_{\mu^+\mu^-} > 1.5$  GeV and  $|t - t_0| < 0.5$  GeV<sup>2</sup> for  $P_\pi=10, 15,$  and  $20$  GeV. Lines with different colors denote the contributions from various sources. The GK2013 GPD parametrization was used as an input for the evaluation of the exclusive Drell-Yan process.

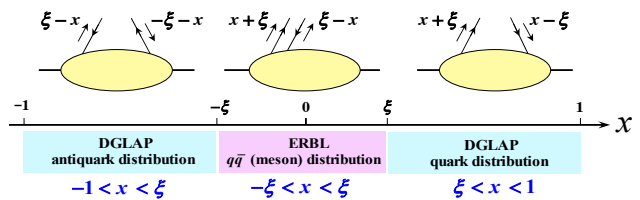


**Fig. 22** ERBL and DGLAP regions of the GPDs.

The study shows that the exclusive Drell-Yan events could be identified by the signature peak at the neutron mass ( $M_n \sim 0.940$  GeV) in the missing-mass spectrum for all three pion beam momenta, and the differential cross sections as a function of  $t$  are good enough to differentiate two different GPD parametrizations. In terms of statistics and missing mass resolution, it was found that the measurement with a 15-GeV pion beam would be optimal.

## 8.2 Proton-induced $2 \rightarrow 3$ processes

GPDs can also be investigated by using the primary proton beam through the  $2 \rightarrow 3$  process  $NN \rightarrow NMB$  [52], where  $M$  is a meson and  $B$  is a baryon. It is especially interesting that this process probes the kinematical region of the ERBL (Efremov-Radyushkin-Brodsky-Lepage) in the GPDs.

There are three kinematical regions for GPDs, depending on the values of the scaling variable  $x$  and the skewness variable  $\xi$  as shown in Fig. 22. The region  $\xi < x < 1$  ( $-1 < x < -\xi$ ) indicates a quark (antiquark) emission of momentum fraction  $x + \xi$  ( $\xi - x$ ) with a quark (antiquark) absorption of momentum fraction  $x - \xi$  ( $-\xi - x$ ), so that the process indicates a quark (antiquark) distribution amplitude. These are called DGLAP (Dokshitzer-Gribov-Lipatov-Altarelli-Parisi) regions. The region  $-\xi < x < \xi$  is the ERBL region, and the process is a quark emission of momentum fraction  $x + \xi$  with an antiquark emission of momentum fraction  $\xi - x$ , so that it is a quark-antiquark (meson) distribution amplitude.

The cross sections for  $NN \rightarrow N\pi B$  are estimated by using the pion- and rho-pole contributions to the GPDs in the ERBL region [52]. Here,  $B$  is a nucleon, or  $\Delta$ . We consider the process where the pion and the final nucleon have large and nearly opposite transverse momenta and a large invariant mass. Namely, the Mandelstam variables satisfy the hard condition  $s', |t'|, |u'| \gg m_N^2$  with  $t'/s' = \text{const}$ . Under such a kinematical condition, an intermediate exchange could be considered as a  $q\bar{q}$  state. The  $q\bar{q}$  attached to the nucleon is described by the GPDs in the ERBL region.

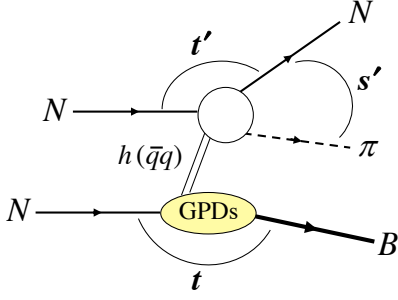


**Fig. 23** Factorized process for the  $NN \rightarrow N\pi B$  reaction under the kinematical condition  $s', |t'|, |u'| \gg M_N^2$  with  $t'/s' = \text{const.}$

The cross section  $NN \rightarrow N\pi B$  is described by the process in Fig. 23. The process is factorized into two terms, the GPD part and the scattering of the intermediate hadronic  $q\bar{q}$  state  $h$  with the nucleon, as  $\mathcal{M}_{NN \rightarrow N\pi B} = \mathcal{M}_{N \rightarrow hB} \mathcal{M}_{hN \rightarrow \pi N}$ . The transverse sizes of the projectile nucleon ( $N$ ) and the outgoing nucleon ( $N$ ) and pion ( $\pi$ ) near the interaction point are of the order of  $\sim 1/\sqrt{|t'|}$ . Therefore, the factorization and the color transparency phenomena are closely related [177]. The factorization was shown for the DVMP process [177], and such studies were also done recently, including  $2 \rightarrow 3$  processes [178, 179]. Detailed factorization studies would be needed for the  $NN \rightarrow N\pi B$  processes.

The  $NN \rightarrow N\pi B$  cross section is expressed in the factorized form, as [52]

$$\begin{aligned} \frac{d\sigma_{NN \rightarrow N\pi B}}{dt dt'} &= \int_{y_{\min}}^{y_{\max}} dy \frac{s}{16(2\pi)^2 M_N p_N} \\ &\times \sqrt{\frac{(ys - t - M_N^2)^2 - 4M_N^2 t}{(s - 2M_N^2)^2 - 4M_N^4}} \frac{d\sigma_{MN \rightarrow \pi N}(s' = ys, t')}{dt'} \\ &\times \sum_{\lambda_N, \lambda_B} \frac{1}{[\phi_M(z)]^2} |\mathcal{M}_{N \rightarrow B}|^2. \end{aligned} \quad (86)$$

where the variable  $y$  is defined by  $y = s'/s$ , and  $d\sigma_{MN \rightarrow \pi N}/(dt')$  is the meson-nucleon elastic scattering cross section. This part can be estimated by using the Brookhaven National Laboratory (BNL) data by the E755 and E838 collaborations. The GPDs are contained in the matrix element  $\mathcal{M}_{N \rightarrow B}$ . If the final baryon  $B$  is a nucleon, the matrix-element part is given by the vector and axial terms as  $|\mathcal{M}_{N \rightarrow N'}|^2 = |\mathcal{M}_N^V|^2 + |\mathcal{M}_N^A|^2$ . They are given by

$$\begin{aligned} \sum_{\lambda_N, \lambda_{N'}} |\mathcal{M}_N^V|^2 &= I_N^2 \left[ 8(1 - \xi^2) \{H(x, \xi, t)\}^2 \right. \\ &\left. + 16\xi^2 H(x, \xi, t) E(x, \xi, t) - \frac{t}{M_N^2} (1 + \xi)^2 \{E(x, \xi, t)\}^2 \right], \end{aligned} \quad (87)$$

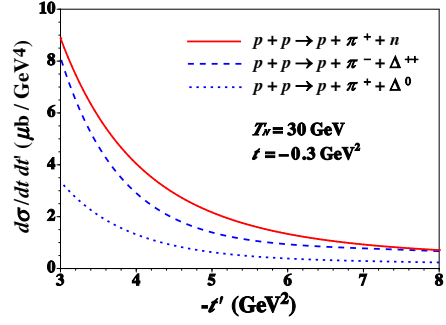


**Fig. 24** The cross sections  $d\sigma/(dtdt')$  are shown for  $p + p \rightarrow p + \pi^+ + n$ ,  $p + p \rightarrow p + \pi^- + \Delta^{++}$ , and  $p + p \rightarrow p + \pi^+ + \Delta^0$  as a function of  $t'$ .

$$\begin{aligned} \sum_{\lambda_N, \lambda_{N'}} |\mathcal{M}_N^A|^2 &= I_N^2 \left[ 8(1 - \xi^2) \{\tilde{H}(x, \xi, t)\}^2 \right. \\ &\left. + 18\xi^2 \tilde{H}(x, \xi, t) \tilde{E}(x, \xi, t) - \frac{2t\xi^2}{M_N^2} \{\tilde{E}(x, \xi, t)\}^2 \right]. \end{aligned} \quad (88)$$

Here,  $I_N$  is the isospin factor for the nucleon defined by  $I_N = \langle 1/2 || \tilde{T} || 1/2 \rangle \langle \frac{1}{2} m_N, 1m | \frac{1}{2} m'_N \rangle / \sqrt{2}$ , and its actual values are  $I_N = 1, \sqrt{2}$  for  $p \rightarrow p, n$ , respectively. The GPDs  $H, E, \tilde{H}$ , and  $\tilde{E}$  contribute to the cross section. In particular, they are estimated by considering the pion and rho as for the intermediate state  $h$ . The  $NN \rightarrow N\pi\Delta$  cross section is calculated in the same way with the transition GPDs of  $N \rightarrow \Delta$  [52].

The GPD measurements by the  $2 \rightarrow 3$  processes are possible at hadron accelerator facilities, for example, at J-PARC. It is a unique opportunity to investigate the ERBL kinematical region of the GPDs, so such experimental measurements are complementary to the DVCS and DVMP experiments at lepton accelerator facilities. The  $pp \rightarrow p\pi^+ B$  ( $B = \Delta^0, n$ ) cross sections were calculated by considering the J-PARC kinematics. In Fig. 24, the differential cross sections  $d\sigma/(dtdt')$  are shown for the three processes,  $p + p \rightarrow p + \pi^+ + n$ ,  $p + p \rightarrow p + \pi^- + \Delta^{++}$ , and  $p + p \rightarrow p + \pi^+ + \Delta^0$ , as a function of  $t'$  by taking the incident proton-beam energy 30 GeV and the momentum transfer  $t = -0.3 \text{ GeV}^2$  [52]. There are advantages of studying these reactions. The cross sections are large, and they are of the order of  $\mu\text{ barn}/\text{GeV}^2$ , these processes are simple to measure experimentally, the vacuum quantum number  $0^+$  does not contribute in the intermediate state, and the  $\Delta$  cross sections are as large as the nucleonic ones for measuring the  $N \rightarrow \Delta$  transition GPDs in addition to the nucleon GPDs.

### 8.3 Exotic hadron production using GPDs

In recent years, there have been reports on exotic hadrons. However, it is not straightforward to find a firm evidence on the exotic nature. The GPDs of exotic hadrons, including transition GPDs, could provide clear information on the exotic structure by considering the following points. The simplest form of the quark GPD  $H$  could be written in the separable form, as [180]

$$H_q^h(x, \xi = 0, t) = f_n(x) F_n^h(t, x), \quad (89)$$

where  $n$  indicates the number of valence quarks,  $h$  is a hadron,  $f_n(x)$  is a quark distribution function, and  $F_n^h(t, x)$  is a transverse form factor at  $x$ .

The exotic nature should be reflected in both the PDF and the transverse form factor [181]. For the PDFs, a simple function of  $x$

$$f_n(x) = C_n x^{\alpha_n} (1-x)^{\beta_n}, \quad (90)$$

is often used. For valence-quark distributions, the parameters  $C_n$ ,  $\alpha_n$ , and  $\beta_n$  are determined by the valence-quark number  $\int_0^1 dx f_n(x) = n$ , and the quark momentum  $\int_0^1 dx x f_n(x) = \langle x \rangle_q$ . The parameter  $\beta_n$  is determined the constituent counting rule in QCD as  $\beta_n = 2n - 3 + 2\Delta S_z$  with the spin factor  $\Delta S_z = |S_z^q - S_z^h|$ . Using these constraints together with  $\langle x \rangle_q = 0.47$ , we obtained the valence-quark distribution functions of the pion, proton, tetraquark hadron, and pentaquark hadron in Fig. 25 [181]. The pion and proton distributions roughly agree with the current PDF parametrizations at  $Q^2 = 2 \text{ GeV}^2$ . These PDFs have a clear indication of their exotic nature because the peak of the valence-quark distributions moves toward the smaller- $x$  region as  $n$  increases.

The transverse form factor  $F_n^h(t, x)$  also reflects the exotic nature. A simple exponential function could be used for the form factor, with the cutoff parameter  $\Lambda$  for the transverse momentum, as [180]

$$F_n^h(t, x) = e^{(1-x)t/(x\Lambda^2)}. \quad (91)$$

The transverse spacial density is given by its Fourier transform, and then the root-mean-square (rms) radius is given by the parameter  $\Lambda$  as  $\langle r_\perp^2 \rangle = 4(1-x)/(x\Lambda^2)$ . The transverse form factor is shown in Fig. 25 at  $x = 0.4$  by taking  $\Lambda = 0.5$  and  $1.0 \text{ GeV}$  as examples. These choices mean that the rms radii are  $\sqrt{\langle r_\perp^2 \rangle} = 0.48$  and  $0.97 \text{ fm}$  for  $\Lambda = 1.0$  and  $0.5 \text{ GeV}$ , respectively. The ‘‘ordinary’’ hadrons with the  $q\bar{q}$  and  $qqq$  configurations would have compact spatial distributions, which are shown as the hard form factor ( $\Lambda = 1.0 \text{ GeV}$ ,  $\sqrt{\langle r_\perp^2 \rangle} = 0.48 \text{ fm}$ ), whereas the exotic tetra- and pentaquark hadrons, or the molecular-type hadrons, should have wide spatial

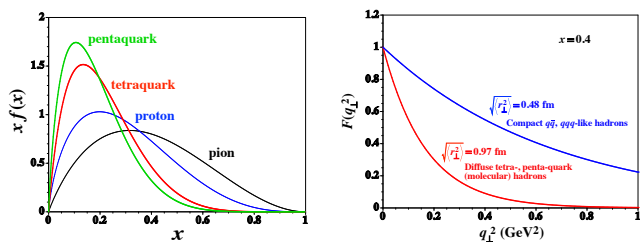


**Fig. 25** Valence-quark distributions and transverse form factors of ordinary and exotic hadrons [181].

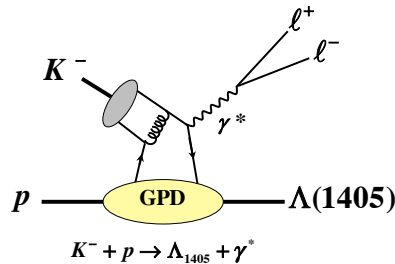


**Fig. 26** Transition GPDs for the exotic candidate  $\Lambda(1405)$ .

distributions and they have the soft form factor ( $\Lambda = 0.5 \text{ GeV}$ ,  $\sqrt{\langle r_\perp^2 \rangle} = 0.97 \text{ fm}$ ) in Fig. 25.

It is interesting to measure the GPDs for exotic hadron candidates, but their spacelike GPDs would not be measured easily because the exotic hadrons are unstable particles. However, the timelike GPDs should be measured even for unstable exotic hadrons as investigated at the KEK B factory for the pion [182, 183].

On the other hand, the exotic-hadron GPDs could be measured in the spacelike region as transition GPDs. For example, the  $\Lambda(1405)$  production process  $K^- p \rightarrow \ell^+ \ell^- \Lambda(1405)$  in Fig. 26 could be investigated at J-PARC by using the future kaon beam, as an extension project of the pion Drell-Yan process  $\pi^- N \rightarrow \ell^+ \ell^- N$  for measuring the nucleon GPDs [51, 184]. The  $\Lambda(1405)$  cannot be described by constituent-quark models, so that it is considered as a  $\bar{K}N$  molecule or a pentaquark (*wudūs*) hadron. Such transition GPDs have not been investigated both theoretically and experimentally, so future efforts are needed for these kind of studies.

There are also possibilities for studying the exotic nature in high-energy reactions by using the constituent-counting rule in perturbative QCD [185, 186] because the constituent number should be different between ordinary and exotic hadrons. This rule indicates that the cross section scales by the total number of constituents ( $n$ ) as  $d\sigma/dt \sim 1/s^{n-2}$  where  $s$  is the center-of-mass-energy squared. For example, the high energy  $\pi^- p \rightarrow K^0 \Lambda(1405)$  reaction could be measured at J-PARC [185]. There is an interesting indication that  $\Lambda(1405)$  could be a penta-quark state at medium energies and a three-quark one at high energies by the



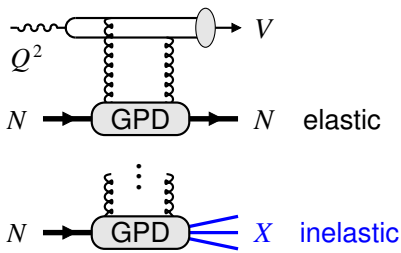


**Fig. 27** Exclusive vector meson production in diffractive channels at small  $x$  ( $V = \rho^0, \omega, \phi, J/\psi, \Upsilon$ ). The amplitude is proportional to the gluon GPD. Upper graph:  $N \rightarrow N$  transitions (elastic diffractive scattering). Lower graph:  $N \rightarrow X$  (low-mass) transitions (inelastic diffractive scattering).

analysis of photo-production data on  $\gamma p \rightarrow K^+ \Lambda(1405)$  [186].

## 9 Transition processes: diffractive scattering

### 9.1 Inelastic diffraction and quantum fluctuations

In  $eN/\gamma N$  scattering at high energies  $W \sim 10^1 - 10^2$  GeV, the dominant exclusive meson production channels are vector mesons with the same quantum numbers as the (virtual) photon,  $V = \rho^0, \omega, \phi, J/\psi, \Upsilon$ . In these channels, the production process does not exchange quantum numbers between the nucleon and the produced meson and has the characteristics of diffractive scattering. If the momentum transfer is large or the produced meson is heavy ( $Q^2, M_{Q\bar{Q}}^2 \gg 1 \text{ GeV}^2$ ), the amplitude of such high-energy exclusive processes can be factorized (see Sec. 2) and samples the gluon GPD of the nucleon at  $x, \xi \ll 1$  (see Fig. 27) [187]. At such values of  $x$  and  $\xi$  the gluon GPD is close to diagonal and can be obtained from the gluon density ( $\xi = 0$ ) in a controlled approximation [188, 189].

Now, in such high-energy exclusive processes, the nucleon can remain intact in the final state,  $N \rightarrow N$  (elastic diffractive scattering) or dissociate into a low-mass state with nucleon quantum numbers,  $N \rightarrow X$  (inelastic diffractive scattering) (see Fig. 27). According to the general theory of diffractive scattering, the elastic cross section is proportional to the quantum average squared of the strength of interaction of the high-energy probe with the target configurations, while the inelastic cross section is proportional to the quantum fluctuations, i.e., the variation of the strength of interaction between the various configurations [190, 191]. Applying these concepts to the factorized processes at high  $Q^2$ , one can show that elastic scattering probes the quantum average of the gluon density in the nucleon, while inelastic scattering probes its quantum fluctua-

tions [49]. Specifically,

$$\omega_g \equiv \frac{\langle G^2 \rangle - \langle G \rangle^2}{\langle G \rangle^2} = \left[ \frac{d\sigma_{\text{inel}}}{dt} / \frac{d\sigma_{\text{el}}}{dt} \right]_{t=0}^{\gamma_L^* N \rightarrow V X} \quad (92)$$

where  $G$  denotes the gluon density operator and  $\langle \dots \rangle$  the quantum average over configurations in the nucleon (the relation is valid at small  $x$  and  $\xi$ , where the gluon GPD can be obtained from the gluon density; see Ref. [49] for details). The relation Eq. (92) allows one to extract the quantum fluctuation of the gluon density from the ratio of inelastic and elastic diffractive scattering. Note that the relation is valid only at  $t = 0$ ; the inelastic cross section can be measured also at  $t < 0$  but is connected with the quantum fluctuations only at  $t = 0$ .

The concept of fluctuations of the gluon density and their connection with inelastic diffractive scattering are derived here in the context of collinear factorization of exclusive processes [49]. In this way, they are directly connected with the transition GPDs describing the individual amplitudes for  $N \rightarrow X$  inelastic diffractive processes. A similar relation between inelastic diffraction and the fluctuations of the gluon density has been derived in the context of the dipole model of  $eN/\gamma N$  scattering [192–194].

### 9.2 GPDs at HERA

Measurements sensitive to GPDs in lepton-proton collisions have been performed at the H1 and ZEUS HERA collider experiments. The covered photon-proton centre-of-mass energies of these experiments ranges from 30 GeV to 300 GeV, providing access hereby to  $10^{-4} \leq xB \leq 10^{-2}$ . Triggers from far-forward detectors and calorimeters allowed for the separation of elastic and dissociative diffractive events and, depending on the period of data collection, the experiments were equipped with far-forward proton spectrometers able to detect, with a coverage in acceptance of a few percent, directly the proton scattered in the elastic process. Hard diffractive production of the light mesons  $\rho^0$  [195, 196] and  $\phi$  [195, 197], of pion pairs [198] and of the quarkonia  $J/\psi$  [199–208],  $\psi(2S)$  [205, 208, 209], and  $\Upsilon$  [210, 211] have been studied in both the elastic and the dissociative channels, while the hard exclusive production of photons was limited to the elastic channel [212–216]. A weak dependence on  $W_{\gamma p}$  of the elastic diffractive cross section is observed in absence of a hard scale. In contrast, the cross section is seen to rise with increasing  $W_{\gamma p}$  in the presence of a hard scale, either through large  $Q^2$  or large heavy-quark mass, where the rise is steeper for increasing values of the hard scale.

This behaviour reflects the increase in gluon density with smaller  $x_B$  (or larger  $W_{\gamma p}$ ). The measurements of the elastic channel also show a  $t$  slope,  $b$ , evolving from large values in the absence of a hard scale to a small, constant value once a sufficiently hard scale is reached, and this irrespective of the produced final-state particle. In the dipole picture this can be understood as  $b$  being a reflection of the transverse dipole size and the transverse proton size, where at large scales the dipole size becomes negligible. For the inelastic channel, a very different  $t$  dependence is observed. Spin-density matrix elements (SDMEs), which are related to the GPDs, have been extracted for DVMP process from the H1 and ZEUS data through the measurement of the angular distribution of the meson decay products. It is observed that for quarkonia  $s$ -channel helicity is conserved and that, apart from some slight deviations for some SDMEs, the same is true for the light vector mesons. This is in contrast with the low-energy, fixed-target experiments, where for some SDMEs a strong violation of  $s$ -channel helicity conservation is observed, see *e.g.* [217]. The extracted SDMEs at the collider experiments also indicate that the interaction between the virtual photon and beam proton proceeds through the exchange of particles of natural parity, which can be at first order equated to the exchange of two gluons. Also here, differences are seen with the fixed-target experiments, where at low energy unnatural-parity exchange also seems to contribute [218]. Finally, an increase in dominance of the longitudinal cross section over the transverse cross section with increasing values of  $Q^2$  has been observed both for the light and the heavy mesons. In relation to the measurement of processes involving transitions of the beam proton to another state, the H1 experiment performed a measurement of  $e+p \rightarrow \rho^0+n+\pi^+$  with  $Q^2 < 2$  GeV, where the  $\rho^0$  meson is reconstructed in the central detector, the neutron is tagged in a forward detector system and the  $\pi^+$  escapes along the beam line without being detected [219]. The interpretation of this interaction can be attributed to scattering off the proton pion cloud or off the neutron core, but also to the creation of a  $N^*$  resonance, which subsequently decays into  $\pi^+n$ . The measurement of this process exemplifies one possibility to study transition GPDs at electron-proton colliders.

### 9.3 Transition GPDs in ultraperipheral collisions

Ultra-peripheral collisions of hadrons at very high energies can be used to access GPDs. Hard exclusive production, in particular, the photoproduction of heavy quarkonium ( $J/\psi$ ,  $\psi(2S)$ ,  $\Upsilon(nS)$ ) states, have been studied in  $\gamma-p$  and  $\gamma$ -lead nucleus collisions at RHIC

and at the LHC [11], providing unique access to the low  $x_B$  region, down to  $x_B = 10^{-6}$ . We focus here on  $\gamma$ - $p$  reactions. They can be studied in proton-proton collisions and in proton-nucleus collisions at these two running hadron colliders.

For the access to GPDs through meson production, the quasi-real nature of the exchanged photon, is limiting the useful studies to the production of quarkonia, while there are also proposals to study exclusive photon-meson pair production at sufficiently high invariant mass [220, 221] as to introduce the needed hard scale. Exclusive production of the quarkonia  $J/\psi$ ,  $\psi(2S)$  and  $\Upsilon$  has been successfully studied in proton-proton [222–225], proton lead [47, 48, 226] and lead-lead collisions [227–234]. The photon-proton cross sections for exclusive  $J/\psi$  production extracted from the measurements in lepton-proton, proton-proton, and lead-proton collisions are compatible with each other in the common  $W_{\gamma p}$  range, which hints at the universality of the underlying probed physics. At present, the exclusive quarkonium production cross section has been used in the study of standard PDFs [235], but not yet to constrain GPDs.

A measurement of the DVCS process is not possible due to the small virtuality of the initial state photon that originates from the electrostatic field of the colliding ultra-relativistic ions. Time-like Compton scattering measurements are in principle possible [236]. A  $t$ -integrated cross section result on exclusive dilepton production in  $\gamma-p$  collisions already exists in a kinematic domain of interest (dilepton mass between 1 and 2.5 GeV/ $c^2$ ) [237].

In addition to hard exclusive photoproduction, ultra-peripheral collisions allow the study of hard dissociative photoproduction processes at high energies, where the target proton breaks up. This observable class is within the Good-Walker-formalism sensitive to the fluctuations of the proton structure [238], whereas the exclusive production is sensitive to the average. A first measurement of dissociative  $J/\psi$  photoproduction in  $\gamma$ - $p$  collisions has been published recently [237]. Future measurements at the LHC can be expected based on the interest of the community and the luminosity increase in the 2020s compared to previous data taking campaigns, thanks to the HL-LHC upgrades [239].

Ultra-peripheral collisions can also be studied in the fixed-target mode of the LHC ( $\sqrt{s} \approx 100$  GeV). A few observables and corresponding publications are summarized in Ref. [240]. LHCb performed with the SMOG gas target originally designed for luminosity measurements via beam imaging [241], a first set of low luminosity cross section measurements, *e.g.*, on charm and on antiproton production [242, 243].

Transition GPDs can, in principle, be accessed within dissociative production provided that the final state nucleon resonance can be at least partially reconstructed. At the existing hadron colliders, this is a difficult undertaking given the existing forward instrumentation. Dedicated simulation studies are required to assess the feasibility with the current experimental set-ups or with dedicated additional instrumentation.

## 10 Future experimental facilities

The data from already existing measurements allows the first extraction of observable, sensitive to transition GPDs. However, for more detailed studies, higher statistics and also higher beam energies are favorable. In addition, hadron beams at J-PARC will allow the study of transition GPDs in hadronic reactions. The following section will summarize upcoming opportunities with existing and planned experiments.

### 10.1 CLAS12 luminosity upgrade and JLab 22 GeV

The  $N \rightarrow N^*$  DVCS, as well as the  $N \rightarrow N^*$  DVMP processes will both strongly profit from a luminosity upgrade of CLAS12 as well as from an energy upgrade of JLab.

From the statistics point of view, the low efficiency for the detection of the multi-particle final states, in combination with the background suppression cuts, strongly limit the available statistics of the final sample. At the moment, the statistics that can be collected with CLAS12 are mainly limited by the rate capability of the detector, which is determined primarily by the forward tracking in the drift chambers, while the CEBAF accelerator could deliver around two orders of magnitude more beam current. Therefore, a luminosity upgrade of CLAS12, which is currently in progress, will help collect data more efficiently and increase the amount of data that can be collected in a certain time. Based on this upgrade, it is expected that sufficient data can be collected in a reasonable time frame to perform a fully differential study of the  $N \rightarrow N^*$  DVCS and DVMP processes, which will allow a partial wave decomposition of the resonance spectrum.

From the beam energy point of view, the currently available beam energy of 10.6 GeV allows a study of the lower lying nucleon and  $\Delta$  resonances in a limited  $Q^2$  range. However, especially for higher-mass resonances, the factorization requirement  $Q^2 \gg m_{N^*}^2$  strongly limits the options based on a 10.6 GeV electron beam. Here, a 22 GeV upgrade of JLab would enable the investigation of higher-mass resonances and extend the ac-

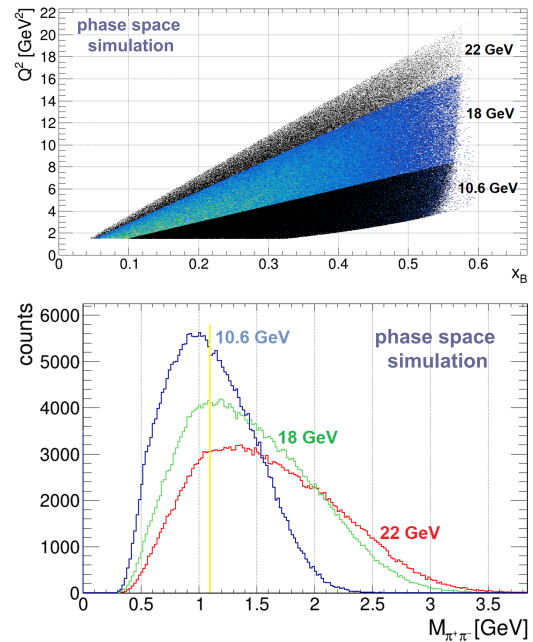


**Fig. 28** Comparison of the available phase space, accessible with the present CLAS12 setup, in  $Q^2 - x_B$  or the  $\pi^- \Delta^{++}$  process under forward kinematics ( $-t < 1.5$  GeV<sup>2</sup>) [up] and for the  $\pi^+ \pi^-$  invariant mass of the same process, which is used to suppress the dominant  $\rho$  production background by the cut on  $M(\pi^+ \pi^-) > 1.1$  GeV, indicated by the yellow line [down] for a 10.6 GeV, 18 GeV and 22 GeV electron beam.

cessible  $Q^2$  range for the lower mass resonances. Based on this extended range, a detailed study of the scaling behavior of the different observables will become possible. Fig. 28 shows the available phase space, accessible with the present CLAS12 setup, in  $Q^2 - x_B$  for the  $\pi^- \Delta^{++}$  process under forward kinematics and the  $\pi^+ \pi^-$  invariant mass of the same process for a 10.6 GeV, 18 GeV, and 22 GeV electron beam. The corresponding distributions of the  $N \rightarrow \Delta$  DVCS process show similar characteristics. It can be seen that a 22 GeV upgrade of JLab would provide a significantly increased  $Q^2$  range for a fixed value of  $x_B$ . This leads to a big advantage for the study of these processes, since the factorization of the  $N \rightarrow N^*$  DVCS and DVMP processes requires a high virtuality  $Q^2$  to be above the resonance mass squared. While this condition can already be fulfilled with a 10.6 GeV electron beam for lower mass resonances, like the  $\Delta(1232)$ , an energy upgrade to 22 GeV will be a big advantage to ensure the factorization of the process for higher mass resonances and to study the scaling behavior of the observables. As shown in the lower part of Fig. 28 the increase in phase space for the different invariant mass combinations will allow a more efficient suppression of non-resonant background from exclusive meson production and also from other (differently charged) nucleon reso-

nance production channels, which is mostly expected at lower masses. Higher beam energies will therefore also provide a more efficient event selection and a better suppression of the non-resonant background. While the presently available 10.6 GeV electron beam already allows a study of the 3D structure of lower-mass nucleon resonances, a 22 GeV upgrade of JLab in combination with a luminosity upgrade of CLAS12 will provide ideal conditions for the study of the 3D structure of nucleon resonances via transition GPDs. Also, future studies with the high resolution two arm spectrometer in JLab hall C will strongly benefit from an energy upgrade.

### 10.2 Muon and meson beams at COMPASS/AMBER

So far, no physics program for the measurement of transition GPDs at COMPASS [244] or AMBER [245] exists. However, the existing COMPASS data based on a 160 GeV muon beam will provide a potential access to lower  $x_B$  ( $0.01 < x_B < 0.2$ ) and higher  $Q^2$  values. It can therefore help to constrain the impact of sea quarks on the resonance properties and also provide valuable inputs for an extrapolation to the gluonic regime, accessible with the EIC.

Since the main spectrometer of COMPASS is focused at very forward angles and provides relatively high momentum thresholds, it can only be used to detect the scattered muons and the DVCS photon or DVMP pion. The decay products of the resonance have to be detected by the CAMERA detector, which consists of two regions of plastic scintillator bars, covering the region around the target. Since only charged tracks can be detected by this device, it mainly limits the channels that can be studied with COMPASS to two  $N \rightarrow N^*$  DVMP channels:

- $\mu^\pm p \rightarrow \mu^\pm \pi^- \Delta^{++} \rightarrow \mu^\pm \pi^- [p\pi^+]$
- $\mu^\pm p \rightarrow \mu^\pm \pi^+ \Delta^0(N^*) \rightarrow \mu^\pm \pi^+ [p\pi^-]$

Currently, feasibility studies for these two channels are ongoing based on existing data taken with COMPASS in 2016. With AMBER also the high-intensity pion and kaon beams with up to 190 GeV/c are expected to provide an excellent basis for the study of meson induced transitions within the exclusive Drell-Yan process. Feasibility studies for potential future muon and meson based measurements with AMBER, including potential detector upgrades, are planned.

### 10.3 Electron-Ion Collider EIC

The planned electron-ion collider (EIC) [246] will allow an extension of the kinematic regime to the gluonic sector at low  $x_B$  and towards higher  $Q^2$  values (see Fig.

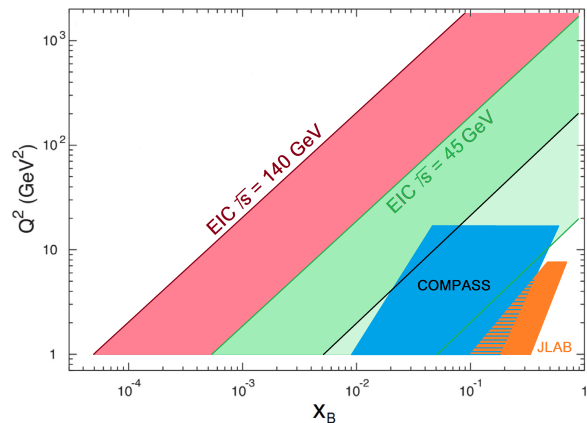


**Fig. 29** Comparison of the available phase space in  $Q^2 - x_B$ , accessible with a 12 GeV electron beam at JLab (orange), a 160 GeV muon beam at COMPASS (blue) and different CM energies of the EIC (green, red).

29), which are especially important for the factorization of the process in relation to higher mass resonances.

The upcoming data from the EIC will provide insights into the contributions of the gluons to the excitation process and to the characteristics of baryon resonances. The planned configuration of the far-forward detectors will provide excellent opportunities to study the low  $-t$  region of hard exclusive processes. So far, no theoretical predictions exist for the low  $x_B$  regime of the  $N \rightarrow N^*$  DVCS and DVMP processes, but following the predictions for the ground-state DVCS and DVMP processes in this regime, a measurement is expected to be feasible from the cross section point of view.

### 10.4 Hadron beams at J-PARC and FAIR

As discussed in section 8, theoretical models also allow the study of transition GPDs with hadronic beams in  $2 \rightarrow 3$  processes and based on the exclusive Drell-Yan process. The high-momentum hadron beam line of J-PARC [12] provides excellent opportunities for such studies. Further opportunities with proton and antiproton beams in a similar energy region will become available at the Facility for Antiproton and Ion Research (FAIR) [247].

The feasibility of measuring the  $2 \rightarrow 3$  process in the ongoing E16 experiment in the high-momentum beamline of J-PARC is currently investigated. Equipping additional detectors in the forward direction will become necessary to increase the acceptance of these exclusive hard events. Also studies of this process at FAIR may be considered and further investigated.

For the measurement of the exclusive Drell-Yan process in the E50 experiment, a letter of intent [184] was

submitted to J-PARC 2019 PAC. A full proposal with the design of the required mu-ID system and dimuon trigger setting is currently being prepared. The “ $\pi 20$ ” project of delivering 10-20 GeV meson beam in the high-momentum beamline of J-PARC’s hadron hall has been included in the hadron hall extension project [12]. This six-year project has been selected as the top priority in the KEK mid-term plan (KEK-PIP2022) and is scheduled to start in 2024. After the upgrade, high resolution pion beams with a momentum of up to 20 GeV will be available.

### 10.5 LHC fixed-target and ultraperipheral collisions

In 2024, results from the first unpolarised fixed-target set-up for high-luminosity data takings at the LHC are expected from LHCb SMOG-2 [248, 249]. This set-up, installed in 2022 will allow to run LHCb in fixed-target and collider mode in parallel throughout the full data taking period and with up to two orders of magnitude larger instantaneous luminosities than SMOG, depending on the gas. An effort towards a polarized gas target in LHCb is ongoing [250].

With the HL-LHC upgrades [239] also future measurements of dissociative  $J/\psi$  photoproduction in  $\gamma - p$  collisions at the LHC can be expected with significantly increased statistics. However, the relevant luminosity increase strongly depends on the experimental set-up, collision system, and operational decisions.

## 11 Challenges of GPD analysis

It is instructive to compare the phenomenology of transition GPDs with that of diagonal counterparts, the latter of which has been extensively studied over the last three decades. Both types of objects naturally shares many similar features, however studies of transition GPDs come with a number of unique difficulties.

Both cases require the simultaneous extraction of several multidimensional objects from observables for exclusive processes, presenting a non-trivial task. Specifically, distinguishing among many contributing objects can only be achieved by measuring a variety of exclusive processes (DVCS, TCS, DDVCS, DVMP, *etc.*) and observables (cross-sections, beam / target / charge asymmetries, *etc.*). This motivates a global experimental program conducted in laboratories covering complementary kinematic domains, and diverse setups equipped with sophisticated detection systems capable of determining the exclusivity condition. In the case of diagonal GPDs, the experimental programs carried out

in laboratories such as JLab, DESY, and CERN have already resulted in numerous measurements, fueling phenomenological analyses like [95, 251, 252]. As indicated in Sec. 7, so far only the first data sensitive to transition GPDs have been collected, allowing for exploratory studies that help to prove the correctness and usefulness of the formalism. We stress again that processes sensitive to both diagonal and transition GPDs can, in principle, be measured together. However, the latter typically come with smaller cross-sections and are more prone to detector effects threatening the reconstruction of all particle states.

Similarly to diagonal counterparts, transition GPDs also enter observables via convolutions with coefficients describing the hard part of a given process, and, in the case of, for example, DVMP, also with additional non-perturbative objects describing produced hadrons. This requires the development of sophisticated deconvolution methods, which in practice for processes like DVCS and lowest-order coefficient functions turns out to be an arduous task (for a full discussion, see both Refs. [253] and [254]). Despite this difficulty, the phenomenology of diagonal GPDs demonstrates that analyses of amplitudes (not requiring deconvolution) still allow us to learn a lot about the structure of hadrons. In particular, one can directly study the nuclear tomography at low  $\xi$  thanks to certain similarities with the optical theorem [10, 214, 216], mechanical properties via the subtraction constant appearing in the dispersion relation [93, 251, 255], and response of hadrons on probes carrying different angular momenta thanks to the recent development of techniques based on the Froissart-Gribov projections [256]. The same can be done in the non-diagonal case, assuming experimental data allow for it.

Another common challenge is defining models that fulfill a maximum of theory-driven requirements. This proves to be a challenge, particularly due to the non-trivial task of combining polynomiality with positivity constraints. Many modelling techniques have been proposed in the diagonal case, including those involving Radyushkin’s double distribution Ansatz [257–259], conformal moment expansion [252, 260], dual parametrization [261–263] and light front wave functions [264]. This selection is supplemented by non-parametric models based on machine learning techniques [265] used to study model dependency. All these modelling techniques can be re-used in the non-diagonal case. The issue of incorporating diagonal GPDs into models of non-diagonal objects relying on the large  $N_c$  limit, as discussed in Ref. [26], remains an open and interesting phenomenological issue. Additional difficulty arises from the limited knowledge of forward limits and

elastic form factors, which are used as basic ingredients in the modeling procedures; see, for instance, Eqs. (8) and (9).

It is also very important to generalize for non-diagonal hard exclusive reaction the consistent methods for accounting the higher-order kinematical effects relying on the approaches developed in Refs. [266–268].

Assuming we have experimental data and a model we would like to constrain, and we understand well the connection between these data and the model, the last non-trivial task is the creation of an extraction framework. In this framework, all elements needed for the extraction must be implemented and well-tested. Since we expect data to span a broad kinematic domain, to fully facilitate their potential, it is required to use evolution equations, but also a suitable description of exclusive processes, particularly in terms of  $\alpha_S$  and twist expansions. Evolution also acts as a useful tool, allowing us to distinguish between various contributions. For instance, in the analysis of the subtraction constant, evolution allows us to decompose this object to access the part related to the energy-momentum tensor form factor  $C$  [255]. In the GPD field, two open-source platforms dedicated to diverse phenomenological studies exist: Gepard [269] and PARTONS [270]. Both of them can be adapted to the non-diagonal case.

The constrained models can be employed in Monte Carlo generators to support ongoing and future experimental campaigns, such as those planned at JLab [45] and EIC [13]. The generators should incorporate radiative corrections, the understanding of which is crucial for interpreting data, and ideally, they should be capable of generating multiple exclusive processes. A potential candidate for such a generator is EpIC [271], which, due to its modular architecture, can easily accommodate elements required to generate events related to non-diagonal GPDs.

## 12 Future transition GPD program

Transition GPDs provide new tools for quantifying and interpreting the structure of baryon resonances in QCD. The transition GPDs describe matrix elements of non-local partonic QCD operators between ground and excited baryon states and contain much more information than vector/axial transition current traditionally used for resonance excitation. They provide a tomographic image of spatial structure of resonances and contain information about mechanical properties such as angular momentum and forces. Systematic theoretical methods are available for characterizing the  $N \rightarrow N^*$  transition GPDs and connecting them with the  $N \rightarrow N$  ground state GPDs.

Transition GPDs are sampled in hard exclusive electroproduction processes with  $N \rightarrow N^*$  transitions, such as DVCS  $e + N \rightarrow e' + \gamma + N^*$  and meson production  $e + N \rightarrow e' + M + N^*$ . QCD factorization is applied to the amplitudes along the same lines as for  $N \rightarrow N$  processes. First experimental results from JLab 12 GeV in  $\pi^- \Delta^{++}$  and  $\pi^0 \Delta^+$  meson production, as well as  $p \rightarrow \Delta^+$  DVCS, demonstrate the feasibility of the measurements and provide a first test of the applicability of framework. Much more extensive data are expected from the ongoing JLab 12 GeV program. Further measurements of transition processes in electron/muon scattering could be performed with COMPASS, EIC and the possible JLab 22 GeV upgrade. Complementary information comes from hadron-induced processes such as exclusive dilepton production  $\pi + N \rightarrow (\ell^+ \ell^-) + N^*$ , which will be measured at J-PARC. The concept of transition GPDs can also be applied to gluon-mediated diffractive scattering at small  $x$ , with measurements performed in ultraperipheral collisions at LHC and photo/electroproduction at the future EIC.

This opens the prospect of a new scientific program exploring baryon resonance structure, using transition GPDs as a unifying concept and quantitative analysis tool. To realize this program, further efforts are needed to develop the theoretical framework, extend the experimental studies at existing facilities, and simulate measurements with future facilities. On the theoretical side, this includes:

- Revisit and standardize the structural decomposition of the  $N \rightarrow \Delta$  transition matrix elements; establish the connections between the various definitions of transition GPDs used in the literature; clarify the manifestation of their basic properties in the different parametrizations. Extend the structural decomposition to other  $N \rightarrow N^*$  transition GPDs.
- Construct a general formalism for non-diagonal hard exclusive reactions based on  $N \rightarrow \pi N$  transition GPDs in the full  $\pi N$  resonance domain, using methods of amplitude analysis to separate resonant and non-resonant contributions. To avoid complications associated with the spins of the target and produced hadrons, a first step might be to treat the toy example of  $\pi \rightarrow \pi\pi$  transition GPDs.
- Develop the interpretation of the EMT transition form factors and the mechanical properties of baryon resonances, using representations of the transition matrix elements in terms of 2-dimensional light-front densities or 3-dimensional Breit frame densities.

- Apply the  $1/N_c$  expansion to achieve a complete classification of the  $N \rightarrow \Delta$  transition GPDs, including subleading structures and  $1/N_c$  corrections to leading structures, using algebraic methods based on the spin-flavor symmetry group. Extend the  $1/N_c$  analysis to  $N \rightarrow N^*$  transitions with mass difference  $\mathcal{O}(N_c^0)$  and orbital excitations.
- Explore quantitative features of transition GPDs in dynamical models of baryons such as light-front quark models, the chiral quark-soliton model based on the large- $N_c$  limit, relativistic bound state models based on Dyson-Schwinger equations, or GPD models based on holographic QCD.
- Classify and compute kinematic power corrections and dynamic higher-twist corrections in non-diagonal DVCS process
- Develop and implement the transition GPD formalism for hard exclusive reactions with strangeness production  $\gamma^*N \rightarrow \{A, \Sigma\}K$ , using methods of SU(3) flavor symmetry. Study the feasibility of strange baryon production in the kinematic conditions of JLab, EIC and EicC.
- Develop dynamical models of diffractive  $N \rightarrow X$  gluon transition GPDs at small  $x$  based on quantum fluctuations of the gluon fields in the nucleon; explore sensitivity and impact of measurements of inelastic diffraction in ultraperipheral  $pA$  collisions at LHC and in photo/electroproduction at EIC and EicC.
- Explore applications of non-diagonal hard exclusive reactions with  $N \rightarrow \pi N$  transitions to resonance spectroscopy, particularly the production of exotic states enriched by large gluonic or multiquark components. This requires employing theoretical tools developed for conventional partial wave analysis, such as the  $K$ -matrix approach,  $N/D$ -method, dispersive methods *etc.*
- Calculate and interpret polarization observables depending on the decay angles of the meson-nucleon system, as a necessary step towards hadron spectroscopy applications.
- Perform cross section measurements of the  $p \rightarrow \Delta$  transition and a potential L-T separation of the unpolarized cross section for certain  $N \rightarrow N^*$  DVMP processes in JLab Hall C.
- Explore the options for transition GPD measurements with a possible 22 GeV upgrade of JLab, extending the phase space and kinematic coverage for hard exclusive processes, especially in  $Q^2$ , and allowing for more efficient background separation.
- Investigate the possibilities for measuring DVMP reactions with hyperon transitions at JLab 12 GeV, to probe the nucleon-to-hyperon transition GPDs.
- Explore options for studies of transition GPDs with muon and meson beams at CERN COMPASS/AMBER.
- Simulate transition GPD measurements with EIC using the far-forward detectors, especially  $N \rightarrow \Delta$  transition processes in EIC kinematics. Far-forward  $\Delta$  detection can use complementary decay channels, *e.g.*  $\Delta^+ \rightarrow \pi^+n$  or  $\pi^0p$  (= one charged and one neutral particle),  $\Delta^0 \rightarrow \pi^-p$  or  $\pi^0n$  (= all charged or all neutral particles); each of these channels present particular challenges or opportunities. The detection of far-forward pions is also needed for the  $u$ -channel exclusive processes.
- Study opportunities for transition GPD measurements at J-PARC, which will provide access to the time-like regime and are complementary to lepton scattering experiments.
- Simulate measurements of diffractive transition GPDs  $p \rightarrow X$  in ultraperipheral collisions at the LHC.

Altogether, the available theoretical concepts and methods and the existing and planned experimental facilities provide excellent opportunities for measurements of transition GPDs and next-generation studies of baryon resonances.

### 13 Acknowledgements

The workshop on “Exploring resonance structure with transition GPDs” has been supported by STRONG-2020 “The strong interaction at the frontier of knowledge: fundamental research and applications” which received funding from the European Union’s Horizon 2020 research and innovation program under grant agreement No 824093, by the European Centre for Theoretical Studies in Nuclear Physics and Related Areas (ECT\*) and by the Asia Pacific Center for Theoretical Physics (APCTP).

S. Diehl was partially supported by Deutsche Forschungsgemeinschaft Project No. 508107918 and the

On the experimental side, this includes:

- Perform high statistics, fully differential measurements of the  $N \rightarrow N^*$  DVMP and DVCS processes with CLAS12, enabling a full partial wave decomposition of the resonance spectrum. For this purpose, an upgrade of the rate capability of CLAS12 will be essential to fully exploit the luminosity which can be provided by CEBAF at JLab. Adding a calorimeter to the central detector of CLAS12 would allow for the detection of further final states for both processes.

German Bundeministerium für Bildung und Forschung (BMBF).

S. Kumano was partially supported by Japan Society for the Promotion of Science (JSPS) Grants-in-Aid for Scientific Research (KAKENHI) Grant Numbers 19K03830 and 24K07026.

K. Semenov-Tian-Shansky was supported by Basic Science Research Program through the National Research Foundation of Korea (NRF) funded by the Ministry of Education RS-2023-00238703; and under Grants No. NRF-2018R1A6A1A06024970 (Basic Science Research Program); and by the Foundation for the Advancement of Theoretical Physics and Mathematics “BASIS”.

M. Vanderhaeghen was supported by the Deutsche Forschungsgemeinschaft (DFG, German Research Foundation), in part through the Cluster of Excellence [Precision Physics, Fundamental Interactions, and Structure of Matter] (PRISMA<sup>+</sup> EXC 2118/1) within the German Excellence Strategy (Project ID 39083149).

The work presented by A. Usman was supported by Natural Science and Engineering Research Council of Canada (NSERC) Grant No. SAPIN-2021-00026 and the National Science Foundation of USA (NSF) Grant No. PHY2012430 and PHY2309976

Parada T. P. Hutaeruk was supported by the National Research Foundation of Korea Grant Nos. 2018R1A5A1025563, 2022R1A2C1003964, 2022K2A9A1A0609176, and 2023R1A2C1003177.

C.-H. Lee was supported by the National Research Foundation of Korea(NRF) grant funded by the Korea government(MSIT) (No. 2023R1A2C1005398).

H.-D. Son was supported by the National Research Foundation of Korea(NRF) grant funded by the Korea government(MSIT) (RS-2023-00210298).

This material is based upon work supported by the U.S. Department of Energy, Office of Science, Office of Nuclear Physics under contract DE-AC05-06OR23177.

The research reported here takes place in the context of the Topical Collaboration “3D quark-gluon structure of hadrons: mass, spin, tomography” (Quark-Gluon Tomography Collaboration) supported by the U.S. Department of Energy, Office of Science, Office of Nuclear Physics.

## References

1. F. Gross, et al., 50 Years of Quantum Chromodynamics, *Eur. Phys. J. C* 83 (2023) 1125. [arXiv:2212.11107](#), [doi:10.1140/epjc/s10052-023-11949-2](#).
2. K. D. Marquez, D. P. Menezes, H. Pais, C. Providência,  $\Delta$  baryons in neutron stars, *Phys. Rev. C* 106 (5) (2022) 055801. [arXiv:2206.02935](#), [doi:10.1103/PhysRevC.106.055801](#).
3. J. E. Amaro, M. B. Barbaro, J. A. Caballero, R. González-Jiménez, G. D. Megias, I. Ruiz Simo, Electron- versus neutrino-nucleus scattering, *J. Phys. G* 47 (12) (2020) 124001. [arXiv:1912.10612](#), [doi:10.1088/1361-6471/abb128](#).
4. D. Müller, D. Robaschik, B. Geyer, F. M. Dittes, J. Hořejši, Wave functions, evolution equations and evolution kernels from light ray operators of QCD, *Fortsch. Phys.* 42 (1994) 101–141. [arXiv:hep-ph/9812448](#), [doi:10.1002/prop.2190420202](#).
5. A. V. Radyushkin, Nonforward parton distributions, *Phys. Rev. D* 56 (1997) 5524–5557. [arXiv:hep-ph/9704207](#), [doi:10.1103/PhysRevD.56.5524](#).
6. X.-D. Ji, Deeply virtual Compton scattering, *Phys. Rev. D* 55 (1997) 7114–7125. [arXiv:hep-ph/9609381](#), [doi:10.1103/PhysRevD.55.7114](#).
7. S. Diehl, Experimental exploration of the 3D nucleon structure, *Prog. Part. Nucl. Phys.* 133 (2023) 104069. [doi:10.1016/j.pnpnp.2023.104069](#).
8. V. D. Burkert, et al., The CLAS12 Spectrometer at Jefferson Laboratory, *Nucl. Instrum. Meth. A* 959 (2020) 163419. [doi:10.1016/j.nima.2020.163419](#).
9. D. Dutta, et al., [Wide Angle, Exclusive Photo-production of  \$\pi^0\$  Mesons](#) (2014). URL [https://www.jlab.org/exp\\_prog/proposals/14/PR12-14-005.pdf](https://www.jlab.org/exp_prog/proposals/14/PR12-14-005.pdf)
10. R. Akhunzyanov, et al., Transverse extension of partons in the proton probed in the sea-quark range by measuring the DVCS cross section, *Phys. Lett. B* 793 (2019) 188–194, [Erratum: *Phys.Lett.B* 800, 135129 (2020)]. [arXiv:1802.02739](#), [doi:10.1016/j.physletb.2019.04.038](#).
11. S. Klein, P. Steinberg, Photonuclear and Two-photon Interactions at High-Energy Nuclear Colliders, *Ann. Rev. Nucl. Part. Sci.* 70 (2020) 323–354. [arXiv:2005.01872](#), [doi:10.1146/annurev-nucl-030320-033923](#).
12. K. Aoki, et al., Extension of the J-PARC Hadron Experimental Facility: Third White Paper (10 2021). [arXiv:2110.04462](#).
13. R. Abdul Khalek, et al., Science Requirements and Detector Concepts for the Electron-Ion Collider: EIC Yellow Report, *Nucl. Phys. A* 1026 (2022) 122447. [arXiv:2103.05419](#), [doi:10.1016/j.nuclphysa.2022.122447](#).



14. V. D. Burkert, et al., Precision studies of QCD in the low energy domain of the EIC, *Prog. Part. Nucl. Phys.* 131 (2023) 104032. [arXiv:2211.15746](#), [doi:10.1016/j.ppnp.2023.104032](#).
15. D. P. Anderle, et al., Electron-ion collider in China, *Front. Phys. (Beijing)* 16 (6) (2021) 64701. [arXiv:2102.09222](#), [doi:10.1007/s11467-021-1062-0](#).
16. K. Goeke, M. V. Polyakov, M. Vanderhaeghen, Hard exclusive reactions and the structure of hadrons, *Prog. Part. Nucl. Phys.* 47 (2001) 401–515. [arXiv:hep-ph/0106012](#), [doi:10.1016/S0146-6410\(01\)00158-2](#).
17. M. Diehl, Generalized parton distributions, *Phys. Rept.* 388 (2003) 41–277. [arXiv:hep-ph/0307382](#), [doi:10.1016/j.physrep.2003.08.002](#).
18. A. V. Belitsky, A. V. Radyushkin, Unraveling hadron structure with generalized parton distributions, *Phys. Rept.* 418 (2005) 1–387. [arXiv:hep-ph/0504030](#), [doi:10.1016/j.physrep.2005.06.002](#).
19. M. Burkardt, Impact parameter dependent parton distributions and off forward parton distributions for  $\zeta \rightarrow 0$ , *Phys. Rev. D* 62 (2000) 071503, [Erratum: *Phys.Rev.D* 66, 119903 (2002)]. [arXiv:hep-ph/0005108](#), [doi:10.1103/PhysRevD.62.071503](#).
20. M. Burkardt, Impact parameter space interpretation for generalized parton distributions, *Int. J. Mod. Phys. A* 18 (2003) 173–208. [arXiv:hep-ph/0207047](#), [doi:10.1142/S0217751X03012370](#).
21. M. V. Polyakov, P. Schweitzer, Forces inside hadrons: pressure, surface tension, mechanical radius, and all that, *Int. J. Mod. Phys. A* 33 (26) (2018) 1830025. [arXiv:1805.06596](#), [doi:10.1142/S0217751X18300259](#).
22. C. Lorcé, H. Moutarde, A. P. Trawiński, Revisiting the mechanical properties of the nucleon, *Eur. Phys. J. C* 79 (1) (2019) 89. [arXiv:1810.09837](#), [doi:10.1140/epjc/s10052-019-6572-3](#).
23. R. L. Workman, et al., Review of Particle Physics, *PTEP* 2022 (2022) 083C01. [doi:10.1093/ptep/ptac097](#).
24. M. Düren, DVCS and associated processes at HERMES, *EPJ Web Conf.* 73 (2014) 02014. [doi:10.1051/epjconf/20147302014](#).
25. S. Diehl, et al., First Measurement of Hard Exclusive  $\pi^- \Delta^{++}$  Electroproduction Beam-Spin Asymmetries off the Proton, *Phys. Rev. Lett.* 131 (2) (2023) 021901. [arXiv:2303.11762](#), [doi:10.1103/PhysRevLett.131.021901](#).
26. P. Kroll, K. Passek-Kumerički, Transition GPDs and exclusive electroproduction of  $\pi - \Delta(1232)$  final states, *Phys. Rev. D* 107 (5) (2023) 054009. [arXiv:2211.09474](#), [doi:10.1103/PhysRevD.107.054009](#).
27. U. Özdem, K. Azizi, Gravitational transition form factors of  $N(1535) \rightarrow N$ , *Phys. Rev. D* 101 (5) (2020) 054031. [arXiv:1912.06375](#), [doi:10.1103/PhysRevD.101.054031](#).
28. M. V. Polyakov, A. Tandogan, Comment on “Gravitational transition form factors of  $N(1535) \rightarrow N$ ”, *Phys. Rev. D* 101 (11) (2020) 118501. [doi:10.1103/PhysRevD.101.118501](#).
29. J.-Y. Kim, Parametrization of transition energy-momentum tensor form factors, *Phys. Lett. B* 834 (2022) 137442. [arXiv:2206.10202](#), [doi:10.1016/j.physletb.2022.137442](#).
30. J.-Y. Kim, H.-Y. Won, J. L. Goity, C. Weiss, QCD angular momentum in  $N \rightarrow \Delta$  transitions, *Phys. Lett. B* 844 (2023) 138083. [arXiv:2304.08575](#), [doi:10.1016/j.physletb.2023.138083](#).
31. P. Schweitzer, C. Weiss, Spin-flavor structure of chiral-odd generalized parton distributions in the large- $N_c$  limit, *Phys. Rev. C* 94 (4) (2016) 045202. [arXiv:1606.08388](#), [doi:10.1103/PhysRevC.94.045202](#).
32. P. V. Pobylitsa, M. V. Polyakov, M. Strikman, Soft pion theorems for hard near threshold pion production, *Phys. Rev. Lett.* 87 (2001) 022001. [arXiv:hep-ph/0101279](#), [doi:10.1103/PhysRevLett.87.022001](#).
33. J.-W. Chen, M. J. Savage, Soft pion emission in DVCS, *Nucl. Phys. A* 735 (2004) 441–448. [arXiv:nucl-th/0308033](#), [doi:10.1016/j.nuclphysa.2004.02.005](#).
34. P. A. M. Guichon, L. Mossé, M. Vanderhaeghen, Pion production in deeply virtual Compton scattering, *Phys. Rev. D* 68 (2003) 034018. [arXiv:hep-ph/0305231](#), [doi:10.1103/PhysRevD.68.034018](#).
35. M. C. Birse, Comment on soft-pion emission in DVCS, *J. Phys. G* 31 (2005) B7–B10. [arXiv:hep-ph/0503076](#), [doi:10.1088/0954-3899/31/7/B01](#).
36. H. Alharazin, B. D. Sun, E. Epelbaum, J. Gegelia, U. G. Meißner, Gravitational  $p \rightarrow \Delta^+$  transition form factors in chiral perturbation theory, *JHEP* 03 (2024) 007. [arXiv:2312.05193](#), [doi:10.1007/JHEP03\(2024\)007](#).
37. H. Alharazin, Gravitational form factors of the nucleon and one pion graviproduction in chiral EFT, *Phys. Rev. D* 109 (1) (2024) 016009. [arXiv:2312.09675](#), [doi:10.1103/PhysRevD.109.016009](#).

38. K. A. Mamo, I. Zahed, Quark and gluon GPDs at finite skewness from strings in holographic QCD: Evolved and compared with experiment, *Phys. Rev. D* 108 (8) (2023) 086026. [arXiv:2206.03813](#), [doi:10.1103/PhysRevD.108.086026](#).
39. C. Alexandrou, K. Cichy, M. Constantinou, K. Hadjiyiannakou, K. Jansen, A. Scapellato, F. Steffens, Unpolarized and helicity generalized parton distributions of the proton within lattice QCD, *Phys. Rev. Lett.* 125 (26) (2020) 262001. [arXiv:2008.10573](#), [doi:10.1103/PhysRevLett.125.262001](#).
40. S. Bhattacharya, K. Cichy, M. Constantinou, J. Dodson, X. Gao, A. Metz, S. Mukherjee, A. Scapellato, F. Steffens, Y. Zhao, Generalized parton distributions from lattice QCD with asymmetric momentum transfer: Unpolarized quarks, *Phys. Rev. D* 106 (11) (2022) 114512. [arXiv:2209.05373](#), [doi:10.1103/PhysRevD.106.114512](#).
41. S. Bhattacharya, et al., Generalized parton distributions from lattice QCD with asymmetric momentum transfer: Axial-vector case, *Phys. Rev. D* 109 (3) (2024) 034508. [arXiv:2310.13114](#), [doi:10.1103/PhysRevD.109.034508](#).
42. R. G. Edwards, J. J. Dudek, D. G. Richards, S. J. Wallace, Excited state baryon spectroscopy from lattice QCD, *Phys. Rev. D* 84 (2011) 074508. [arXiv:1104.5152](#), [doi:10.1103/PhysRevD.84.074508](#).
43. M. Sun, et al., Roper State from Overlap Fermions, *Phys. Rev. D* 101 (5) (2020) 054511. [arXiv:1911.02635](#), [doi:10.1103/PhysRevD.101.054511](#).
44. K. M. Semenov-Tian-Shansky, M. Vanderhaeghen, Deeply virtual Compton process  $e^-N \rightarrow e^- \gamma \pi N$  to study nucleon to resonance transitions, *Phys. Rev. D* 108 (3) (2023) 034021. [arXiv:2303.00119](#), [doi:10.1103/PhysRevD.108.034021](#).
45. A. Accardi, et al., Strong Interaction Physics at the Luminosity Frontier with 22 GeV Electrons at Jefferson Lab (6 2023). [arXiv:2306.09360](#).
46. A. J. Baltz, The Physics of Ultrapерipheral Collisions at the LHC, *Phys. Rept.* 458 (2008) 1–171. [arXiv:0706.3356](#), [doi:10.1016/j.physrep.2007.12.001](#).
47. B. B. Abelev, et al., Exclusive  $J/\psi$  photoproduction off protons in ultra-peripheral p-Pb collisions at  $\sqrt{s_{NN}} = 5.02$  TeV, *Phys. Rev. Lett.* 113 (23) (2014) 232504. [arXiv:1406.7819](#), [doi:10.1103/PhysRevLett.113.232504](#).
48. S. Acharya, et al., Energy dependence of exclusive  $J/\psi$  photoproduction off protons in ultra-peripheral p-Pb collisions at  $\sqrt{s_{NN}} = 5.02$  TeV, *Eur. Phys. J. C* 79 (5) (2019) 402. [arXiv:1809.03235](#), [doi:10.1140/epjc/s10052-019-6816-2](#).
49. L. Frankfurt, M. Strikman, D. Treleani, C. Weiss, Evidence for color fluctuations in the nucleon in high-energy scattering, *Phys. Rev. Lett.* 101 (2008) 202003. [arXiv:0808.0182](#), [doi:10.1103/PhysRevLett.101.202003](#).
50. E. R. Berger, M. Diehl, B. Pire, Probing generalized parton distributions in  $\pi N \rightarrow \ell^+ \ell^- N$ , *Phys. Lett. B* 523 (2001) 265–272. [arXiv:hep-ph/0110080](#), [doi:10.1016/S0370-2693\(01\)01345-4](#).
51. T. Sawada, W.-C. Chang, S. Kumano, J.-C. Peng, S. Sawada, K. Tanaka, Accessing proton generalized parton distributions and pion distribution amplitudes with the exclusive pion-induced Drell-Yan process at J-PARC, *Phys. Rev. D* 93 (11) (2016) 114034. [arXiv:1605.00364](#), [doi:10.1103/PhysRevD.93.114034](#).
52. S. Kumano, M. Strikman, K. Sudoh, Novel two-to-three hard hadronic processes and possible studies of generalized parton distributions at hadron facilities, *Phys. Rev. D* 80 (2009) 074003. [doi:10.1103/PhysRevD.80.074003](#).
53. X.-D. Ji, Gauge-Invariant Decomposition of Nucleon Spin, *Phys. Rev. Lett.* 78 (1997) 610–613. [arXiv:hep-ph/9603249](#), [doi:10.1103/PhysRevLett.78.610](#).
54. A. V. Radyushkin, Scaling limit of deeply virtual Compton scattering, *Phys. Lett. B* 380 (1996) 417–425. [arXiv:hep-ph/9604317](#), [doi:10.1016/0370-2693\(96\)00528-X](#).
55. J. C. Collins, L. Frankfurt, M. Strikman, Factorization for hard exclusive electroproduction of mesons in QCD, *Phys. Rev. D* 56 (1997) 2982–3006. [arXiv:hep-ph/9611433](#), [doi:10.1103/PhysRevD.56.2982](#).
56. M. Diehl, Generalized parton distributions with helicity flip, *Eur. Phys. J. C* 19 (2001) 485–492. [arXiv:hep-ph/0101335](#), [doi:10.1007/s100520100635](#).
57. R. Dupre, M. Guidal, M. Vanderhaeghen, Tomographic image of the proton, *Phys. Rev. D* 95 (1) (2017) 011501. [arXiv:1606.07821](#), [doi:10.1103/PhysRevD.95.011501](#).
58. M. V. Polyakov,  $N \rightarrow \Delta$  and  $N \rightarrow N\pi$  DVCS and skewed quark distributions, in: 8th International Conference on the Structure of Baryons, 1998, pp. 765–769.

59. M. V. Polyakov, S. Stratmann, Soft Pion Emission in Hard Exclusive Pion Production (9 2006). [arXiv:hep-ph/0609045](#).
60. V. Pascalutsa, M. Vanderhaeghen, S. N. Yang, Electromagnetic excitation of the  $\Delta(1232)$ -resonance, *Phys. Rept.* 437 (2007) 125–232. [arXiv:hep-ph/0609004](#), [doi:10.1016/j.physrep.2006.09.006](#).
61. H. F. Jones, M. D. Scadron, Multipole  $\gamma N - \Delta$  form-factors and resonant photoproduction and electroproduction, *Annals Phys.* 81 (1973) 1–14. [doi:10.1016/0003-4916\(73\)90476-4](#).
62. S. L. Adler, Photoproduction, electroproduction and weak single pion production in the (3,3) resonance region, *Annals Phys.* 50 (1968) 189–311. [doi:10.1016/0003-4916\(68\)90278-9](#).
63. S. L. Adler, Application of current-algebra techniques to soft pion production by the weak neutral current:  $V, A$  Case, *Phys. Rev. D* 12 (1975) 2644. [doi:10.1103/PhysRevD.12.2644](#).
64. L. Tiator, D. Drechsel, S. S. Kamalov, M. Vanderhaeghen, Electromagnetic Excitation of Nucleon Resonances, *Eur. Phys. J. ST* 198 (2011) 141–170. [arXiv:1109.6745](#), [doi:10.1140/epjst/e2011-01488-9](#).
65. L. Tiator, M. Vanderhaeghen, Empirical transverse charge densities in the nucleon-to- $P_{11}(1440)$  transition, *Phys. Lett. B* 672 (2009) 344–348. [arXiv:0811.2285](#), [doi:10.1016/j.physletb.2009.01.048](#).
66. V. D. Burkert, C. D. Roberts, Colloquium : Roper resonance: Toward a solution to the fifty year puzzle, *Rev. Mod. Phys.* 91 (1) (2019) 011003. [arXiv:1710.02549](#), [doi:10.1103/RevModPhys.91.011003](#).
67. K. Kumerički, D. Mueller, Deeply virtual Compton scattering at small  $x_B$  and the access to the GPD H, *Nucl. Phys. B* 841 (2010) 1–58. [arXiv:0904.0458](#), [doi:10.1016/j.nuclphysb.2010.07.015](#).
68. M. Strikman, C. Weiss, Chiral dynamics and the growth of the nucleon’s gluonic transverse size at small x, *Phys. Rev. D* 69 (2004) 054012. [arXiv:hep-ph/0308191](#), [doi:10.1103/PhysRevD.69.054012](#).
69. M. Burkardt, Transverse deformation of parton distributions and transversity decomposition of angular momentum, *Phys. Rev. D* 72 (2005) 094020. [arXiv:hep-ph/0505189](#), [doi:10.1103/PhysRevD.72.094020](#).
70. J.-Y. Kim, Quark distribution functions and spin-flavor structures in  $N \rightarrow \Delta$  transitions, *Phys. Rev. D* 108 (3) (2023) 034024. [arXiv:2305.12714](#), [doi:10.1103/PhysRevD.108.034024](#).
71. G. A. Miller, Charge Density of the Neutron, *Phys. Rev. Lett.* 99 (2007) 112001. [arXiv:0705.2409](#), [doi:10.1103/PhysRevLett.99.112001](#).
72. G. A. Miller, Transverse Charge Densities, *Ann. Rev. Nucl. Part. Sci.* 60 (2010) 1–25. [arXiv:1002.0355](#), [doi:10.1146/annurev.nucl.012809.104508](#).
73. S. Venkat, J. Arrington, G. A. Miller, X. Zhan, Realistic Transverse Images of the Proton Charge and Magnetic Densities, *Phys. Rev. C* 83 (2011) 015203. [arXiv:1010.3629](#), [doi:10.1103/PhysRevC.83.015203](#).
74. G. A. Miller, M. Strikman, C. Weiss, Realizing vector meson dominance with transverse charge densities, *Phys. Rev. C* 84 (2011) 045205. [arXiv:1105.6364](#), [doi:10.1103/PhysRevC.84.045205](#).
75. C. Granados, C. Weiss, Chiral dynamics and peripheral transverse densities, *JHEP* 01 (2014) 092. [arXiv:1308.1634](#), [doi:10.1007/JHEP01\(2014\)092](#).
76. J. M. Alarcón, C. Weiss, Transverse charge and current densities in the nucleon from dispersively improved chiral effective field theory, *Phys. Rev. D* 106 (5) (2022) 054005. [arXiv:2204.11863](#), [doi:10.1103/PhysRevD.106.054005](#).
77. Y.-F. Wang, M. Döring, J. Hergenrather, M. Mai, T. Mart, U.-G. Meißner, D. Rönchen, R. Workman, Global data-driven determination of baryon transition form factors (4 2024). [arXiv:2404.17444](#).
78. C. E. Carlson, M. Vanderhaeghen, Empirical transverse charge densities in the nucleon and the nucleon-to- $\Delta$  transition, *Phys. Rev. Lett.* 100 (2008) 032004. [arXiv:0710.0835](#), [doi:10.1103/PhysRevLett.100.032004](#).
79. D. Chakrabarti, C. Mondal, Nucleon to  $\Delta$  transition form factors and empirical transverse charge densities, *Eur. Phys. J. A* 52 (9) (2016) 285. [arXiv:1605.00997](#), [doi:10.1140/epja/i2016-16285-8](#).
80. J. M. Alarcón, A. N. Hiller Blin, M. J. Vicente Vacas, C. Weiss, Peripheral transverse densities of the baryon octet from chiral effective field theory and dispersion analysis, *Nucl. Phys. A* 964 (2017) 18–54. [arXiv:1703.04534](#), [doi:10.1016/j.nuclphysa.2017.05.002](#).
81. E. Leader, C. Lorcé, The angular momentum controversy: What’s it all about and does it matter?, *Phys. Rept.* 541 (3) (2014) 163–248. [arXiv:1309.4235](#), [doi:10.1016/j.physrep.2014.02.010](#).
82. C. Granados, C. Weiss, Partonic angular momentum in the nucleon’s chiral periphery, *Phys. Lett.*

- B 797 (2019) 134847. [arXiv:1905.02742](#), [doi:10.1016/j.physletb.2019.134847](#).
83. M. Gockeler, R. Horsley, D. Pleiter, P. E. L. Rakow, A. Schafer, G. Schierholz, W. Schroers, Generalized parton distributions from lattice QCD, *Phys. Rev. Lett.* 92 (2004) 042002. [arXiv:hep-ph/0304249](#), [doi:10.1103/PhysRevLett.92.042002](#).
  84. P. Hagler, et al., Nucleon Generalized Parton Distributions from Full Lattice QCD, *Phys. Rev. D* 77 (2008) 094502. [arXiv:0705.4295](#), [doi:10.1103/PhysRevD.77.094502](#).
  85. J. D. Bratt, et al., Nucleon structure from mixed action calculations using 2+1 flavors of asqtad sea and domain wall valence fermions, *Phys. Rev. D* 82 (2010) 094502. [arXiv:1001.3620](#), [doi:10.1103/PhysRevD.82.094502](#).
  86. G. S. Bali, S. Collins, M. Göckeler, R. Rödl, A. Schäfer, A. Sternbeck, Nucleon generalized form factors from two-flavor lattice QCD, *Phys. Rev. D* 100 (1) (2019) 014507. [arXiv:1812.08256](#), [doi:10.1103/PhysRevD.100.014507](#).
  87. C. Alexandrou, et al., Moments of nucleon generalized parton distributions from lattice QCD simulations at physical pion mass, *Phys. Rev. D* 101 (3) (2020) 034519. [arXiv:1908.10706](#), [doi:10.1103/PhysRevD.101.034519](#).
  88. M. V. Polyakov, Generalized parton distributions and strong forces inside nucleons and nuclei, *Phys. Lett. B* 555 (2003) 57–62. [arXiv:hep-ph/0210165](#), [doi:10.1016/S0370-2693\(03\)00036-4](#).
  89. L. Adhikari, M. Burkardt, Angular Momentum Distribution in the Transverse Plane, *Phys. Rev. D* 94 (11) (2016) 114021. [arXiv:1609.07099](#), [doi:10.1103/PhysRevD.94.114021](#).
  90. C. Lorcé, L. Mantovani, B. Pasquini, Spatial distribution of angular momentum inside the nucleon, *Phys. Lett. B* 776 (2018) 38–47. [arXiv:1704.08557](#), [doi:10.1016/j.physletb.2017.11.018](#).
  91. V. D. Burkert, L. Elouadrhiri, F. X. Girod, C. Lorcé, P. Schweitzer, P. E. Shanahan, Colloquium: Gravitational form factors of the proton, *Rev. Mod. Phys.* 95 (4) (2023) 041002. [arXiv:2303.08347](#), [doi:10.1103/RevModPhys.95.041002](#).
  92. M. V. Polyakov, C. Weiss, Skewed and double distributions in pion and nucleon, *Phys. Rev. D* 60 (1999) 114017. [arXiv:hep-ph/9902451](#), [doi:10.1103/PhysRevD.60.114017](#).
  93. V. D. Burkert, L. Elouadrhiri, F. X. Girod, The pressure distribution inside the proton, *Nature* 557 (7705) (2018) 396–399. [doi:10.1038/s41586-018-0060-z](#).
  94. K. Kumericki, Measurability of pressure inside the proton, *Nature* 570 (E1-E2) (2019) 7759. [doi:10.1038/s41586-019-1211-6](#).
  95. H. Moutarde, P. Sznajder, J. Wagner, Unbiased determination of DVCS Compton Form Factors, *Eur. Phys. J. C* 79 (7) (2019) 614. [arXiv:1905.02089](#), [doi:10.1140/epjc/s10052-019-7117-5](#).
  96. M. Burkardt, Transversity decomposition of quark angular momentum, *Phys. Lett. B* 639 (2006) 462–464. [doi:10.1016/j.physletb.2006.01.076](#).
  97. S. Ahmad, G. R. Goldstein, S. Liuti, Nucleon Tensor Charge from Exclusive  $\pi^0$  Electroproduction, *Phys. Rev. D* 79 (2009) 054014. [arXiv:0805.3568](#), [doi:10.1103/PhysRevD.79.054014](#).
  98. N. Kivel, M. V. Polyakov, S. Stratmann, Soft pion emission from the nucleon induced by twist-2 light-cone operators (7 2004). [arXiv:nucl-th/0407052](#).
  99. G. 't Hooft, A Planar Diagram Theory for Strong Interactions, *Nucl. Phys. B* 72 (1974) 461. [doi:10.1016/0550-3213\(74\)90154-0](#).
  100. E. Witten, Baryons in the  $1/N$  Expansion, *Nucl. Phys. B* 160 (1979) 57–115. [doi:10.1016/0550-3213\(79\)90232-3](#).
  101. R. F. Dashen, E. E. Jenkins, A. V. Manohar, The  $1/N_c$  expansion for baryons, *Phys. Rev. D* 49 (1994) 4713, [Erratum: *Phys. Rev. D* 51, 2489 (1995)]. [arXiv:hep-ph/9310379](#), [doi:10.1103/PhysRevD.51.2489](#).
  102. R. F. Dashen, E. E. Jenkins, A. V. Manohar, Spin flavor structure of large  $N_c$  baryons, *Phys. Rev. D* 51 (1995) 3697–3727. [arXiv:hep-ph/9411234](#), [doi:10.1103/PhysRevD.51.3697](#).
  103. E. E. Jenkins, Large  $N_c$  baryons, *Ann. Rev. Nucl. Part. Sci.* 48 (1998) 81–119. [arXiv:hep-ph/9803349](#), [doi:10.1146/annurev.nucl.48.1.81](#).
  104. A. J. Buchmann, J. A. Hester, R. F. Lebed, Quadrupole moments of  $N$  and  $\Delta$  in the  $1/N_c$  expansion, *Phys. Rev. D* 66 (2002) 056002. [arXiv:hep-ph/0205108](#), [doi:10.1103/PhysRevD.66.056002](#).
  105. E. E. Jenkins, X.-d. Ji, A. V. Manohar,  $\Delta \rightarrow N\gamma$  in large  $N_c$  QCD, *Phys. Rev. Lett.* 89 (2002) 242001. [arXiv:hep-ph/0207092](#), [doi:10.1103/PhysRevLett.89.242001](#).
  106. V. Pascalutsa, M. Vanderhaeghen, Large- $N_c$  relations for the electromagnetic  $N$  to  $\Delta(1232)$  transition, *Phys. Rev. D* 76 (2007) 111501. [arXiv:0711.0147](#), [doi:10.1103/PhysRevD.76.111501](#).
  107. L. L. Frankfurt, M. V. Polyakov, M. Strikman, M. Vanderhaeghen, Hard exclusive elec-

- troproduction of decuplet baryons in the large  $N_c$  limit, *Phys. Rev. Lett.* 84 (2000) 2589–2592. [arXiv:hep-ph/9911381](#), [doi:10.1103/PhysRevLett.84.2589](#).
108. A. Calle Cordon, J. L. Goity, Baryon Masses and Axial Couplings in the Combined  $1/N_c$  and Chiral Expansions, *Phys. Rev. D* 87 (1) (2013) 016019. [arXiv:1210.2364](#), [doi:10.1103/PhysRevD.87.016019](#).
109. I. P. Fernando, J. L. Goity, SU(3) vector currents in baryon chiral perturbation theory combined with the  $1/N_c$  expansion, *Phys. Rev. D* 101 (5) (2020) 054026. [arXiv:1911.00987](#), [doi:10.1103/PhysRevD.101.054026](#).
110. D. Diakonov, V. Y. Petrov, P. V. Pobylitsa, A Chiral Theory of Nucleons, *Nucl. Phys. B* 306 (1988) 809. [doi:10.1016/0550-3213\(88\)90443-9](#).
111. V. Y. Petrov, P. V. Pobylitsa, M. V. Polyakov, I. Bornig, K. Goeke, C. Weiss, Off - forward quark distributions of the nucleon in the large  $N_c$  limit, *Phys. Rev. D* 57 (1998) 4325–4333. [arXiv:hep-ph/9710270](#), [doi:10.1103/PhysRevD.57.4325](#).
112. I. I. Balitsky, V. M. Braun, A. V. Kolesnichenko, Radiative Decay  $\Sigma^+ \rightarrow p\gamma$  in Quantum Chromodynamics, *Nucl. Phys. B* 312 (1989) 509–550. [doi:10.1016/0550-3213\(89\)90570-1](#).
113. A. Khodjamirian, B. Melić, Y.-M. Wang, A guide to the QCD light-cone sum rules for  $b$ -quark decays, *Eur. Phys. J. ST* 233 (2) (2024) 271–298. [arXiv:2311.08700](#), [doi:10.1140/epjs/s11734-023-01046-6](#).
114. V. M. Braun, A. Lenz, G. Peters, A. V. Radyushkin, Light cone sum rules for  $\gamma^*N \rightarrow \Delta$  transition form-factors, *Phys. Rev. D* 73 (2006) 034020. [arXiv:hep-ph/0510237](#), [doi:10.1103/PhysRevD.73.034020](#).
115. V. M. Braun, A. Lenz, M. Wittmann, Nucleon Form Factors in QCD, *Phys. Rev. D* 73 (2006) 094019. [arXiv:hep-ph/0604050](#), [doi:10.1103/PhysRevD.73.094019](#).
116. I. V. Anikin, V. M. Braun, N. Offen, Nucleon Form Factors and Distribution Amplitudes in QCD, *Phys. Rev. D* 88 (2013) 114021. [arXiv:1310.1375](#), [doi:10.1103/PhysRevD.88.114021](#).
117. I. V. Anikin, V. M. Braun, N. Offen, Electroproduction of the  $N^*(1535)$  nucleon resonance in QCD, *Phys. Rev. D* 92 (1) (2015) 014018. [arXiv:1505.05759](#), [doi:10.1103/PhysRevD.92.014018](#).
118. I. V. Anikin, V. M. Braun, N. Offen, Axial form factor of the nucleon at large momentum transfers, *Phys. Rev. D* 94 (3) (2016) 034011. [arXiv:1607.01504](#), [doi:10.1103/PhysRevD.94.034011](#).
119. V. M. Braun, D. Y. Ivanov, A. Peters, Threshold pion electroproduction at large momentum transfers, *Phys. Rev. D* 77 (2008) 034016. [arXiv:0710.3265](#), [doi:10.1103/PhysRevD.77.034016](#).
120. G. S. Bali, et al., Light-cone distribution amplitudes of octet baryons from lattice QCD, *Eur. Phys. J. A* 55 (7) (2019) 116. [arXiv:1903.12590](#), [doi:10.1140/epja/i2019-12803-6](#).
121. K.-F. Liu, S.-J. Dong, Origin of difference between anti-d and anti-u partons in the nucleon, *Phys. Rev. Lett.* 72 (1994) 1790–1793. [arXiv:hep-ph/9306299](#), [doi:10.1103/PhysRevLett.72.1790](#).
122. X. Ji, Parton Physics on a Euclidean Lattice, *Phys. Rev. Lett.* 110 (2013) 262002. [arXiv:1305.1539](#), [doi:10.1103/PhysRevLett.110.262002](#).
123. X. Ji, Parton Physics from Large-Momentum Effective Field Theory, *Sci. China Phys. Mech. Astron.* 57 (2014) 1407–1412. [arXiv:1404.6680](#), [doi:10.1007/s11433-014-5492-3](#).
124. W. Detmold, C. J. D. Lin, Deep-inelastic scattering and the operator product expansion in lattice QCD, *Phys. Rev. D* 73 (2006) 014501. [arXiv:hep-lat/0507007](#), [doi:10.1103/PhysRevD.73.014501](#).
125. V. Braun, D. Müller, Exclusive processes in position space and the pion distribution amplitude, *Eur. Phys. J. C* 55 (2008) 349–361. [arXiv:0709.1348](#), [doi:10.1140/epjc/s10052-008-0608-4](#).
126. A. V. Radyushkin, Quasi-parton distribution functions, momentum distributions, and pseudo-parton distribution functions, *Phys. Rev. D* 96 (3) (2017) 034025. [arXiv:1705.01488](#), [doi:10.1103/PhysRevD.96.034025](#).
127. K. Orginos, A. Radyushkin, J. Karpie, S. Zafeiropoulos, Lattice QCD exploration of parton pseudo-distribution functions, *Phys. Rev. D* 96 (9) (2017) 094503. [arXiv:1706.05373](#), [doi:10.1103/PhysRevD.96.094503](#).
128. A. J. Chambers, R. Horsley, Y. Nakamura, H. Perlt, P. E. L. Rakow, G. Schierholz, A. Schiller, K. Somfleth, R. D. Young, J. M. Zanotti, Nucleon Structure Functions from Operator Product Expansion on the Lattice, *Phys. Rev. Lett.* 118 (24) (2017) 242001. [arXiv:1703.01153](#), [doi:10.1103/PhysRevLett.118.242001](#).
129. Y.-Q. Ma, J.-W. Qiu, Exploring Partonic Structure of Hadrons Using ab initio Lattice QCD Calculations, *Phys. Rev. Lett.* 120 (2) (2018) 022003. [arXiv:1709.03018](#), [doi:10.1103/PhysRevLett.120.022003](#).
130. H.-W. Lin, Nucleon Tomography and Generalized Parton Distribution at Physical Pion Mass

- from Lattice QCD, Phys. Rev. Lett. 127 (18) (2021) 182001. [arXiv:2008.12474](#), [doi:10.1103/PhysRevLett.127.182001](#).
131. C. Alexandrou, K. Cichy, M. Constantinou, K. Hadjiyiannakou, K. Jansen, A. Scapellato, F. Steffens, Transversity GPDs of the proton from lattice QCD, Phys. Rev. D 105 (3) (2022) 034501. [arXiv:2108.10789](#), [doi:10.1103/PhysRevD.105.034501](#).
132. A. Hannaford-Gunn, K. U. Can, R. Horsley, Y. Nakamura, H. Perlt, P. E. L. Rakow, H. Stüben, G. Schierholz, R. D. Young, J. M. Zanotti, Generalized parton distributions from the off-forward Compton amplitude in lattice QCD, Phys. Rev. D 105 (1) (2022) 014502. [arXiv:2110.11532](#), [doi:10.1103/PhysRevD.105.014502](#).
133. H.-W. Lin, Nucleon helicity generalized parton distribution at physical pion mass from lattice QCD, Phys. Lett. B 824 (2022) 136821. [arXiv:2112.07519](#), [doi:10.1016/j.physletb.2021.136821](#).
134. S. Bhattacharya, K. Cichy, M. Constantinou, X. Gao, A. Metz, J. Miller, S. Mukherjee, P. Petreczky, F. Steffens, Y. Zhao, Moments of proton GPDs from the OPE of nonlocal quark bilinears up to NNLO, Phys. Rev. D 108 (1) (2023) 014507. [arXiv:2305.11117](#), [doi:10.1103/PhysRevD.108.014507](#).
135. S. Bhattacharya, K. Cichy, M. Constantinou, J. Dodson, A. Metz, A. Scapellato, F. Steffens, Chiral-even axial twist-3 GPDs of the proton from lattice QCD, Phys. Rev. D 108 (5) (2023) 054501. [arXiv:2306.05533](#), [doi:10.1103/PhysRevD.108.054501](#).
136. K. Cichy, M. Constantinou, A guide to light-cone PDFs from Lattice QCD: an overview of approaches, techniques and results, Adv. High Energy Phys. 2019 (2019) 3036904. [arXiv:1811.07248](#), [doi:10.1155/2019/3036904](#).
137. X. Ji, Y.-S. Liu, Y. Liu, J.-H. Zhang, Y. Zhao, Large-momentum effective theory, Rev. Mod. Phys. 93 (3) (2021) 035005. [arXiv:2004.03543](#), [doi:10.1103/RevModPhys.93.035005](#).
138. M. Constantinou, The  $x$ -dependence of hadronic parton distributions: A review on the progress of lattice QCD, Eur. Phys. J. A 57 (2) (2021) 77. [arXiv:2010.02445](#), [doi:10.1140/epja/s10050-021-00353-7](#).
139. K. Cichy, Progress in  $x$ -dependent partonic distributions from lattice QCD, PoS LATTICE2021 (2022) 017. [arXiv:2110.07440](#), [doi:10.22323/1.396.0017](#).
140. D. B. Leinweber, T. Draper, R. M. Woloshyn, Baryon octet to decuplet electromagnetic transitions, Phys. Rev. D 48 (1993) 2230–2249. [arXiv:hep-lat/9212016](#), [doi:10.1103/PhysRevD.48.2230](#).
141. C. Alexandrou, G. Koutsou, J. W. Negele, Y. Proestos, A. Tsapalis, Nucleon to  $\Delta$  transition form factors with  $N_F = 2 + 1$  domain wall fermions, Phys. Rev. D 83 (2011) 014501. [arXiv:1011.3233](#), [doi:10.1103/PhysRevD.83.014501](#).
142. C. Alexandrou, L. Leskovec, S. Meinel, J. Negele, S. Paul, M. Petschlies, A. Pochinsky, G. Rendon, S. Syritsyn,  $\pi\gamma \rightarrow \pi\pi$  transition and the  $\rho$  radiative decay width from lattice QCD, Phys. Rev. D 98 (7) (2018) 074502, [Erratum: Phys.Rev.D 105, 019902 (2022)]. [arXiv:1807.08357](#), [doi:10.1103/PhysRevD.98.074502](#).
143. C. Alexandrou, et al., Pion transition form factor from twisted-mass lattice QCD and the hadronic light-by-light  $\pi^0$ -pole contribution to the muon  $g - 2$ , Phys. Rev. D 108 (9) (2023) 094514. [arXiv:2308.12458](#), [doi:10.1103/PhysRevD.108.094514](#).
144. M. Guidal, S. Bouchigny, J. P. Didelez, C. Hadjiidakis, E. Hourany, M. Vanderhaeghen, Generalized parton distributions and nucleon resonances, Nucl. Phys. A 721 (2003) 327–332. [arXiv:hep-ph/0304252](#), [doi:10.1016/S0375-9474\(03\)01061-3](#).
145. X.-D. Ji, J. Osborne, One loop corrections and all order factorization in deeply virtual Compton scattering, Phys. Rev. D 58 (1998) 094018. [arXiv:hep-ph/9801260](#), [doi:10.1103/PhysRevD.58.094018](#).
146. J. C. Collins, A. Freund, Proof of factorization for deeply virtual Compton scattering in QCD, Phys. Rev. D 59 (1999) 074009. [arXiv:hep-ph/9801262](#), [doi:10.1103/PhysRevD.59.074009](#).
147. D. Drechsel, S. S. Kamalov, L. Tiator, Unitary Isobar Model - MAID2007, Eur. Phys. J. A 34 (2007) 69–97. [arXiv:0710.0306](#), [doi:10.1140/epja/i2007-10490-6](#).
148. V. M. Braun, A. N. Manashov, D. Müller, B. M. Pirnay, Deeply Virtual Compton Scattering to the twist-four accuracy: Impact of finite- $t$  and target mass corrections, Phys. Rev. D 89 (7) (2014) 074022. [arXiv:1401.7621](#), [doi:10.1103/PhysRevD.89.074022](#).
149. L. L. Frankfurt, P. V. Pobylitsa, M. V. Polyakov, M. Strikman, Hard exclusive pseudoscalar meson electroproduction and spin structure of a nucleon, Phys. Rev. D 60 (1999) 014010. [arXiv:hep-ph/9901429](#), [doi:10.1103/PhysRevD.60.014010](#).

150. P. Kroll, Hard exclusive processes involving kaons, *Eur. Phys. J. A* 55 (5) (2019) 76. [arXiv:1901.11380](#), [doi:10.1140/epja/i2019-12747-9](#).
151. T. Arens, O. Nachtmann, M. Diehl, P. V. Landshoff, Some tests for the helicity structure of the pomeron in e p collisions, *Z. Phys. C* 74 (1997) 651–669. [arXiv:hep-ph/9605376](#), [doi:10.1007/s002880050430](#).
152. S. V. Goloskokov, P. Kroll, An Attempt to understand exclusive  $\pi^+$  electroproduction, *Eur. Phys. J. C* 65 (2010) 137–151. [arXiv:0906.0460](#), [doi:10.1140/epjc/s10052-009-1178-9](#).
153. S. V. Goloskokov, P. Kroll, The Role of the quark and gluon GPDs in hard vector-meson electroproduction, *Eur. Phys. J. C* 53 (2008) 367–384. [arXiv:0708.3569](#), [doi:10.1140/epjc/s10052-007-0466-5](#).
154. S. V. Goloskokov, P. Kroll, Transversity in hard exclusive electroproduction of pseudoscalar mesons, *Eur. Phys. J. A* 47 (2011) 112. [arXiv:1106.4897](#), [doi:10.1140/epja/i2011-11112-6](#).
155. N. M. Kroll, M. A. Ruderman, A Theorem on photomeson production near threshold and the suppression of pairs in pseudoscalar meson theory, *Phys. Rev.* 93 (1954) 233–238. [doi:10.1103/PhysRev.93.233](#).
156. Y. Nambu, D. Lurie, Chirality conservation and soft pion production, *Phys. Rev.* 125 (1962) 1429–1436. [doi:10.1103/PhysRev.125.1429](#).
157. Y. Nambu, E. Shrauner, Soft pion emission induced by electromagnetic and weak interactions, *Phys. Rev.* 128 (1962) 862–868. [doi:10.1103/PhysRev.128.862](#).
158. V. Bernard, N. Kaiser, U. G. Meissner, Measuring the axial radius of the nucleon in pion electroproduction, *Phys. Rev. Lett.* 69 (1992) 1877–1879. [doi:10.1103/PhysRevLett.69.1877](#).
159. V. Bernard, N. Kaiser, U.-G. Meissner, Chiral dynamics in nucleons and nuclei, *Int. J. Mod. Phys. E* 4 (1995) 193–346. [arXiv:hep-ph/9501384](#), [doi:10.1142/S0218301395000092](#).
160. A. I. Vainshtein, V. I. Zakharov, Low-energy theorems for photoproduction and electropion production at threshold, *Nucl. Phys. B* 36 (1972) 589–604. [doi:10.1016/0550-3213\(72\)90238-6](#).
161. V. M. Braun, D. Y. Ivanov, A. Lenz, A. Peters, Deep inelastic pion electroproduction at threshold, *Phys. Rev. D* 75 (2007) 014021. [arXiv:hep-ph/0611386](#), [doi:10.1103/PhysRevD.75.014021](#).
162. K. Park, et al., Measurement of the generalized form factors near threshold via  $\gamma^*p \rightarrow n\pi^+$  at high  $Q^2$ , *Phys. Rev. C* 85 (2012) 035208. [arXiv:1201.0903](#), [doi:10.1103/PhysRevC.85.035208](#).
163. P. Khetarpal, et al., Near Threshold Neutral Pion Electroproduction at High Momentum Transfers and Generalized Form Factors, *Phys. Rev. C* 87 (4) (2013) 045205. [arXiv:1211.6460](#), [doi:10.1103/PhysRevC.87.045205](#).
164. S. Diehl, et al., A multidimensional study of the structure function ratio  $\sigma_{LT'}/\sigma_0$  from hard exclusive  $\pi^+$  electro-production off protons in the GPD regime, *Phys. Lett. B* 839 (2023) 137761. [arXiv:2210.14557](#), [doi:10.1016/j.physletb.2023.137761](#).
165. A. Kim, et al., Beam spin asymmetry measurements of deeply virtual  $\pi^0$  production with CLAS12, *Phys. Lett. B* 849 (2024) 138459. [arXiv:2307.07874](#), [doi:10.1016/j.physletb.2024.138459](#).
166. H. Blok, T. Horn, G. Huber, E. Beise, D. Gaskell, D. Mack, V. Tadevosyan, J. Volmer, D. Abbott, K. Aniol, et al., Charged pion form factor between  $Q^2 = 0.60$  and  $2.45$  GeV<sup>2</sup>. I. Measurements of the cross section for the  $^1\text{H}(e, e' \pi^+)n$  reaction, *Physical Review C* 78 (4) (2008) 045202. [doi:10.1103/PhysRevC.78.045202](#).
167. P. Bosted, T. Horn, G. Huber, P. Markowitz, et al., Proposal to Jefferson Lab PAC 34: Studies of the L-T Separated Kaon Electroproduction Cross Section from 5-11 GeV (2008), url: [https://www.jlab.org/exp\\_prog/proposals/09/PR12-09-011.pdf](https://www.jlab.org/exp_prog/proposals/09/PR12-09-011.pdf).
168. B. Moreno, PhD thesis Universite Paris-sud XI (2009), url: [https://www.jlab.org/Hall-B/general/thesis/Moreno\\_thesis.pdf](https://www.jlab.org/Hall-B/general/thesis/Moreno_thesis.pdf).
169. P. Chatagnon, et al., First Measurement of Timelike Compton Scattering, *Phys. Rev. Lett.* 127 (26) (2021) 262501. [arXiv:2108.11746](#), [doi:10.1103/PhysRevLett.127.262501](#).
170. K. Tanaka, Exclusive pion-induced Drell-Yan process at J-PARC for accessing the nucleon GPDs and soft nonfactorizable mechanism, *PoS DIS2017* (2018) 249. [arXiv:1709.01063](#), [doi:10.22323/1.297.0249](#).
171. S. V. Goloskokov, P. Kroll, The exclusive limit of the pion-induced Drell-Yan process, *Phys. Lett. B* 748 (2015) 323–327. [arXiv:1506.04619](#), [doi:10.1016/j.physletb.2015.07.016](#).
172. B. Pire, K. Semenov-Tian-Shansky, L. Szymanowski, Transition distribution amplitudes and hard exclusive reactions with baryon number transfer, *Phys. Rept.* 940 (2021) 1–121. [arXiv:2103.01079](#), [doi:10.1016/j.physrep.2021.09.002](#).

173. B. Pire, K. Semenov-Tian-Shansky, L. Szymanowski, Backward charmonium production in  $\pi N$  collisions, *Phys. Rev. D* 95 (3) (2017) 034021. [doi:10.1103/PhysRevD.95.034021](https://doi.org/10.1103/PhysRevD.95.034021).
174. H. Noumi, Hadron Experimental Facility at J-PARC, *Few Body Syst.* 54 (7-10) (2013) 813–819. [doi:10.1007/s00601-013-0660-y](https://doi.org/10.1007/s00601-013-0660-y).
175. K. Shirotori, et al., Charmed Baryon Spectroscopy Experiment at J-PARC, *JPS Conf. Proc.* 8 (2015) 022012. [doi:10.7566/JPSCP.8.022012](https://doi.org/10.7566/JPSCP.8.022012).
176. P. Kroll, H. Moutarde, F. Sabatie, From hard exclusive meson electroproduction to deeply virtual Compton scattering, *Eur. Phys. J. C* 73 (1) (2013) 2278. [arXiv:1210.6975](https://arxiv.org/abs/1210.6975), [doi:10.1140/epjc/s10052-013-2278-0](https://doi.org/10.1140/epjc/s10052-013-2278-0).
177. J. C. Collins, L. Frankfurt, M. Strikman, Proof of factorization for exclusive deep-inelastic processes, pp. 296-303, *Low  $x$  Physics*, Proceedings of the Madrid Workshop, Madrid, Spain, June 18- 21, 1997, edited by F. Barreiro, L Labarga, and J. del Peso, World Scientific (1998).
178. J.-W. Qiu, Z. Yu, Exclusive production of a pair of high transverse momentum photons in pion-nucleon collisions for extracting generalized parton distributions, *JHEP* 08 (2022) 103. [doi:10.1007/JHEP08\(2022\)103](https://doi.org/10.1007/JHEP08(2022)103).
179. J.-W. Qiu, Z. Yu, Single diffractive hard exclusive processes for the study of generalized parton distributions, *Phys. Rev. D* 107 (1) (2023) 014007. [doi:10.1103/PhysRevD.107.014007](https://doi.org/10.1103/PhysRevD.107.014007).
180. M. Guidal, M. V. Polyakov, A. V. Radyushkin, M. Vanderhaeghen, Nucleon form-factors from generalized parton distributions, *Phys. Rev. D* 72 (2005) 054013. [arXiv:hep-ph/0410251](https://arxiv.org/abs/hep-ph/0410251), [doi:10.1103/PhysRevD.72.054013](https://doi.org/10.1103/PhysRevD.72.054013).
181. H. Kawamura, S. Kumano, Tomography of exotic hadrons in high-energy exclusive processes, *Phys. Rev. D* 89 (5) (2014) 054007. [arXiv:1312.1596](https://arxiv.org/abs/1312.1596), [doi:10.1103/PhysRevD.89.054007](https://doi.org/10.1103/PhysRevD.89.054007).
182. M. Masuda, et al., Study of  $\pi^0$  pair production in single-tag two-photon collisions, *Phys. Rev. D* 93 (3) (2016) 032003. [arXiv:1508.06757](https://arxiv.org/abs/1508.06757), [doi:10.1103/PhysRevD.93.032003](https://doi.org/10.1103/PhysRevD.93.032003).
183. S. Kumano, Q.-T. Song, O. V. Teryaev, Hadron tomography by generalized distribution amplitudes in pion-pair production process  $\gamma^*\gamma \rightarrow \pi^0\pi^0$  and gravitational form factors for pion, *Phys. Rev. D* 97 (1) (2018) 014020. [arXiv:1711.08088](https://arxiv.org/abs/1711.08088), [doi:10.1103/PhysRevD.97.014020](https://doi.org/10.1103/PhysRevD.97.014020).
184. J. K. Ahn, et al., letter of Intent (2018), 27th J-PARC PAC meeting (2019), url: [https://j-parc.jp/researcher/Hadron/en/pac\\_1901/pdf/LoI\\_2019-07.pdf](https://j-parc.jp/researcher/Hadron/en/pac_1901/pdf/LoI_2019-07.pdf).
185. H. Kawamura, S. Kumano, T. Sekihara, Determination of exotic hadron structure by constituent-counting rule for hard exclusive processes, *Phys. Rev. D* 88 (2013) 034010. [doi:10.1103/PhysRevD.88.034010](https://doi.org/10.1103/PhysRevD.88.034010).
186. W.-C. Chang, S. Kumano, T. Sekihara, Constituent-counting rule in photoproduction of hyperon resonances, *Phys. Rev. D* 93 (3) (2016) 034006. [doi:10.1103/PhysRevD.93.034006](https://doi.org/10.1103/PhysRevD.93.034006).
187. L. Frankfurt, M. Strikman, C. Weiss, Small- $x$  physics: From HERA to LHC and beyond, *Ann. Rev. Nucl. Part. Sci.* 55 (2005) 403–465. [arXiv:hep-ph/0507286](https://arxiv.org/abs/hep-ph/0507286), [doi:10.1146/annurev.nucl.53.041002.110615](https://doi.org/10.1146/annurev.nucl.53.041002.110615).
188. L. Frankfurt, A. Freund, V. Guzey, M. Strikman, Nondiagonal parton distribution in the leading logarithmic approximation, *Phys. Lett. B* 418 (1998) 345–354, [Erratum: *Phys.Lett.B* 429, 414 (1998)]. [arXiv:hep-ph/9703449](https://arxiv.org/abs/hep-ph/9703449), [doi:10.1016/S0370-2693\(97\)01152-0](https://doi.org/10.1016/S0370-2693(97)01152-0).
189. A. G. Shuvaev, K. J. Golec-Biernat, A. D. Martin, M. G. Ryskin, Off diagonal distributions fixed by diagonal partons at small  $x$  and  $\xi$ , *Phys. Rev. D* 60 (1999) 014015. [arXiv:hep-ph/9902410](https://arxiv.org/abs/hep-ph/9902410), [doi:10.1103/PhysRevD.60.014015](https://doi.org/10.1103/PhysRevD.60.014015).
190. M. L. Good, W. D. Walker, Diffraction dissociation of beam particles, *Phys. Rev.* 120 (1960) 1857–1860. [doi:10.1103/PhysRev.120.1857](https://doi.org/10.1103/PhysRev.120.1857).
191. H. I. Miettinen, J. Pumplin, Diffraction Scattering and the Parton Structure of Hadrons, *Phys. Rev. D* 18 (1978) 1696. [doi:10.1103/PhysRevD.18.1696](https://doi.org/10.1103/PhysRevD.18.1696).
192. S. Schlichting, B. Schenke, The shape of the proton at high energies, *Phys. Lett. B* 739 (2014) 313–319. [arXiv:1407.8458](https://arxiv.org/abs/1407.8458), [doi:10.1016/j.physletb.2014.10.068](https://doi.org/10.1016/j.physletb.2014.10.068).
193. H. Mäntysaari, B. Schenke, Evidence of strong proton shape fluctuations from incoherent diffraction, *Phys. Rev. Lett.* 117 (5) (2016) 052301. [arXiv:1603.04349](https://arxiv.org/abs/1603.04349), [doi:10.1103/PhysRevLett.117.052301](https://doi.org/10.1103/PhysRevLett.117.052301).
194. H. Mäntysaari, B. Schenke, Revealing proton shape fluctuations with incoherent diffraction at high energy, *Phys. Rev. D* 94 (3) (2016) 034042. [arXiv:1607.01711](https://arxiv.org/abs/1607.01711), [doi:10.1103/PhysRevD.94.034042](https://doi.org/10.1103/PhysRevD.94.034042).
195. F. D. Aaron, et al., Diffractive Electroproduction of rho and phi Mesons at HERA, *JHEP* 05 (2010) 032. [arXiv:0910.5831](https://arxiv.org/abs/0910.5831), [doi:10.1007/JHEP05\(2010\)032](https://doi.org/10.1007/JHEP05(2010)032).
196. S. Chekanov, et al., Exclusive  $\rho^0$  production in deep inelastic scattering at HERA, *PMC Phys. A* 1 (2007) 6. [arXiv:0708.1478](https://arxiv.org/abs/0708.1478), [doi:10.1186/](https://doi.org/10.1186/)



- 1754-0410-1-6.
197. S. Chekanov, et al., Exclusive electroproduction of  $\phi$  mesons at HERA, Nucl. Phys. B 718 (2005) 3–31. [arXiv:hep-ex/0504010](#), [doi:10.1016/j.nuclphysb.2005.04.009](#).
  198. H. Abramowicz, et al., Exclusive electroproduction of two pions at HERA, Eur. Phys. J. C 72 (2012) 1869. [arXiv:1111.4905](#), [doi:10.1140/epjc/s10052-012-1869-5](#).
  199. S. Aid, et al., Elastic and inelastic photoproduction of  $J/\psi$  mesons at HERA, Nucl. Phys. B 472 (1996) 3–31. [arXiv:hep-ex/9603005](#), [doi:10.1016/0550-3213\(96\)00274-X](#).
  200. C. Adloff, et al., Inelastic photoproduction of  $J/\psi$  mesons at HERA, Eur. Phys. J. C 25 (2002) 25–39. [arXiv:hep-ex/0205064](#), [doi:10.1007/s10052-002-1009-8](#).
  201. A. Aktas, et al., Elastic  $J/\psi$  production at HERA, Eur. Phys. J. C 46 (2006) 585–603. [arXiv:hep-ex/0510016](#), [doi:10.1140/epjc/s2006-02519-5](#).
  202. F. D. Aaron, et al., Inelastic Production of  $J/\psi$  Mesons in Photoproduction and Deep Inelastic Scattering at HERA, Eur. Phys. J. C 68 (2010) 401–420. [arXiv:1002.0234](#), [doi:10.1140/epjc/s10052-010-1376-5](#).
  203. C. Alexa, et al., Elastic and Proton-Dissociative Photoproduction of  $J/\psi$  Mesons at HERA, Eur. Phys. J. C 73 (6) (2013) 2466. [arXiv:1304.5162](#), [doi:10.1140/epjc/s10052-013-2466-y](#).
  204. J. Breitweg, et al., Measurement of inelastic  $J/\psi$  photoproduction at HERA, Z. Phys. C 76 (1997) 599–612. [arXiv:hep-ex/9708010](#), [doi:10.1007/s002880050583](#).
  205. S. Chekanov, et al., Measurements of inelastic  $J/\psi$  and  $\psi'$  photoproduction at HERA, Eur. Phys. J. C 27 (2003) 173–188. [arXiv:hep-ex/0211011](#), [doi:10.1140/epjc/s2002-01130-2](#).
  206. S. Chekanov, et al., Exclusive electroproduction of  $J/\psi$  mesons at HERA, Nucl. Phys. B 695 (2004) 3–37. [arXiv:hep-ex/0404008](#), [doi:10.1016/j.nuclphysb.2004.06.034](#).
  207. S. Chekanov, et al., Measurement of  $J/\psi$  helicity distributions in inelastic photoproduction at HERA, JHEP 12 (2009) 007. [arXiv:0906.1424](#), [doi:10.1088/1126-6708/2009/12/007](#).
  208. H. Abramowicz, et al., Measurement of inelastic  $J/\psi$  and  $\psi'$  photoproduction at HERA, JHEP 02 (2013) 071. [arXiv:1211.6946](#), [doi:10.1007/JHEP02\(2013\)071](#).
  209. C. Adloff, et al., Diffractive photoproduction of  $\psi(2S)$  mesons at HERA, Phys. Lett. B 541 (2002) 251–264. [arXiv:hep-ex/0205107](#), [doi:10.1016/S0370-2693\(02\)02275-X](#).
  210. S. Chekanov, et al., Exclusive photoproduction of  $\psi(2S)$  mesons at HERA, Phys. Lett. B 680 (2009) 4–12. [arXiv:0903.4205](#), [doi:10.1016/j.physletb.2009.07.066](#).
  211. H. Abramowicz, et al., Measurement of the  $t$  dependence in exclusive photoproduction of  $\Upsilon(1S)$  mesons at HERA, Phys. Lett. B 708 (2012) 14–20. [arXiv:1111.2133](#), [doi:10.1016/j.physletb.2012.01.009](#).
  212. A. Aktas, et al., Measurement of deeply virtual Compton scattering at HERA, Eur. Phys. J. C 44 (2005) 1–11. [arXiv:hep-ex/0505061](#), [doi:10.1140/epjc/s2005-02345-3](#).
  213. F. D. Aaron, et al., Measurement of deeply virtual Compton scattering and its  $t$ -dependence at HERA, Phys. Lett. B 659 (2008) 796–806. [arXiv:0709.4114](#), [doi:10.1016/j.physletb.2007.11.093](#).
  214. F. D. Aaron, et al., Deeply Virtual Compton Scattering and its Beam Charge Asymmetry in  $e^\pm p$  Collisions at HERA, Phys. Lett. B 681 (2009) 391–399. [arXiv:0907.5289](#), [doi:10.1016/j.physletb.2009.10.035](#).
  215. S. Chekanov, et al., Measurement of deeply virtual Compton scattering at HERA, Phys. Lett. B 573 (2003) 46–62. [arXiv:hep-ex/0305028](#), [doi:10.1016/j.physletb.2003.08.048](#).
  216. S. Chekanov, et al., A Measurement of the  $Q^2$ ,  $W$  and  $t$  dependences of deeply virtual Compton scattering at HERA, JHEP 05 (2009) 108. [arXiv:0812.2517](#), [doi:10.1088/1126-6708/2009/05/108](#).
  217. A. Airapetian, et al., Spin Density Matrix Elements in Exclusive  $\rho^0$  Electroproduction on  $^1H$  and  $^2H$  Targets at 27.5-GeV Beam Energy, Eur. Phys. J. C 62 (2009) 659–695. [arXiv:0901.0701](#), [doi:10.1140/epjc/s10052-009-1082-3](#).
  218. A. Airapetian, et al., Ratios of helicity amplitudes for exclusive  $\rho^0$  electroproduction on transversely polarized protons, Eur. Phys. J. C 77 (6) (2017) 378. [arXiv:1702.00345](#), [doi:10.1140/epjc/s10052-017-4899-1](#).
  219. V. Andreev, et al., Exclusive  $\rho^0$  meson photoproduction with a leading neutron at HERA, Eur. Phys. J. C 76 (1) (2016) 41. [arXiv:1508.03176](#), [doi:10.1140/epjc/s10052-015-3863-1](#).
  220. G. Duplančić, S. Nabeebaccus, K. Passek-Kumerički, B. Pire, L. Szymanowski, S. Wallon, Accessing chiral-even quark generalised parton distributions in the exclusive photoproduction of a  $\gamma\pi^\pm$  pair with large invariant mass in both fixed-target and collider experiments, JHEP

- 03 (2023) 241. [arXiv:2212.00655](#), [doi:10.1007/JHEP03\(2023\)241](#).
221. G. Duplancić, S. Nabeebaccus, K. Passek-Kumerički, B. Pire, L. Szymanowski, S. Wallon, Probing chiral-even and chiral-odd leading twist quark generalized parton distributions through the exclusive photoproduction of a  $\gamma\rho$  pair, *Phys. Rev. D* 107 (9) (2023) 094023. [arXiv:2302.12026](#), [doi:10.1103/PhysRevD.107.094023](#).
222. R. Aaij, et al., Exclusive  $J/\psi$  and  $\psi(2S)$  production in pp collisions at  $\sqrt{s} = 7$  TeV, *J. Phys. G* 40 (2013) 045001. [arXiv:1301.7084](#), [doi:10.1088/0954-3899/40/4/045001](#).
223. R. Aaij, et al., Updated measurements of exclusive  $J/\psi$  and  $\psi(2S)$  production cross-sections in pp collisions at  $\sqrt{s} = 7$  TeV, *J. Phys. G* 41 (2014) 055002. [arXiv:1401.3288](#), [doi:10.1088/0954-3899/41/5/055002](#).
224. R. Aaij, et al., Measurement of the exclusive  $\Upsilon$  production cross-section in pp collisions at  $\sqrt{s} = 7$  TeV and 8 TeV, *JHEP* 09 (2015) 084. [arXiv:1505.08139](#), [doi:10.1007/JHEP09\(2015\)084](#).
225. R. Aaij, et al., Central exclusive production of  $J/\psi$  and  $\psi(2S)$  mesons in  $pp$  collisions at  $\sqrt{s} = 13$  TeV, *JHEP* 10 (2018) 167. [arXiv:1806.04079](#), [doi:10.1007/JHEP10\(2018\)167](#).
226. A. M. Sirunyan, et al., Measurement of exclusive  $\Upsilon$  photoproduction from protons in pPb collisions at  $\sqrt{s_{NN}} = 5.02$  TeV, *Eur. Phys. J. C* 79 (3) (2019) 277, [Erratum: *Eur.Phys.J.C* 82, 343 (2022)]. [arXiv:1809.11080](#), [doi:10.1140/epjc/s10052-019-6774-8](#).
227. B. Abelev, et al., Coherent  $J/\psi$  photoproduction in ultra-peripheral Pb-Pb collisions at  $\sqrt{s_{NN}} = 2.76$  TeV, *Phys. Lett. B* 718 (2013) 1273–1283. [arXiv:1209.3715](#), [doi:10.1016/j.physletb.2012.11.059](#).
228. E. Abbas, et al., Charmonium and  $e^+e^-$  pair photoproduction at mid-rapidity in ultra-peripheral PbPb collisions at  $\sqrt{s_{NN}}=2.76$  TeV, *Eur. Phys. J. C* 73 (11) (2013) 2617. [arXiv:1305.1467](#), [doi:10.1140/epjc/s10052-013-2617-1](#).
229. V. Khachatryan, et al., Coherent  $J/\psi$  photoproduction in ultra-peripheral PbPb collisions at  $\sqrt{s_{NN}} = 2.76$  TeV with the CMS experiment, *Phys. Lett. B* 772 (2017) 489–511. [arXiv:1605.06966](#), [doi:10.1016/j.physletb.2017.07.001](#).
230. S. Acharya, et al., Coherent  $J/\psi$  photoproduction at forward rapidity in ultra-peripheral Pb-Pb collisions at  $\sqrt{s_{NN}} = 5.02$  TeV, *Phys. Lett. B* 798 (2019) 134926. [arXiv:1904.06272](#), [doi:10.1016/j.physletb.2019.134926](#).
231. S. Acharya, et al., Coherent  $J/\psi$  and  $\psi'$  photoproduction at midrapidity in ultraperipheral Pb-Pb collisions at  $\sqrt{s_{NN}} = 5.02$  TeV, *Eur. Phys. J. C* 81 (8) (2021) 712. [arXiv:2101.04577](#), [doi:10.1140/epjc/s10052-021-09437-6](#).
232. S. Acharya, et al., First measurement of the  $|t|$ -dependence of coherent  $J/\psi$  photonuclear production, *Phys. Lett. B* 817 (2021) 136280. [arXiv:2101.04623](#), [doi:10.1016/j.physletb.2021.136280](#).
233. R. Aaij, et al.,  $J/\psi$  photoproduction in Pb-Pb peripheral collisions at  $\sqrt{s_{NN}} = 5$  TeV, *Phys. Rev. C* 105 (3) (2022) L032201. [arXiv:2108.02681](#), [doi:10.1103/PhysRevC.105.L032201](#).
234. R. Aaij, et al., Study of exclusive photoproduction of charmonium in ultra-peripheral lead-lead collisions, *JHEP* 06 (2023) 146. [arXiv:2206.08221](#), [doi:10.1007/JHEP06\(2023\)146](#).
235. C. A. Flett, A. D. Martin, M. G. Ryskin, T. Teubner, Very low  $x$  gluon density determined by LHCb exclusive  $J/\psi$  data, *Phys. Rev. D* 102 (2020) 114021. [arXiv:2006.13857](#), [doi:10.1103/PhysRevD.102.114021](#).
236. B. Pire, L. Szymanowski, J. Wagner, Can one measure timelike Compton scattering at LHC?, *Phys. Rev. D* 79 (2009) 014010. [arXiv:0811.0321](#), [doi:10.1103/PhysRevD.79.014010](#).
237. S. Acharya, et al., Exclusive and dissociative  $J/\psi$  photoproduction, and exclusive dimuon production, in p-Pb collisions at  $\sqrt{s_{NN}} = 8.16$  TeV, *Phys. Rev. D* 108 (11) (2023) 112004. [arXiv:2304.12403](#), [doi:10.1103/PhysRevD.108.112004](#).
238. H. I. Miettinen, J. Pumplin, [Diffraction scattering and the parton structure of hadrons](#), *Phys. Rev. D* 18 (1978) 1696–1708. [doi:10.1103/PhysRevD.18.1696](#). URL <https://link.aps.org/doi/10.1103/PhysRevD.18.1696>
239. Z. Citron, et al., Report from Working Group 5: Future physics opportunities for high-density QCD at the LHC with heavy-ion and proton beams, CERN Yellow Rep. Monogr. 7 (2019) 1159–1410. [arXiv:1812.06772](#), [doi:10.23731/CYRM-2019-007.1159](#).
240. C. Hadjidakis, et al., A fixed-target programme at the LHC: Physics case and projected performances for heavy-ion, hadron, spin and astroparticle studies, *Phys. Rept.* 911 (2021) 1–83. [arXiv:1807.00603](#), [doi:10.1016/j.physrep.2021.01.002](#).
241. C. Barschel, [Precision luminosity measurement at LHCb with beam-gas imaging](#), Ph.D. thesis, RWTH Aachen U. (2014). URL <https://publications.rwth-aachen.de/>

- [record/229539/files/4989.pdf](#)
242. R. Aaij, et al., First Measurement of Charm Production in its Fixed-Target Configuration at the LHC, *Phys. Rev. Lett.* 122 (13) (2019) 132002. [arXiv:1810.07907](#), [doi:10.1103/PhysRevLett.122.132002](#).
  243. R. Aaij, et al., Measurement of Antiproton Production in pHe Collisions at  $\sqrt{s_{NN}} = 110$  GeV, *Phys. Rev. Lett.* 121 (22) (2018) 222001. [arXiv:1808.06127](#), [doi:10.1103/PhysRevLett.121.222001](#).
  244. P. Abbon, et al., The COMPASS experiment at CERN, *Nucl. Instrum. Meth. A* 577 (2007) 455–518. [arXiv:hep-ex/0703049](#), [doi:10.1016/j.nima.2007.03.026](#).
  245. B. Adams, et al., Letter of Intent: A New QCD facility at the M2 beam line of the CERN SPS (COMPASS++/AMBER) (8 2018). [arXiv:1808.00848](#).
  246. A. Accardi, et al., Electron Ion Collider: The Next QCD Frontier: Understanding the glue that binds us all, *Eur. Phys. J. A* 52 (9) (2016) 268. [arXiv:1212.1701](#), [doi:10.1140/epja/i2016-16268-9](#).
  247. GSI Helmholtzzentrum für Schwerionenforschung GmbH, GSI-FAIR Scientific Report 2022, GSI Report 2023-1 (2023). [doi:10.15120/GSI-2023-00462](#).
  248. A. Bursche, H. P. Dembinski, P. Di Nezza, M. Ferro-Luzzi, F. Fleuret, G. Graziani, G. Manca, E. A. Maurice, N. Neri, L. L. Pappalardo, P. Robbe, M. Schmelling, M. A. Winn, V. Zhukov, [Physics opportunities with the fixed-target program of the LHCb experiment using an unpolarized gas target](#) (2018). URL <https://cds.cern.ch/record/2649878>
  249. LHCb SMOG Upgrade (2019). [doi:10.17181/CERN.SAQC.EOWH](#).
  250. C. A. Aidala, et al., The LHCSpin Project (1 2019). [arXiv:1901.08002](#).
  251. K. Kumerički, Measurability of pressure inside the proton, *Nature* 570 (7759) (2019) E1–E2. [doi:10.1038/s41586-019-1211-6](#).
  252. Y. Guo, X. Ji, M. G. Santiago, K. Shiells, J. Yang, Generalized parton distributions through universal moment parameterization: non-zero skewness case, *JHEP* 05 (2023) 150. [arXiv:2302.07279](#), [doi:10.1007/JHEP05\(2023\)150](#).
  253. V. Bertone, H. Dutrieux, C. Mezrag, H. Moutarde, P. Sznajder, Deconvolution problem of deeply virtual Compton scattering, *Phys. Rev. D* 103 (11) (2021) 114019. [arXiv:2104.03836](#), [doi:10.1103/PhysRevD.103.114019](#).
  254. E. Moffat, A. Freese, I. Cloët, T. Donohoe, L. Gamberg, W. Melnitchouk, A. Metz, A. Prokudin, N. Sato, Shedding light on shadow generalized parton distributions, *Phys. Rev. D* 108 (3) (2023) 036027. [arXiv:2303.12006](#), [doi:10.1103/PhysRevD.108.036027](#).
  255. H. Dutrieux, C. Lorcé, H. Moutarde, P. Sznajder, A. Trawiński, J. Wagner, Phenomenological assessment of proton mechanical properties from deeply virtual Compton scattering, *Eur. Phys. J. C* 81 (4) (2021) 300. [arXiv:2101.03855](#), [doi:10.1140/epjc/s10052-021-09069-w](#).
  256. K. M. Semenov-Tian-Shansky, P. Sznajder, Systematic description of hadron's response to non-local QCD probes: Froissart-Gribov projections in analysis of deeply virtual Compton scattering, *Phys. Rev. D* 109 (2024) 054010. [arXiv:2312.09624](#), [doi:10.1103/PhysRevD.109.054010](#).
  257. S. V. Goloskokov, P. Kroll, Vector meson electroproduction at small Bjorken- $x$  and generalized parton distributions, *Eur. Phys. J. C* 42 (2005) 281–301. [arXiv:hep-ph/0501242](#), [doi:10.1140/epjc/s2005-02298-5](#).
  258. M. Vanderhaeghen, P. A. M. Guichon, M. Guidal, Hard electroproduction of photons and mesons on the nucleon, *Phys. Rev. Lett.* 80 (1998) 5064–5067. [doi:10.1103/PhysRevLett.80.5064](#).
  259. C. Mezrag, H. Moutarde, F. Sabatié, Test of two new parametrizations of the generalized parton distribution H, *Phys. Rev. D* 88 (1) (2013) 014001. [arXiv:1304.7645](#), [doi:10.1103/PhysRevD.88.014001](#).
  260. K. Kumerički, D. Müller, Description and interpretation of DVCS measurements, *EPJ Web Conf.* 112 (2016) 01012. [arXiv:1512.09014](#), [doi:10.1051/epjconf/201611201012](#).
  261. M. V. Polyakov, A. G. Shuvaev, On 'dual' parametrizations of generalized parton distributions (2002). [arXiv:hep-ph/0207153](#).
  262. M. V. Polyakov, K. M. Semenov-Tian-Shansky, Dual parametrization of GPDs versus double distribution Ansatz, *Eur. Phys. J. A* 40 (2009) 181–198. [arXiv:0811.2901](#), [doi:10.1140/epja/i2008-10759-2](#).
  263. D. Müller, M. V. Polyakov, K. M. Semenov-Tian-Shansky, Dual parametrization of generalized parton distributions in two equivalent representations, *JHEP* 03 (2015) 052. [arXiv:1412.4165](#), [doi:10.1007/JHEP03\(2015\)052](#).
  264. C. Mezrag, Generalised Parton Distributions in Continuum Schwinger Methods: Progresses, Opportunities and Challenges, *Particles* 6 (1) (2023) 262–296. [doi:10.3390/particles6010015](#).

- 
265. H. Dutrieux, O. Grocholski, H. Moutarde, P. Sznajder, Artificial neural network modelling of generalised parton distributions, *Eur. Phys. J. C* 82 (3) (2022) 252, [Erratum: *Eur.Phys.J.C* 82, 389 (2022)]. [arXiv:2112.10528](#), [doi:10.1140/epjc/s10052-022-10211-5](#).
266. V. M. Braun, A. N. Manashov, B. Pirnay, Finite- $t$  and target mass corrections to deeply virtual Compton scattering, *Phys. Rev. Lett.* 109 (2012) 242001. [arXiv:1209.2559](#), [doi:10.1103/PhysRevLett.109.242001](#).
267. Y. Guo, X. Ji, K. Shiells, Higher-order kinematical effects in deeply virtual Compton scattering, *JHEP* 12 (2021) 103. [arXiv:2109.10373](#), [doi:10.1007/JHEP12\(2021\)103](#).
268. V. M. Braun, Y. Ji, A. N. Manashov, Next-to-leading-power kinematic corrections to DVCS: a scalar target, *JHEP* 01 (2023) 078. [arXiv:2211.04902](#), [doi:10.1007/JHEP01\(2023\)078](#).
269. K. Kumericki, D. Müller, K. Passek-Kumericki, Towards a fitting procedure for deeply virtual Compton scattering at next-to-leading order and beyond, *Nucl. Phys. B* 794 (2008) 244–323. [arXiv:hep-ph/0703179](#), [doi:10.1016/j.nuclphysb.2007.10.029](#).
270. B. Berthou, et al., PARTONS: PARTonic Tomography Of Nucleon Software: A computing framework for the phenomenology of Generalized Parton Distributions, *Eur. Phys. J. C* 78 (6) (2018) 478. [arXiv:1512.06174](#), [doi:10.1140/epjc/s10052-018-5948-0](#).
271. E. C. Aschenauer, V. Batozskaya, S. Fazio, K. Gates, H. Moutarde, D. Sokhan, H. Spiesberger, P. Sznajder, K. Tezgin, EpIC: novel Monte Carlo generator for exclusive processes, *Eur. Phys. J. C* 82 (9) (2022) 819. [arXiv:2205.01762](#), [doi:10.1140/epjc/s10052-022-10651-z](#).